

AD-A191 975

STABILITY AND DRAG REDUCTION IN A BOUNDARY LAYER WITH
MICROBUBBLES(U) PENNSYLVANIA STATE UNIV UNIVERSITY PARK
APPLIED RESEARCH LAB J M NEVES FEB 88

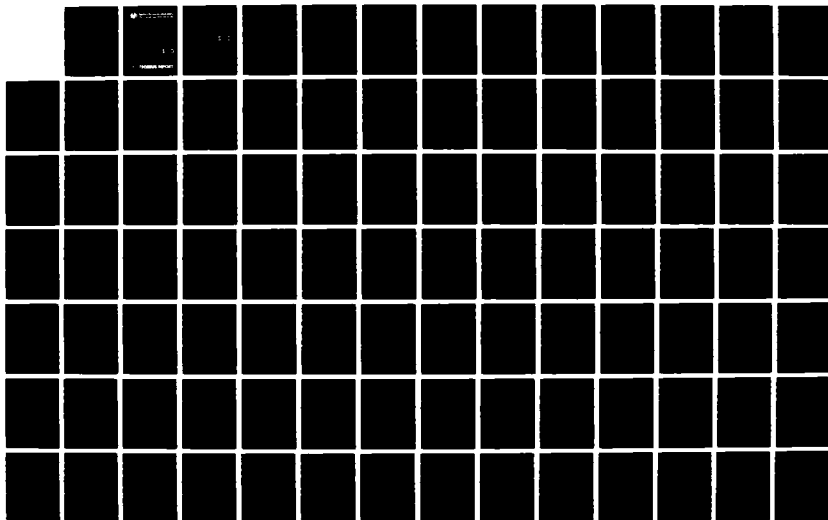
1/2

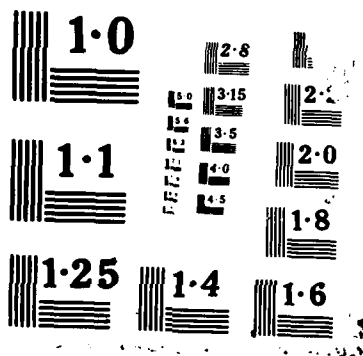
UNCLASSIFIED

ARL/PSU-TR-88-001 N00024-85-C-6041

F/G 20/4

NL







Applied Research Laboratory The Pennsylvania State University

AD-A191 975

STABILITY AND DRAG REDUCTION IN A
BOUNDARY LAYER WITH MICROBUBBLES

by

Joao M. P. Correia Neves

DTIC
ELECTE
MAR 22 1988
S C_H D

DISTRIBUTION STATEMENT A

Approved for public release;
Distribution Unlimited



TECHNICAL REPORT

88 3 21 124

4

The Pennsylvania State University
APPLIED RESEARCH LABORATORY
P.O. Box 30
State College, PA 16804

STABILITY AND DRAG REDUCTION IN A
BOUNDARY LAYER WITH MICROBUBBLES

by

Joao M. P. Correia Neves

Technical Report No. TR 88-001

February 1988

DTIC
ELECTE
MAR 22 1988
S D
H a

Supported by:
Naval Sea Systems Command

L. R. Hettche
Applied Research Laboratory

Approved for public release; distribution unlimited

Unclassified

SECURITY CLASSIFICATION OF THIS PAGE

ADA 191975

REPORT DOCUMENTATION PAGE

1a. REPORT SECURITY CLASSIFICATION Unclassified			1b. RESTRICTIVE MARKINGS		
2a. SECURITY CLASSIFICATION AUTHORITY			3. DISTRIBUTION / AVAILABILITY OF REPORT		
2b. DECLASSIFICATION / DOWNGRADING SCHEDULE			Unlimited		
4. PERFORMING ORGANIZATION REPORT NUMBER(S) TR 88-001			5. MONITORING ORGANIZATION REPORT NUMBER(S)		
6a. NAME OF PERFORMING ORGANIZATION Applied Research Laboratory The Penna. State University		6b. OFFICE SYMBOL (If applicable) ARL	7a. NAME OF MONITORING ORGANIZATION Naval Sea Systems Command Department of the Navy		
6c. ADDRESS (City, State, and ZIP Code) P. O. Box 30 State College, PA 16804			7b. ADDRESS (City, State, and ZIP Code) Washington, DC 20362		
8a. NAME OF FUNDING / SPONSORING ORGANIZATION Naval Sea Systems Command		8b. OFFICE SYMBOL (If applicable) NAVSEA	9. PROCUREMENT INSTRUMENT IDENTIFICATION NUMBER N-00024-85-C-6041		
8c. ADDRESS (City, State, and ZIP Code) Department of the Navy Washington, DC 20362			10. SOURCE OF FUNDING NUMBERS		11. TITLE (Include Security Classification)
			PROGRAM ELEMENT NO.	PROJECT NO.	TASK NO.
			WORK UNIT ACCESSION NO.		
12. PERSONAL AUTHOR(S) Joao M. P. Correia Neves					
13a. TYPE OF REPORT thesis		13b. TIME COVERED FROM TO		14. DATE OF REPORT (Year, Month, Day) Febrvart 1988	
15. PAGE COUNT 136					
16. SUPPLEMENTARY NOTATION					
17. COSATI CODES			18. SUBJECT TERMS (Continue on reverse if necessary and identify by block number)		
FIELD	GROUP	SUB-GROUP	Boundary Layers, Cavitation, Drag Reduction		
19. ABSTRACT (Continue on reverse if necessary and identify by block number)					
<p>When microbubbles are injected in a turbulent boundary layer, they promote a reduction of the local skin friction and a sharp mean velocity gradient between the two microbubble free regions in the boundary layer, i.e., the outer edge and the near wall region.</p>					
20. DISTRIBUTION / AVAILABILITY OF ABSTRACT <input checked="" type="checkbox"/> UNCLASSIFIED/UNLIMITED <input type="checkbox"/> SAME AS RPT <input type="checkbox"/> DTIC USERS			21. ABSTRACT SECURITY CLASSIFICATION Unclassified		
22a. NAME OF RESPONSIBLE INDIVIDUAL			22b. TELEPHONE (Include Area Code)		22c. OFFICE SYMBOL

Unclassified

SECURITY CLASSIFICATION OF THIS PAGE

In connection with the apparent stability of the bubbles in the boundary layer, the stability of a hollow vortex sheet in an infinite expanse of fluid as well as in the presence of a wall are studied. We concluded that the simple hollow vortex sheet is unconditionally unstable while a stability range was found for a hollow vortex sheet perturbed in the presence of a wall. In all cases, however, the computations suggest that the hollow vortex radius is invariably a destabilizing factor.

Regarding the second aspect of the problem, a heuristic, but physically sound explanation of the mechanisms of the drag reduction is proposed. Based on these ideas and using a phenomenological approach, the flat plate boundary layer is numerically analyzed.



Accession For		
NTIS GRA&I	<input checked="" type="checkbox"/>	
DTIC TAB	<input type="checkbox"/>	
Unannounced	<input type="checkbox"/>	
Justification		
By		
Distribution/		
Availability Codes		
Avail and/or		
Dist	Special	
A-1		

Unclassified

SECURITY CLASSIFICATION OF THIS PAGE

ABSTRACT

When microbubbles are injected in a turbulent boundary layer, they promote a reduction of the local skin friction and a sharp mean velocity gradient between the two microbubble free regions in the boundary layer, i.e., the outer edge and the near wall region.

In connection with the apparent stability of the bubbles in the boundary layer, the stability of a hollow vortex sheet in an infinite expanse of fluid as well as in the presence of a wall are studied. We concluded that the simple hollow vortex sheet is unconditionally unstable while a stability range was found for a hollow vortex sheet perturbed in the presence of a wall. In all cases, however, the computations suggest that the hollow vortex radius is invariably a destabilizing factor.

Regarding the second aspect of the problem, a heuristic, but physically sound explanation of the mechanisms of the drag reduction is proposed. Based on these ideas and using a phenomenological approach, the flat plate boundary layer is numerically analyzed.

TABLE OF CONTENTS

	<u>Page</u>
ABSTRACT	iii
LIST OF FIGURES	vi
ACKNOWLEDGMENTS	viii
NOMENCLATURE	ix
 <u>Chapter</u>	
1. INTRODUCTION	1
1.1 Previous Experimental Work	1
1.2 Problem Statement	9
1.2.1 The Stability	11
1.2.2 The Drag Reduction	11
2. STABILITY OF A HOLLOW VORTEX SHEET	12
2.1 Introduction	12
2.2 A Simple Hollow Vortex Sheet	13
2.3 A Symmetric Hollow Vortex Sheet	18
3. EVOLUTION OF A HOLLOW VORTEX SHEET	28
3.1 Introduction	28
3.2 The Dipole Strength of the System	29
3.3 The Dynamics of the System	36
3.4 The Image System	41
4. THE DRAG REDUCTION	48
4.1 Introduction	48
4.2 The Constitutive Relation	49
4.3 The Mechanisms of the Drag Reduction	52
4.4 The System of Equations	56
4.5 The Turbulent Regime	59
4.6 The Boundary Conditions	66
4.7 Results	67
5. DISCUSSION AND CONCLUSIONS	74
5.1 The Stability	74
5.2 The Drag Reduction	76

TABLE OF CONTENTS [continuation]

	<u>Page</u>
BIBLIOGRAPHY	80
APPENDIX A. THE FOURIER SERIES EXPANSIONS	86
APPENDIX B. THE CONTOUR INTEGRALS	88
APPENDIX C. THE HOLLOW VORTEX SHEET EVOLUTION CODE	91
APPENDIX D. THE MANGLER-LEVY-LEES TRANSFORMATION	97
APPENDIX E. THE BOUNDARY LAYER CODE	101

LIST OF FIGURES

<u>Figure</u>		<u>Page</u>
1.1	Ratio of Integrated Skin Friction in the Presence of Microbubbles to Skin Friction without Microbubbles as a Function of Airflow Rate	3
1.2	Velocity Profiles in the Absence of Microbubbles Presented in Inner Variables	4
1.3	Velocity Profiles in the Absence of Microbubbles Presented in Outer Variables	5
1.4	The Downstream Persistence of the Skin Friction Reduction $U_\infty = 16.8$ m/s	7
1.5	The Downstream Persistence of the Skin Friction Reduction $U_\infty = 10.7$ m/s	8
1.6	Comparison of Mean Velocity Profiles in the Outer Part of the Boundary Layer in the Presence and Absence of Microbubbles	10
2.1	A Simple Hollow Vortex Sheet	15
2.2	A Symmetric Hollow Vortex Sheet	19
2.3	Stability Envelope for a Symmetric Hollow Vortex Sheet	27
3.1	Flow Field Variables at the m^{th} Hollow Vortex	30
3.2	Evolution of a Simple Point Vortex Sheet starting with a Sinusoidal Deformation of Amplitude $\beta = 0.05$	40
3.3	Evolution of a Simple Point Vortex Sheet in the Presence of a Wall, starting with a Sinusoidal Deformation of Amplitude $\beta = 0.025$ and $k = 0.08$	40
3.4	Evolution of a Simple Hollow Vortex Sheet starting with a Sinusoidal Deformation of Amplitude $\beta = 0.05$ and $\alpha = 0.01$	42
3.5	Evolution of a Simple Hollow Vortex Sheet starting with a Sinusoidal Deformation of Amplitude $\beta = 0.05$ and $\alpha = 0.018$	42
4.1	Relationship between the Specific Viscosity and the Void Fraction	51

LIST OF FIGURES [continuation]

<u>Figure</u>		<u>Page</u>
4.2	Variation of the Skin Friction with the Streamwise Reynolds Number in the Absence of Injection ($U_{\infty} = 4.2$ m/s)	68
4.3	Variation of the Boundary Layer Displacement Thickness Reynolds Number with the Streamwise Reynolds Number in the Absence of Injection ($U_{\infty} = 4.2$ m/s)	69
4.4	Variation of the Boundary Layer Momentum Thickness Reynolds Number with the Streamwise Reynolds Number in the Absence of Injection ($U_{\infty} = 4.2$ m/s)	70
4.5	Variation of the Boundary Layer Shape Factor with the Streamwise Reynolds Number in the Absence of Injection ($U_{\infty} = 4.2$ m/s)	71

ACKNOWLEDGMENTS

The author wishes to express his deep indebtedness to several persons.

To my dear mother, I owe the constant support and encouragement that nourished ideals that made this moment possible.

To Dr. Barnes W. McCormick, then Head of the Department of Aerospace Engineering of The Pennsylvania State University, I owe the gift of coming to the United States and of studying at The Pennsylvania State University.

I want to thank Dr. James D. Foch, Jr. for the offer of the assistantship that supported the research as well as the academic work of the author. The funds were provided by the Office of Naval Research through an E/F Grant from NAVSEA Contract N00024-79-C-6043.

From Dr. Blaine R. Parkin, my adviser during most of the work, I always had the freedom that allowed me to study many subjects which, I am confident, will bear fruit in the near future. To him, I am also indebted for the constant stimulus and an experience that has shaped indelibly my attitude towards research.

Finally, I want to thank Mrs. Leanne Zindler for her patient and resourceful typing which I most appreciated.

NOMENCLATURE

a	hollow vortex radius
$A = \pi a^2$	hollow vortex cross section area
b	distance of hollow vortex sheet to the wall
$\vec{B} = (B_x, B_y)$	2D body force vector
C	void fraction boundary condition
C_f	local skin friction
d	bubble diameter
du/dy	characteristic velocity gradient
$D_i = L_i a^2$	dipole strength of the i^{th} hollow vortex
f	Mangler streamfunction
$F_i = (F_{x_i}, F_{y_i})$	complex hollow vortex force vector
g	acceleration of gravity
G_i	hollow vortex dipole function
h	mixing length correction function
H	boundary layer shape factor
$k = b/\lambda$	wall distance parameter
ℓ	Prandtl's mixing length
L	length scale
L_i	dipole strength parameter of the i^{th} hollow vortex
N	number of hollow vortices per wavelength of disturbance
P	mean pressure field
\tilde{p}	pressure disturbance
P_∞	free stream pressure field

NOMENCLATURE [continuation]

Q_g	gas volume flow rate
$Re_L = \rho_l U_\infty L / \mu_l$	free stream Reynolds number
$Re_x = \rho_l U_\infty x / \mu_l$	streamwise Reynolds number
$Re_{\theta_{tr}} = \rho_l U_\infty \theta / \mu_l$	transition Reynolds number based on momentum thickness
S_i	acceleration source term of the i^{th} vortex
$T_a = \mu_l d(du/dy)/\sigma$	bubble nondimensional parameter
U_∞	free stream velocity
(U, V)	mean velocity field
\bar{U}	far stream induced velocity
(\tilde{u}, \tilde{v})	velocity disturbances
U_i	complex velocity of the i^{th} hollow vortex
$\overline{u^2}, \overline{v^2}, \overline{uv}$	2D Reynolds stresses
$u^* = \sqrt{\tau_w / \rho_l}$	friction velocity
$v' = \sqrt{Re_L} v$	boundary layer scaled velocity component
\vec{V}	2D velocity vector
\bar{V}	symmetric vortex sheet rigid body velocity
W	complex velocity potential
X	volume fraction
x	streamwise variable
y	cross stream variable
$y^+ = y u^* / \nu_l$	cross stream inner variable
$y' = \sqrt{Re_L} y$	boundary layer scaled variable
$z_i = (x_i, y_i)$	complex vortex position vector

NOMENCLATURE [continuation]

z_{oi}	first order displacement of the i^{th} order
z_{ci}	displacement correction of the i^{th} vortex
$\alpha = \pi a / \lambda$	hollow vortex small parameter
β	vortex sheet dimensionless amplitude
δ	boundary layer thickness
$\delta^* = \int_0^\infty (1 - \frac{\rho u}{\rho_\infty U_\infty}) dy$	boundary layer displacement thickness
$\nabla \cdot = \frac{\partial}{\partial x} \vec{i} + \frac{\partial}{\partial y} \vec{j}$	2D gradient operator
$\nabla \times \vec{A} = k (\frac{\partial A_x}{\partial y} - \frac{\partial A_y}{\partial x})$	2D curl operator
$\nabla^2 = \frac{\partial^2}{\partial x^2} + \frac{\partial^2}{\partial y^2}$	2D Laplace operator
ϵ	eddy viscosity
ϵ_{ref}	reference viscosity
ϕ	velocity potential
γ	vortex circulation
$\Gamma = \frac{\gamma}{2\pi}$	circulation parameter
η	cross stream Mangler variable
λ	wave length
μ	mixture viscosity
μ_ℓ	liquid viscosity
$\mu_{\text{sp}} = \frac{\mu}{\mu_\ell} - 1$	specific viscosity
$\mu_t = \mu_\ell + \rho_\ell \epsilon$	turbulent viscosity
$\mu_{t_{\text{ref}}} = \mu_\ell + \rho_\ell \epsilon_{\text{ref}}$	turbulence stretching parameter
$\nu = \mu / \rho$	kinematic viscosity
χ	characteristic function
ρ	mixture density

NOMENCLATURE [continuation]

ρ_l	liquid density
ρ_g	gas density
σ	surface tension
τ	shear stress
τ_w	wall shear stress
θ	disturbance phase
$\omega = \pi\Gamma/\lambda\bar{V}$	hollow vortex circulation small parameter
ψ	stream function
ξ	streamwise Mangler variable
ζ	hollow vortex sheet stability parameter

CHAPTER I

INTRODUCTION

1.1 Previous Experimental Work

The idea of reducing the skin friction between water and a solid by injecting air close to the surface goes back to Froude, 1875. It was hoped that the lower viscosity of the injected fluid close to the surface would lead to a reduction in the skin friction. Indeed, from the very beginning experiments validated this idea. Even though the mechanisms by which the drag reduction is brought about are not yet fully understood, the phenomenon and its potential applications have lured the attention of physicists and engineers ever since.

What precludes our full understanding of the problem is that it occurs in a strictly turbulent flow. Turbulence itself is included in the category of one of the major unsolved problems of physics today. With the addition of small bubbles in the boundary layer, the drag reduction is intimately related to subtle flow interactions between the bubbles and the carrier fluid in the viscous and the buffer layers of the boundary layer. Even in the case of the simple turbulent boundary layer, today's knowledge of the near wall region is far from complete mainly because of experimental difficulties in obtaining reliable data close to the surface. In the case of the turbulent boundary layer with microbubbles, this difficulty is further aggravated because the thickness of the film of fluid between the bubble layer and the wall is of the order of micrometers and the bubbles are optically opaque.

The interest in studying this phenomenon has intensified in the past twenty years mainly as a result of a better physical understanding of turbulent flows and of new experimental techniques developed to study more complex flowfields.

Some researchers [1] chose to generate the microbubbles in the boundary layer via electrolysis. This approach, however, does not seem to be the most appropriate if one is interested in studying the interactions between the bubbles and the mean flow in the boundary layer because of the presence there of the gas generating wire.

The study of the turbulent boundary layer flow with microbubble injection was undertaken in a systematic fashion for the first time in the Soviet Union [2,3,4,5] at the beginning of the last decade. These researchers, as well as the research group at The Pennsylvania State University, have become dedicated more recently to the same problem [6,7,8]. In the United States, this group chose to inject the gaseous fluid in the boundary layer through porous plates.

The results of the work of N. K. Madavan, et al. [8] as well as those of the Soviet researchers show that the local skin friction coefficient can be reduced to within 20% of its undisturbed value. Figure 1.1 illustrates some of these findings.

In this particular work, the boundary layer was observed on a flat plate at zero pressure gradient. In the absence of microbubbles, the boundary layer exhibited the classical characteristics of a fully developed turbulent boundary layer, as is evident from the data which are reproduced in Figure 1.2 and Figure 1.3.

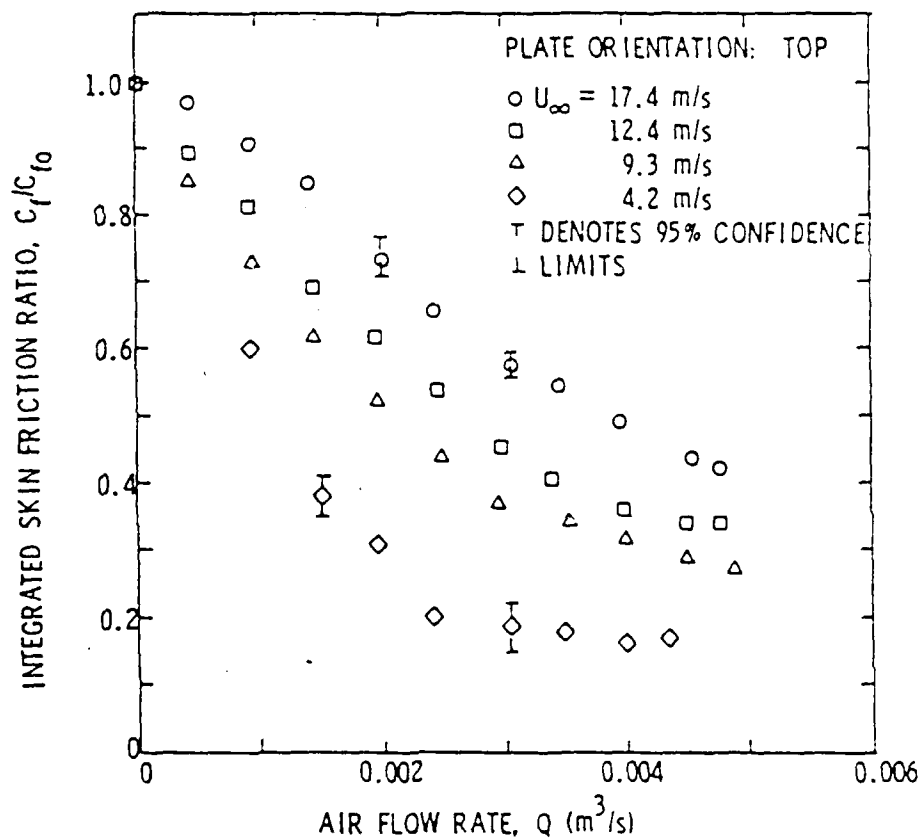


Figure 1.1. Ratio of Integrated Skin Friction in the Presence of Microbubbles to Skin Friction without Microbubbles as a Function of Airflow Rate.

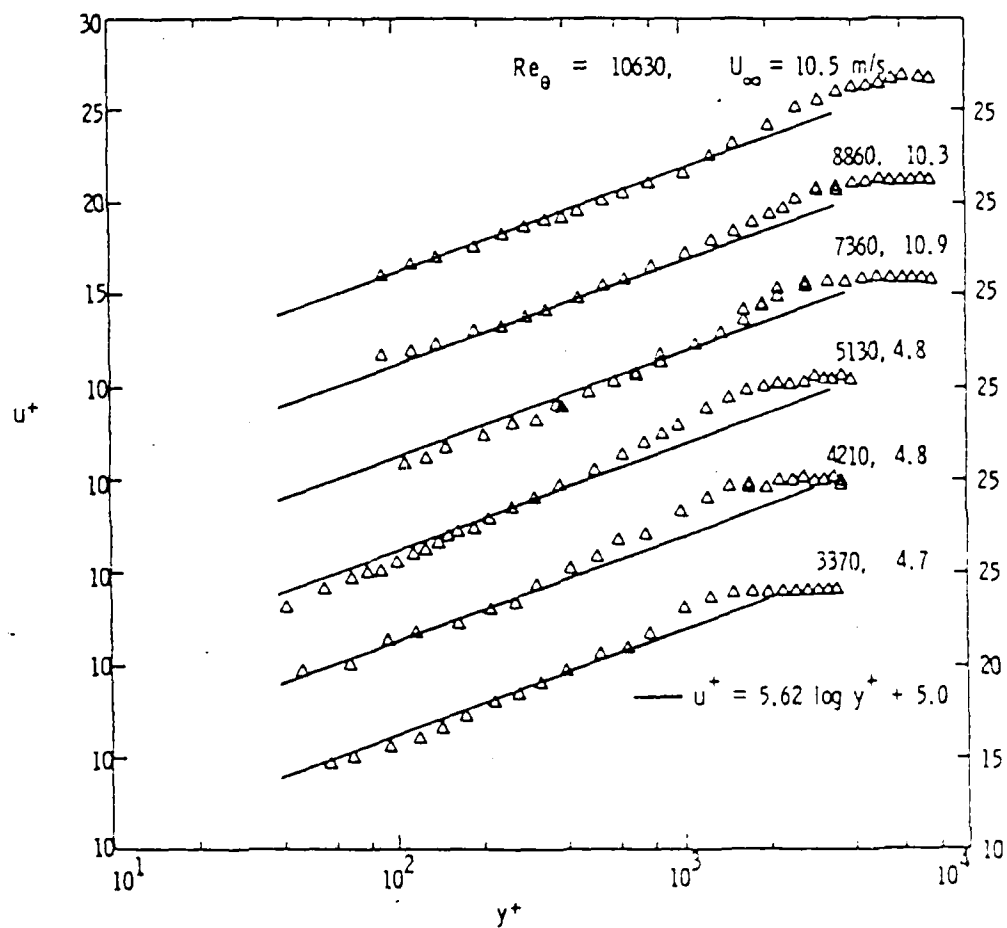


Figure 1.2. Velocity Profiles in the Absence of Microbubbles Presented in Inner Variables.

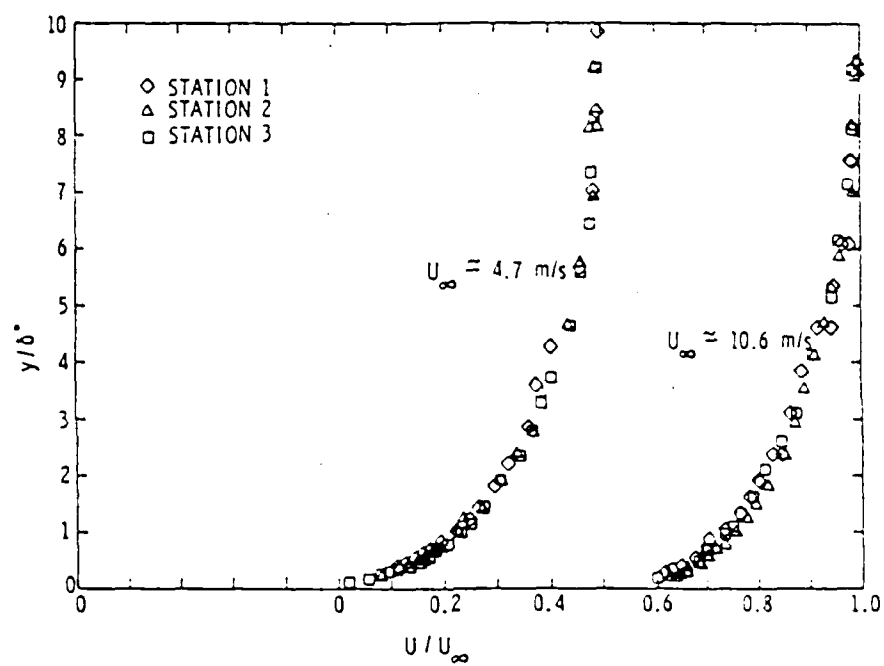


Figure 1.3. Velocity Profiles in the Absence of Microbubbles Presented in Outer Variables.

As reported in [8], Figure 1.1 indicates that the skin friction is decreased as soon as the gas starts being injected through the plate. It is noted also that the amount of the skin friction reduction generally increases with increased gas flow and decreased free stream velocity. Indeed, the results suggest that for a given free stream velocity there is an optimum gas flow rate for which the skin friction reduction is a maximum. In [8] it is shown that the skin friction reduction data can be collapsed on the same curve if plotted against the ratio of the gas flow to the total flow in the boundary layer.

Generally, for any gas flow rate, it was observed that the maximum skin friction reduction occurred immediately downstream of the porous section and that the skin friction gradually recovers to its undisturbed value in the downstream direction. Madavan, et al. [6] reports that the skin reduction is felt as far downstream as 60 to 70 boundary layer thicknesses. The results shown in Figure 1.4 and Figure 1.5, taken from this work, are representative of the conclusions obtained.

Both N. K. Madavan, et al. [6] and G. S. Migirenko, et al. [7] report that at the higher speed flow regimes the bubble packing is higher while the bubble mean radius is smaller. The latter author claims that the highest bubble volumetric concentrations of the order of 80% are at a location of around $0.1\delta^*$. In fact, contrary to the findings of the Soviet researchers in [6], it is reported that the bubble radius is much more sensitive to the

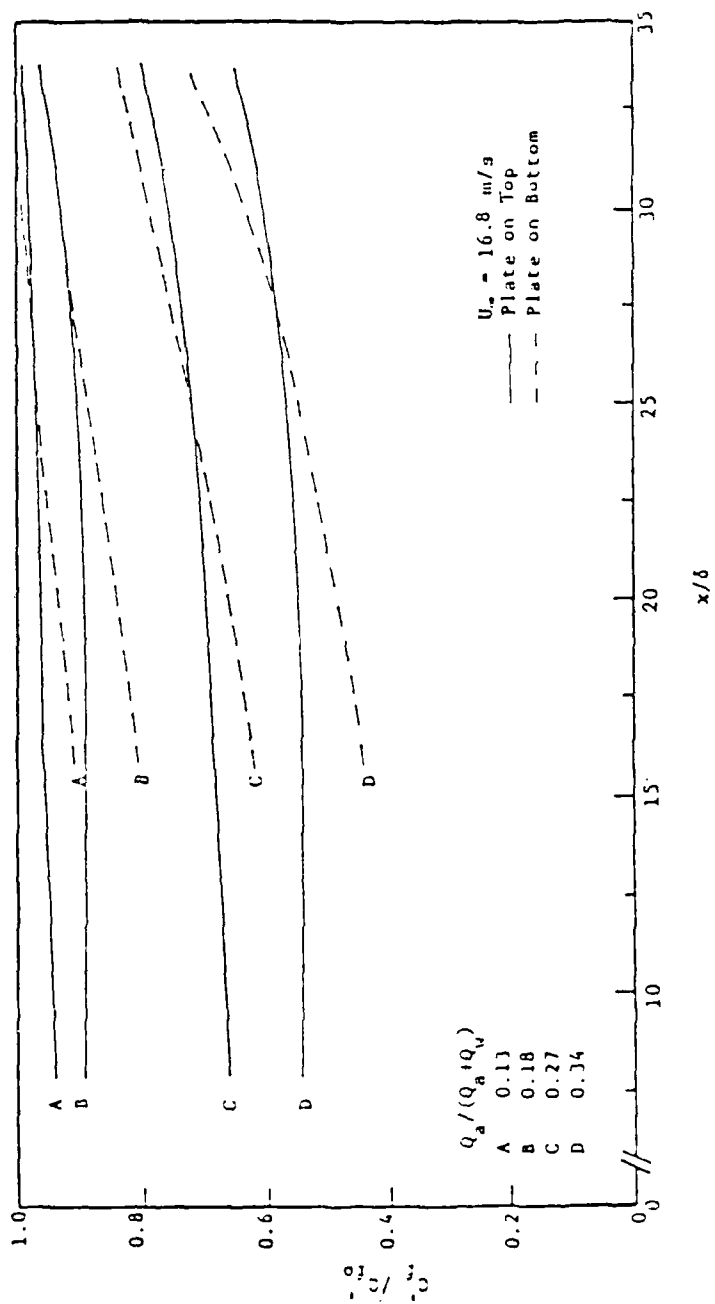


Figure 1.4. The Downstream Persistence of the Skin Friction Reduction $U_\infty = 16.8 \text{ m/s}$.

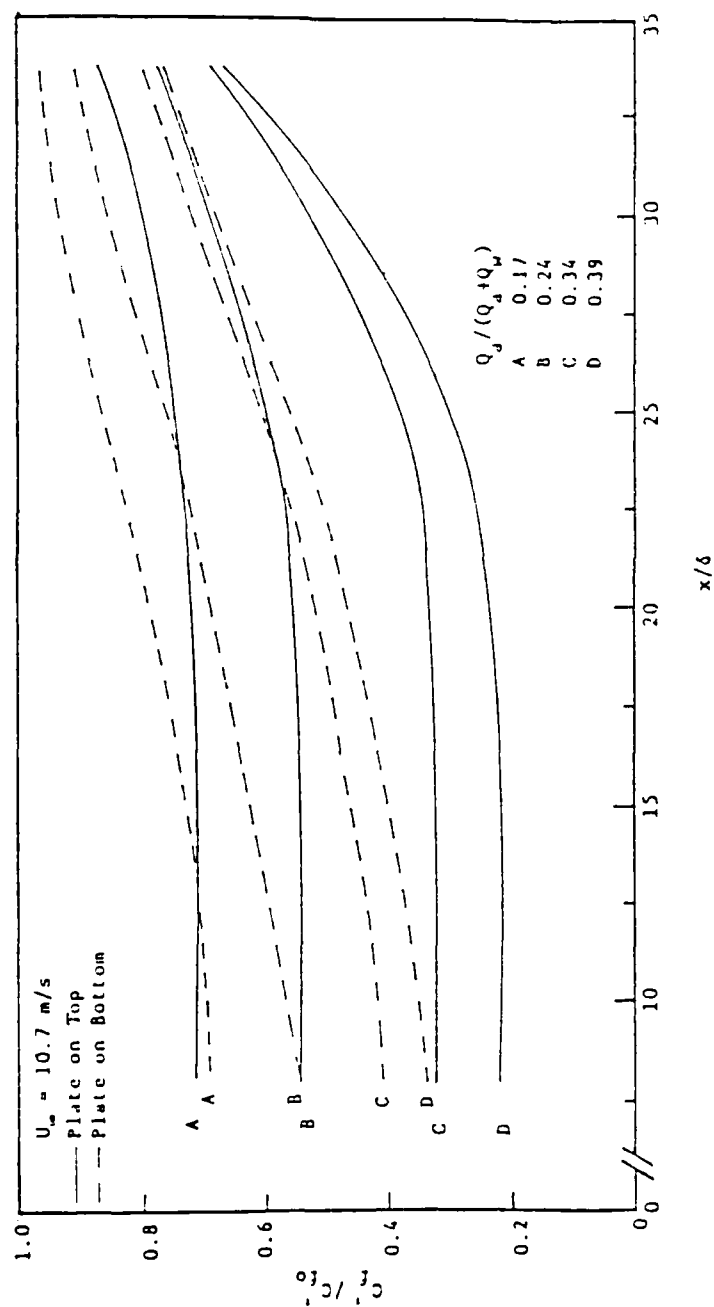


Figure 1.5. The Downstream Persistence of the Skin Friction
Reduction $U_\infty = 10.7 \text{ m/s}$.

flow conditions than to the characteristics of the porous materials through which the gas is injected. This seems to be in line with experimental results reported earlier [9].

The recovery of the wall mean velocity gradient was observed to be associated with the migration of the bubbles away from the boundary layer. The time scale of the migration is associated with the buoyant force and is consequently of longer duration for the smaller bubbles. The higher packing seems to be directly related to the extent to which the skin friction reduction persists downstream.

Another interesting feature reported in both [1] and [2] is that the bubble concentration or, in other words, the void fraction dies out as the boundary layer edge is approached. The measurements of the mean velocity profile in this part of the boundary layer show that it is not affected by the presence of the bubbles in the boundary layer. The LDA measurements in this region of the boundary layer, as presented in [8], are reproduced in Figure 1.6.

Finally, both the American and Soviet researchers report that the high frequency signals of the shear stress and pressure fluctuations close to the surface are lost with the injection of the gas.

1.2 Problem Statement

The problem analyzed in the following chapters has two distinct aspects, i.e., the stability of the bubble layer in the shear flow and the drag reduction.

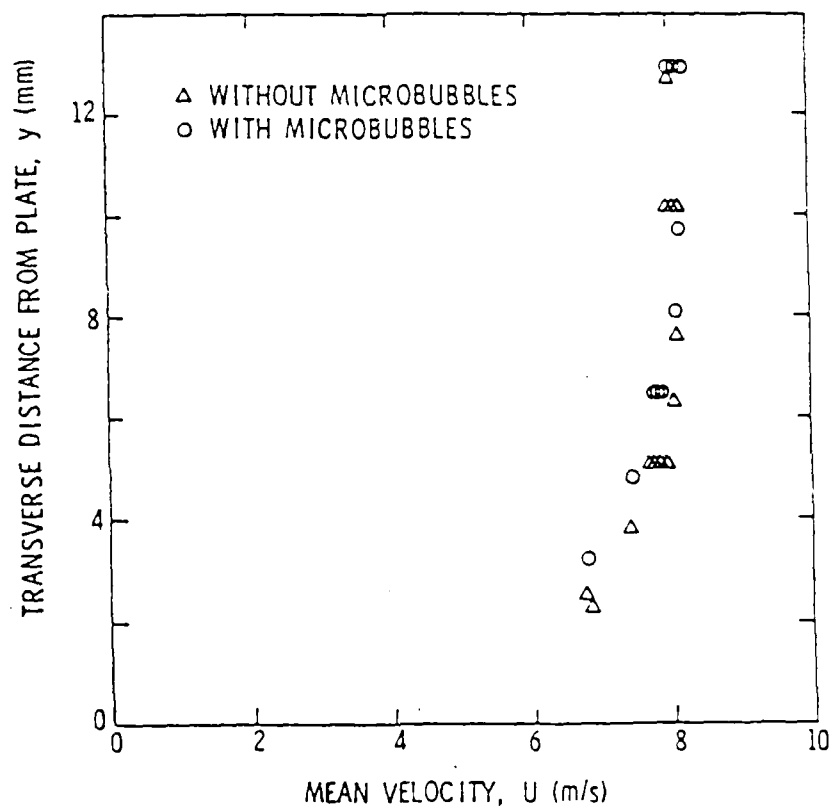


Figure 1.6. Comparison of Mean Velocity Profiles in the Outer Part of the Boundary Layer in the Presence and Absence of Microbubbles.

1.2.1 The Stability

In light of the brief discussion presented above, we see that the insertion of the bubble layer in the boundary layer appears to give rise to a sharp mean velocity variation across the bubble layer. The above statement is motivated by the fact that while promoting a decrease in the wall velocity gradient the bubbles do not affect the outer region of the boundary layer.

The fact that the bubble layer seems to be stable in the turbulent shear flow was to a certain extent surprising because of Helmholtz's classical result on vortex sheet unconditional instability.

The question of the stability is looked upon from several points of view. Given the two-dimensional nature of the boundary layer flow, the stability of a hollow vortex sheet is considered in the presence and in the absence of a wall. We study the problem from both an analytical and numerical point of view.

1.2.2 The Drag Reduction

As is clear from the description of the experimental results, the flowfield is rather complex and the mechanisms by which the drag reduction is brought about are not entirely clear.

Due to the small size of the bubbles and the two-dimensional nature of the flow, we adopt a phenomenological approach in which the fluid is assumed to have spatially varying properties. The obvious limitations of this model are discussed in Chapter IV.

CHAPTER II

STABILITY OF A HOLLOW VORTEX SHEET

2.1 Introduction

Helmholtz's classical result on the unconditional instability of a plane velocity discontinuity has been re-examined by several authors from both computational [10,11,12] and analytical [13] points of view.

In von Kármán's classical analysis (see Sir H. Lamb [13]), as well as in all subsequent works, the plane surface velocity discontinuity is modeled by a doubly infinite array of discrete vortices the circulation of which depends on the velocity jump across the surface. In addition to corroborating Helmholtz's result, von Kármán, in his elegant analysis, showed also that the presence of a wall has no influence on the vortex sheet so far as its stability is concerned.

In the following sections, we try to devise a simple model that may be representative of the two-phase phenomena observed and will give us a working base for the study of the stability. The two-dimensional nature of the boundary layer leads one naturally to imagine the bubbles as cylinders. In the realm of inviscid flows, we analyze the problem of the stability of a hollow vortex sheet from two different points of view.

In the following sections, we take the spirit of von Kármán's work and extend his analysis in order to consider hollow core vortices instead of point vortices. The main difference becomes the superposition on the original flowfield of the appropriate velocity potentials in order to guarantee the existence of

circular streamlines centered at each of the vortices. The circular streamlines are the surfaces of the cylinders which, in this two-dimensional framework, represent the bubbles.

2.2 A Simple Hollow Vortex Sheet

Sir Horace Lamb [19] reports that in an infinite expanse of fluid a vortex sheet moves with a velocity equal to the average of the velocities above and below the vortex sheet $\bar{U} = (U_1 + U_2)/2$. Furthermore, in [13] it is shown that a plane infinite row of vortices does not induce a velocity in itself. Similarly, one can show that a plane infinite row of dipoles induces a velocity field in itself given by $D\pi^2/3\lambda^2$, where D is the dipole strength and λ is the spacing between the dipoles.

The circulation of the vortices is uniquely determined by the average velocity across the vortex sheet \bar{U} as well as the spacing of the vortices, λ . From symmetry considerations, all the dipoles in the undisturbed state must have the same strength and orientation. Since the vortices are being displaced with a velocity \bar{U} , and the dipoles create a velocity field given by $D\pi^2/3\lambda^3$, the normal velocity condition at each hollow vortex is satisfied if,

$$D = \frac{R^2 \lambda^2}{1 - \frac{\pi^2 R^2}{3}} \quad (2.2.1)$$

where $R = a/\lambda$.

We notice that the dipole strength will be zero if either R or U are zero. In the following analysis, we assume that the small disturbance does not affect the dipole strength and orientation in a significant way. This assumption is acceptable because we are only interested in small disturbances.

According to Figure 2.1, the original position of the hollow vortices is given by $(m\lambda, 0)$ while the disturbed state is identified by $(x_m + m\lambda, y_m)$, where m is an integer. We now focus our attention on a typical vortex, say (x_o, y_o) , and investigate how the velocity field introduced by the disturbance affects the stability.

It can be easily shown that the velocity field created at a particular point, say (x_o, y_o) by the displaced system of dipoles and vortices is given by

$$\left. \frac{dx_o}{dt} \right|_v = \frac{-\gamma}{2\pi\lambda^2} \sum_m \frac{y_o - y_m}{m^2} \quad , \quad (2.2.2a)$$

$$\left. \frac{dy_o}{dt} \right|_v = \frac{-\gamma}{2\pi\lambda^2} \sum_m \frac{x_o - x_m}{m^2} + \frac{\gamma}{2\pi\lambda^2} \sum_m \frac{1}{m} \quad , \quad (2.2.2b)$$

$$\left. \frac{dx_o}{dt} \right|_d = \frac{2D}{\lambda^3} \sum_m \frac{x_o - x_m}{m^3} + \frac{D}{\lambda^3} \sum_m \frac{1}{m^2} \quad , \quad (2.2.2c)$$

and

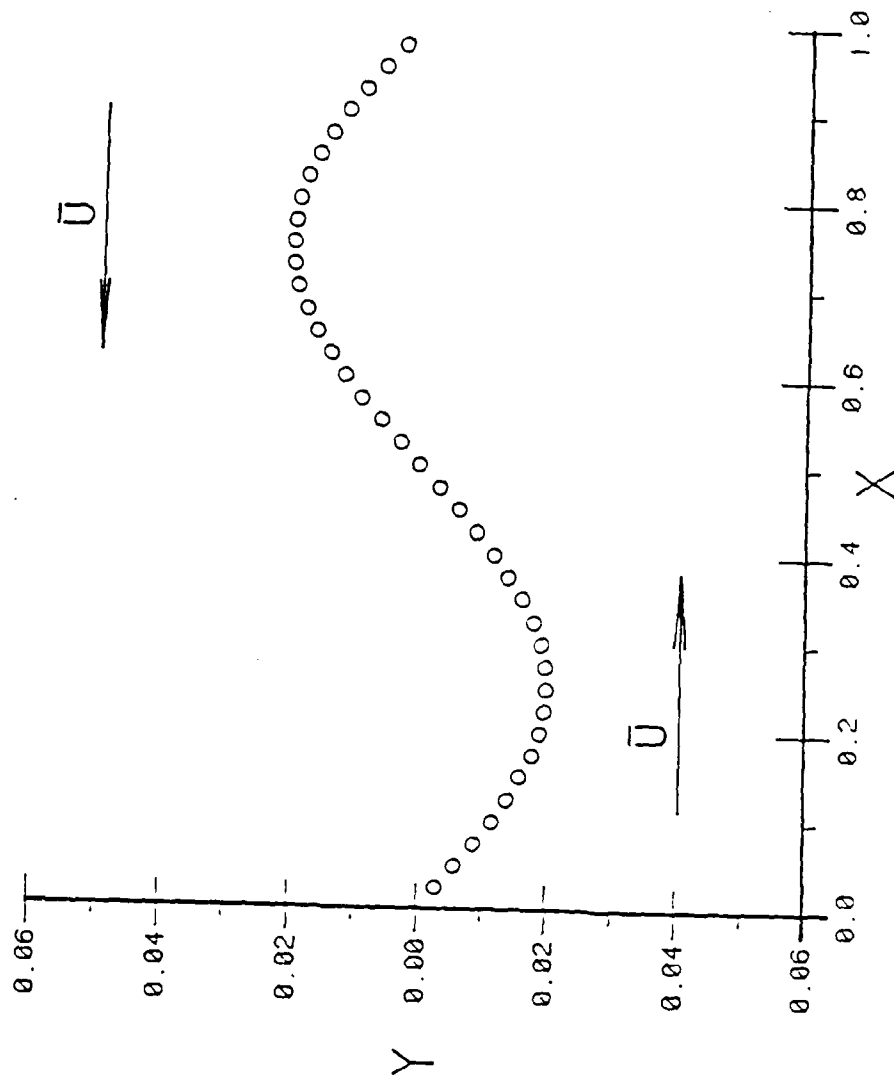


Figure 2.1. A Simple Hollow Vortex Sheet.

$$\left. \frac{dy_o}{dt} \right|_d = - \frac{2D}{\lambda^3} \sum_m \frac{y_o - y_m}{m^3}, \quad (2.2.3b)$$

where, in these expressions, only the first order terms in the displacements have been kept. Putting these contributions together, one finds the velocity components at the hollow vortex (x_o, y_o) to be

$$\frac{dx_o}{dt} = \frac{-\gamma}{2\pi\lambda^2} \sum_m \frac{y_o - y_m}{m^2} + \frac{2D}{\lambda^3} \sum_m \frac{x_o - x_m}{m^3}, \quad (2.2.4a)$$

and

$$\frac{dy_o}{dt} = \frac{-\gamma}{2\pi\lambda^2} \sum_m \frac{x_o - x_m}{m^2} - \frac{2D}{\lambda^3} \sum_m \frac{y_o - y_m}{m^3}, \quad (2.2.4b)$$

where our reference system moves with the rigid body velocity of the vortices and dipoles.

Following von Kármán, we consider disturbances of the type,

$$x_m = x_o e^{im\theta}; \quad y_m = y_o e^{im\theta} \quad (2.2.5)$$

where $0 < \theta < 2\pi$. With this the system of equations can be transformed into

$$\frac{dx_o}{dt} = - \frac{\gamma y_o}{2\pi\lambda^2} A_v(\theta) - \frac{2Dx_o}{\lambda^3} iA_d(\theta) \quad (2.2.6a)$$

$$\frac{dy_o}{dt} = -\frac{\gamma x_o}{2\pi\lambda^2} A_v(\theta) + \frac{2Dy_o}{\lambda^3} iA_d(\theta) \quad (2.2.6b)$$

where we have made use of the following series function representations:

$$A_v(\theta) = \frac{\theta}{2} (2\pi - \theta) = \sum_m \frac{1 - \cos m\theta}{m^2}, \quad (2.2.7a)$$

and

$$A_d(\theta) = \frac{\theta}{6} (\theta^2 - 3\pi\theta + 2\pi^2) = \sum_m \frac{\sin m\theta}{m^3}. \quad (2.2.7b)$$

Transcribing the system of equations to matrix notation, i.e.,

$$[X] = [C][X] \quad (2.2.8)$$

and assuming its solution to be of the form,

$$[X] = [Y]e^{\lambda t} \quad (2.2.9)$$

one finds that the problem is reduced to finding the eigenvalues of the matrix $[C]$. These are

$$\lambda_{1,2} = \pm \sqrt{\left(\frac{\gamma A_v}{2\pi\lambda^2}\right)^2 - \left(\frac{2DA_d}{\lambda^3}\right)^2}. \quad (2.2.10)$$

As expected, we see that in the limit of vanishing core radius we recover von Kármán's result of unconditional instability of a simple vortex sheet. If we define a nondimensional parameter given by $\zeta = \gamma\lambda/2\pi D$, then the simple hollow vortex sheet will be stable if

$$\zeta^2 - \left(\frac{2A_d}{A_v}\right)^2 < 0, \quad (2.2.11)$$

is satisfied for all frequencies of the disturbance. We see that for $\theta = \pi$ the stability interval is reduced to zero, thus there is no range of combinations of circulation, vortex spacing or dipole strength that can make the hollow vortex sheet stable.

2.3 A Symmetric Hollow Vortex Sheet

In the realm of potential flow theory, another possible explanation for the apparent stability of the bubble layer is presence of the wall. With the same underlying assumptions as in the last section, we attempt to consider the presence of the wall. The wall is located at a distance $b/2$ from the initially undisturbed hollow vortex sheet. The zero normal wall velocity boundary condition is satisfied by considering the image system as shown in Figure 2.2.

In the same way that a vortex sheet in the presence of a wall induces a velocity in itself [13], so does a dipole sheet. Consequently, the hollow vortices in the disturbed system will be identified by $(m\lambda + (U_v + U_d)t + x_m, b/2 + y_m)$ for the upper row and $(n\lambda + (U_v + U_d)t + x_m, -b/2 + y_m)$ for the lower row, where U_v and U_d are the velocities induced by the vortex and dipole systems in themselves, respectively.

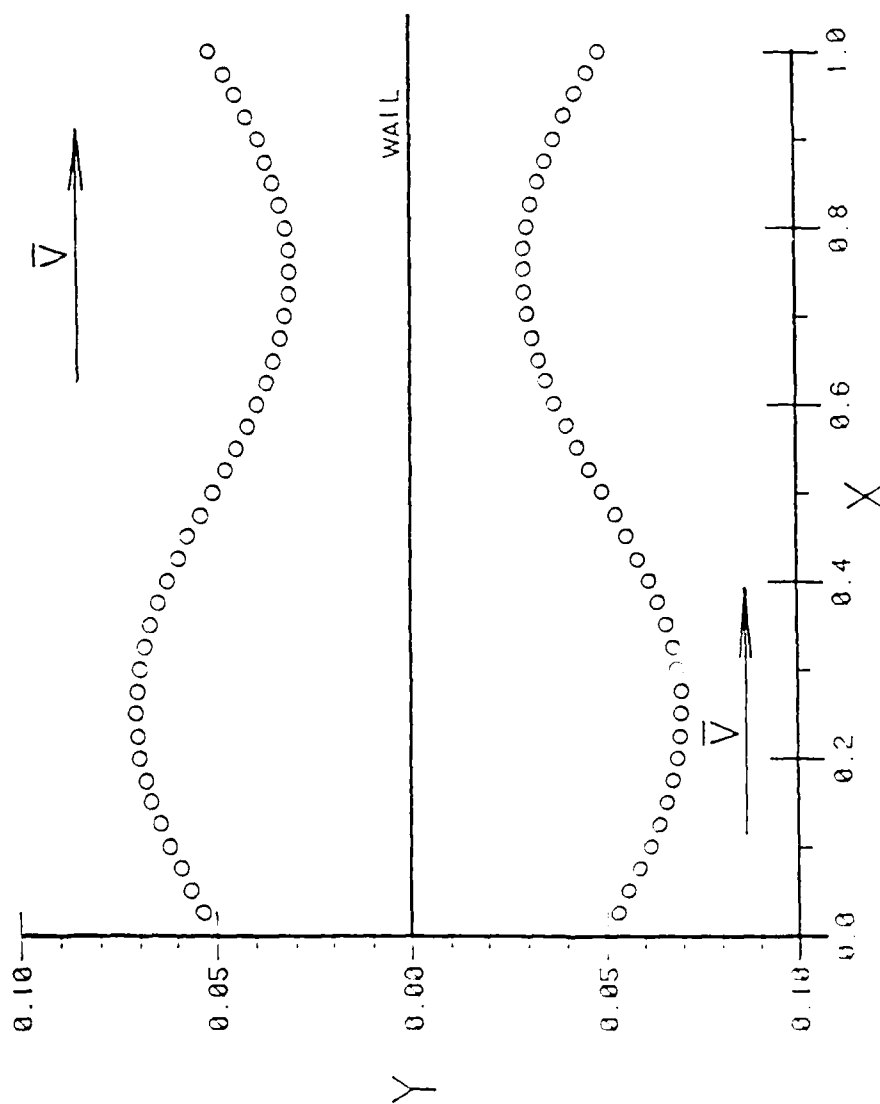


Figure 2.2. A Symmetric Hollow Vortex Sheet.

Directing our attention to the hollow vortex (x_o, y_o) in the upper row of hollow vortices, one can show after some algebra, that the components of the velocity field created by the lower row of vortices and dipoles are given by

$$\begin{aligned} \left. \frac{dx_o}{dt} \right|_v &= \frac{-\gamma}{2\pi} \sum_n \frac{b}{(n^2 \lambda^2 + b^2)^2} - \frac{\gamma}{2\pi} \sum_n \frac{(n^2 \lambda^2 - b^2)}{(n^2 \lambda^2 + b^2)^2} (y_o - y_n) \\ &\quad - \frac{-\gamma}{2\pi} \sum_n \frac{2n\lambda b}{(n^2 \lambda^2 + b^2)^2} (x_o - x_n) \quad , \end{aligned} \quad (2.3.1a)$$

$$\begin{aligned} \left. \frac{dy_o}{dt} \right|_v &= \frac{-\gamma}{2\pi} \sum_n \frac{n^2 \lambda^2 - b^2}{(n^2 \lambda^2 + b^2)^2} (x_o - x_n) \\ &\quad + \frac{\gamma}{2\pi} \sum_n \frac{2n\lambda b}{(n^2 \lambda^2 + b^2)^2} (y_o - y_n) \quad , \end{aligned} \quad (2.3.1b)$$

$$\begin{aligned} \left. \frac{dx_o}{dt} \right|_d &= D \sum_n \frac{n^2 \lambda^2 - b^2}{(n^2 \lambda^2 + b^2)^2} + D \sum_n \frac{2n\lambda(n^2 \lambda^2 - 3b^2)}{(n^2 \lambda^2 + b^2)^3} (x_o - x_n) \\ &\quad - 2D \sum_n \frac{b(3n^2 \lambda^2 - b^2)}{(n^2 \lambda^2 + b^2)^3} (y_o - y_n) \quad , \end{aligned} \quad (2.3.2a)$$

and

$$\begin{aligned} \left. \frac{dy_o}{dt} \right|_d &= 2D \sum_n \frac{n\lambda(3b^2 - n^2\lambda^2)}{(n^2\lambda^2 + b^2)^3} (y_o - y_n) \\ &- 2D \sum_n \frac{b(3n^2\lambda^2 - b^2)}{(n^2\lambda^2 + b^2)^3} (x_o - x_n) \end{aligned} \quad , \quad (2.3.2b)$$

respectively.

In looking at our typical vortex, which is located in the upper row, we also have to take into account the contribution of the upper row to the flowfield. This contribution is expressed by Eq. (2.2.2) and Eq. (2.2.3), where the vortices have the opposite orientation in order to satisfy the zero normal wall velocity boundary condition. Thus, the equations for the velocity components of the hollow vortex identified by (x_o, y_o) become

$$\frac{dx_o}{dt} = \frac{\gamma}{2\pi\lambda^2} \sum_m \frac{y_o - y_m}{m^2} + \frac{2D}{\lambda^3} \sum_m \frac{x_o - x_m}{m^3} + \left. \frac{dx_o}{dt} \right|_d + \left. \frac{dx_o}{dt} \right|_v \quad , \quad (2.3.3a)$$

and

$$\frac{dy_o}{dt} = \frac{\gamma}{2\pi\lambda^2} \sum_m \frac{x_o - x_m}{m^2} - \frac{2D}{\lambda^3} \sum_m \frac{y_o - y_m}{m^3} + \left. \frac{dy_o}{dt} \right|_d + \left. \frac{dy_o}{dt} \right|_v \quad , \quad (2.3.3b)$$

where the rigid body contributions from the vortices and dipoles have been subtracted. The rigid body velocity of the system is given by

$$\frac{D\pi^2}{3\lambda^2} + \frac{\lambda}{2\lambda} \coth\left(\frac{\pi b}{\lambda}\right) - \frac{\pi^2 D}{\lambda^2} \operatorname{csch}^2\left(\frac{\pi b}{\lambda}\right), \quad (2.3.4)$$

where, as can be easily shown [14],

$$\frac{\gamma}{2\lambda} \coth\left(\frac{\pi b}{\lambda}\right) = \frac{\gamma}{2\pi} \sum_n \frac{b}{n^2 \lambda^2 + b^2} \quad (2.3.5a)$$

and

$$\frac{\pi^2 D}{\lambda^2} \operatorname{csch}^2\left(\frac{\pi b}{\lambda}\right) = D \sum_n \frac{n^2 \lambda^2 - b^2}{(n^2 \lambda^2 + b^2)^2}. \quad (2.3.5b)$$

Again, following von Kármán, we define the following disturbances,

$$\begin{aligned} x_m &= x_o \ell^{im\theta} ; & y_m &= y_o \ell^{im\theta} ; \\ x_n &= \bar{x}_o \ell^{in\theta} ; & y_n &= \bar{y}_o \ell^{in\theta} \end{aligned} \quad (2.3.6)$$

for the upper and lower rows, respectively.

With the function representations of the resulting series (see Appendix A), we find

$$\begin{aligned} \frac{dx_o}{dt} &= y_o \left\{ \frac{\gamma}{2\pi\lambda^2} [A_v(\theta) - C_v(0)] - \frac{D}{\lambda^3} C_d(0) \right\} - ix_o \frac{2D}{\lambda^3} A_d(\theta) \\ &+ \bar{y}_o \left[\frac{\gamma}{2\pi\lambda^2} C_v(\theta) + \frac{D}{\lambda^3} C_d(\theta) \right] \\ &+ i\bar{x}_o \left[\frac{\gamma}{2\pi\lambda^2} B_v(\theta) + \frac{D}{\lambda^3} B_d(\theta) \right], \end{aligned} \quad (2.3.7a)$$

$$\begin{aligned}
\frac{dy}{d\tau} = & x_o \left\{ \frac{Y}{2\pi\lambda^2} [A_v(\theta) - C_v(0)] - \frac{D}{\lambda^3} C_d(0) \right\} + iy_o \frac{2D}{\lambda^3} A_d(\theta) \\
& + \bar{x}_o \left[\frac{Y}{2\pi\lambda^2} C_v(\theta) + \frac{D}{\lambda^3} C_d(\theta) \right] \\
& - i\bar{y}_o \left[\frac{Y}{2\pi\lambda^2} B_v(\theta) + \frac{D}{\lambda^3} B_d(\theta) \right] , \quad (2.3.7b)
\end{aligned}$$

where

$$B_v(\theta) = \frac{\pi\theta \cosh k(\pi - \theta)}{\sinh k\pi} - \frac{\pi^2 \sinh k\theta}{\sinh^2 k\pi} = \sum_n \frac{2nk \sin n\theta}{(n^2 + k^2)^2} , \quad (2.3.8a)$$

$$\begin{aligned}
B_d(\theta) &= -\frac{2\pi^3 \cosh k\pi}{\sinh^3 k\pi} \sinh k\theta + \frac{2\pi^2 \theta \cosh k\theta}{\sinh^2 k\pi} + \frac{\pi\theta^2 \sinh k(\pi - \theta)}{\sinh k\pi} \\
&= \sum_n \frac{2n(3k^2 - n^2)}{(n^2 + k^2)^3} \sin n\theta , \quad (2.3.8b)
\end{aligned}$$

$$\begin{aligned}
C_d(\theta) &= -\frac{2\pi^3 \cosh k\pi}{\sinh^3 k\pi} \cosh k\theta + \frac{2\pi^2 \theta \sinh k\theta}{\sinh^2 k\pi} - \frac{\pi\theta^2 \cosh k(\pi - \theta)}{\sinh k\pi} \\
&= \sum_n \frac{2k(3n^2 - k^2)}{(n^2 + k^2)^3} \cos n\theta , \quad (2.3.8c)
\end{aligned}$$

$$C_v(\theta) = -\frac{\pi^2 \cosh k\theta}{\sinh^2 k\pi} - \frac{\pi \theta \sinh k(\pi - \theta)}{\sinh k\pi} = \frac{2}{n} \frac{(n^2 - k^2)}{(n^2 + k^2)^2} \cos n\theta ,$$

(2.3.8d)

and $k = b/\lambda$.

As in the problem of a simple symmetric vortex sheet there are two types of solutions for the system of equations (2.2.7), i.e.,

$$\begin{aligned} \frac{dx_o}{dt} = y_o \left\{ \frac{\gamma}{2\pi\lambda^2} [A_v(\theta) - C_v(0) - C_v(\theta)] - \frac{D}{\lambda^3} [C_d(0) + C_d(\theta)] \right\} \\ + x_o i \left\{ \frac{\gamma}{2\pi\lambda^2} B_v(\theta) + \frac{D}{\lambda^3} [B_d(\theta) - 2A_d(\theta)] \right\} , \end{aligned} \quad (2.3.9a)$$

$$\begin{aligned} \frac{dy_o}{dt} = x_o \left\{ \frac{\gamma}{2\pi\lambda^2} [A_v(\theta) - C_v(0) + C_v(\theta)] - \frac{D}{\lambda^3} [C_d(0) - C_d(\theta)] \right\} \\ + y_o i \left\{ \frac{\gamma}{2\pi\lambda^2} B_v(\theta) + \frac{D}{\lambda^3} [2A_d(\theta) + B_d(\theta)] \right\} , \end{aligned} \quad (2.3.9b)$$

for $\bar{x}_o = x_o$ and $\bar{y}_o = -y_o$ and ,

$$\begin{aligned} \frac{dx_o}{dt} = y_o \left\{ \frac{\gamma}{2\pi\lambda^2} [A_v(\theta) - C_v(0) + C_v(\theta)] - \frac{D}{\lambda^3} [C_d(0) - C_d(\theta)] \right\} \\ - x_o i \left\{ \frac{D}{\lambda^3} [B_d(\theta) + 2A_d(\theta)] + \frac{\gamma}{2\pi\lambda^2} B_v(\theta) \right\} , \end{aligned} \quad (2.3.10a)$$

$$\begin{aligned} \frac{dy_o}{d\tau} = x_o \left\{ \frac{\gamma}{2\pi\lambda^2} [A_v(\theta) - C_v(0) - C_v(\theta)] - \frac{D}{\lambda^3} [C_d(0) + C_d(\theta)] \right\} \\ + y_o i \left\{ \frac{D}{\lambda^3} [2A_d(\theta) - B_d(\theta)] - \frac{\gamma}{2\pi\lambda^2} B_v(\theta) \right\} \quad , \quad (2.3.10b) \end{aligned}$$

for $\bar{x}_o = -\bar{x}_o$ and $\bar{y}_o = y_o$.

We realize immediately that if we take away the dipole contributions the two systems above reduce to those of von Kármán's as reported in [13]. Each of the two systems of equations can be written in matrix form as represented by Eq. (2.2.8). If a solution of the form of Eq. (2.2.9) is also assumed, the stability condition, which turns out to be the same for the systems (2.3.9) and (2.3.10), can be easily found to be

$$\begin{aligned} \zeta^2 \{ [A_v(\theta) - C_v(0)]^2 - C_v(\theta)^2 \} - 2\zeta \{ C_d(\theta)C_v(\theta) \\ + C_d(0) [A_v(\theta) - C_v(0)] \} + [C_d(0)^2 - C_d(\theta)^2 - 4A_d(\theta)^2] < 0 \quad , \end{aligned} \quad (2.3.11)$$

where $\zeta = \gamma\lambda/2\pi D$.

The stability of the system, which has to be satisfied for all $\theta \in [0, 2\pi)$ depends on the initial wall distance of the vortices ($b/2$) as well as the wavelength of the disturbance (λ). This dependency, expressed by the dimensionless parameter k , determines

the stability envelope given in Figure 2.3. The shape of the stability curves suggests that the presence of the wall has a very strong stabilizing influence on the hollow vortex sheet. We also note that the result of unconditional instability for a hollow vortex sheet, obtained in the last section, is recovered just a few wavelengths away from the wall.

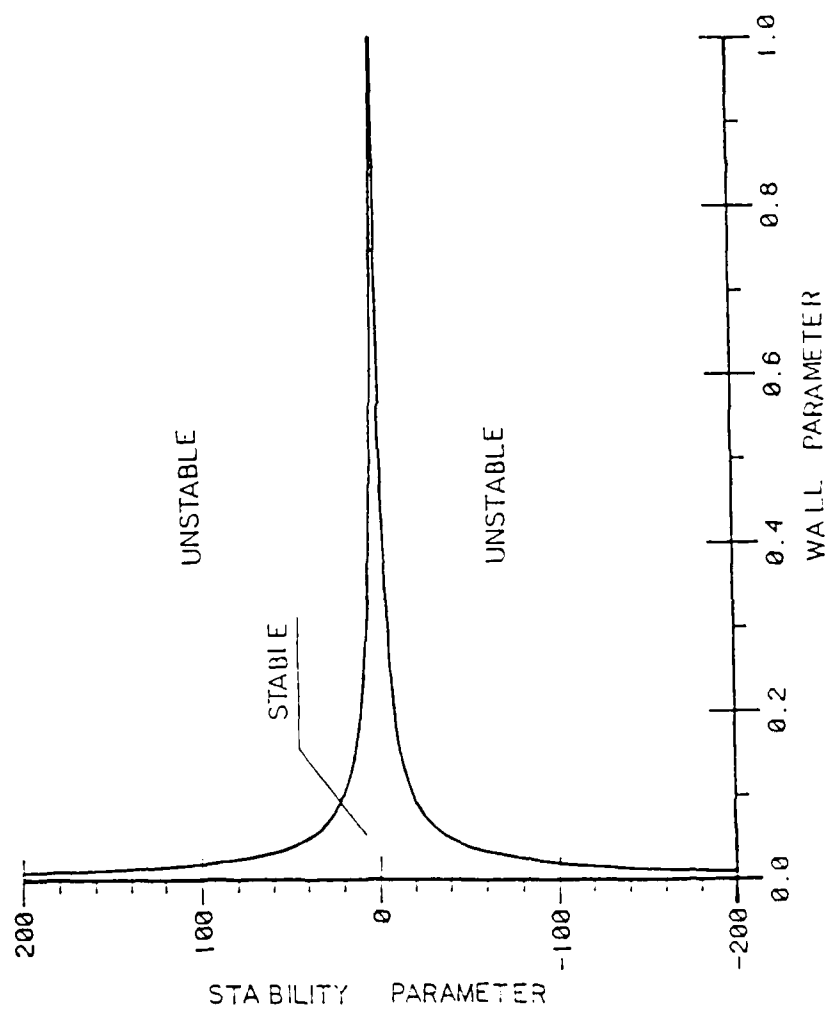


Figure 2.3. Stability Envelope for a Symmetric Hollow Vortex Sheet.

CHAPTER III

EVOLUTION OF A HOLLOW VORTEX SHEET

3.1 Introduction

The results obtained in the last section can be observed qualitatively from the numerical evolution of the hollow vortex sheet submitted to an initial disturbance. The numerical results stem from the consideration of the full nonlinear equations of motion. Even though more complex, the following development has the advantage of looking at the problem from a dynamical point of view.

The solution presented below follows the conceptual approach and the steps of D. Rosenhead [12], who by making use of von Kármán's analysis, tried to compute for the first time the evolution of a vortex sheet. It is known today [10] that Rosenhead's computations were incorrect. Indeed, some authors believe that the discrete vortex representation of a surface velocity discontinuity may not be appropriate. Nevertheless, this has been the approach used by C. Y. Chow [11] and R. F. Hama, et al. [10] to compute the evolution of the vortex sheet. The latter authors point out interesting first order vorticity effects that had been disregarded in all previous analyses and which cannot be accounted for in the vortex representation of the surface velocity discontinuity. Through a simple model they also looked at how the background vorticity affects the evolution of the vortex sheet.

The analysis presented below is suggested in the first chapter of a most interesting dissertation by G. R. Baker [15] on vortex dynamics.

As in the last chapter, we attempt to model the hollow vortices by using dipoles. In contrast with Chapter II, however, the orientation and strength of the dipoles depends on the characteristics of the flowfield past each of the hollow vortices, vide Figure 3.1.

There are two characteristic lengths in the problem, i.e., the cylinder radius (a) and the wavelength (λ). Since the ratio of the hollow core radius to the wavelength ($\alpha = \pi a/\lambda$) is very small, we will take into account only the first order contribution of the disturbance to the solution. From Helmholtz's theorems it follows that to solve the point vortex problem one needs only to take into account the kinematics of the flowfield. To solve the problem of the hollow vortices, however, one must consider both the kinematics and the dynamics of the system of hollow vortices. The forces created by the flowfield on each of the hollow vortices will determine their evolution which in turn determines the dipole strength and orientation.

3.2 The Dipole Strength of the System

Since the flowfield under consideration is a two-dimensional inviscid and irrotational flow, one can define both a streamfunction (ψ) and a velocity potential (ϕ). The complex potential is defined in the usual way,

$$W(z) = \phi(x,y) + i\psi(x,y) \quad , \quad (3.3.1)$$

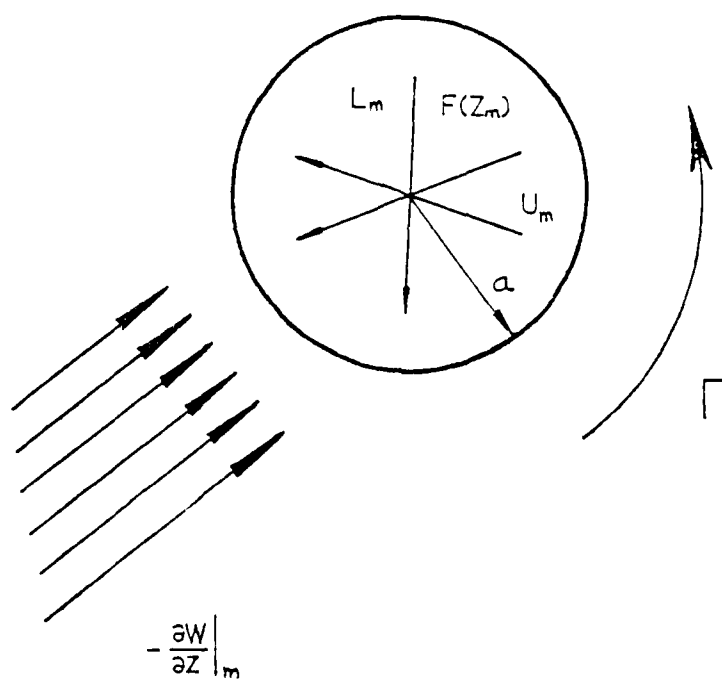


Figure 3.1. Flow Field Variables at the m^{th} Hollow Vortex.

and the complex velocity is obtained by taking the derivative of $W(z)$ with respect to z . The velocity components then relate to the streamfunction and the velocity potential by the Cauchy-Riemann conditions.

It can be easily shown [16] that the complex potentials of a dipole and a vortex, located at z_0 , are given by

$$W_d(z) = D/(z - z_0) \quad (3.3.2a)$$

and

$$W_v(z) = i\Gamma \log(z - z_0) \quad (3.3.2b)$$

respectively. In Eq. (3.3.2b), $\Gamma = \gamma/2\pi$ and the positive sense is taken as the counterclockwise. From expression (3.3.2a) we notice that the dipole strength D is proportional to a^2 , i.e., $D = La^2$.

The complex potential of a plane infinite row of vortices can be shown [16] to be given analytically by

$$W_{v_\infty}(z) = i\Gamma \log \left[\sin \frac{\pi}{\lambda} (z - z_0) \right] \quad (3.3.3)$$

where z_0 represents the position of the vortex closest to the origin and λ the distance between vortices, vide Figure 2.1. From the application of the Circulation Theorem over one wavelength of the vortex sheet, we find that $\Gamma = \bar{U}\lambda/\pi N$, where N is the number of hollow vortices contained in one wavelength of the disturbance.

If we differentiate Eq. (2.3.2b) and compare it with Eq. (2.3.2a), we conclude that

$$W_d(z) = -\frac{iD}{\Gamma} \frac{dW_v}{dz}(z) \quad (3.3.4)$$

Since the complex velocity potential of an infinite row of vortices is obtained by superposing the velocity potentials of each of the vortices, we can write

$$W_{d_{\infty}}(z) = -\frac{iD}{\Gamma} \frac{dW_{v_{\infty}}(z)}{dz} = \frac{D\pi}{\lambda} \cot \frac{\pi}{\lambda} (z - z_0) \quad . \quad (3.3.5)$$

Thus, the complex velocity fields created by a plane infinite row of dipoles and vortices are given in closed analytic form by

$$\frac{dW_{v_{\infty}}}{dz} = \frac{i\Gamma\pi}{\lambda} \cot \frac{\pi}{\lambda} (z - z_0) \quad , \quad (3.3.6a)$$

$$\frac{dW_{d_{\infty}}}{dz} = -\frac{D\pi^2}{\lambda^2} \csc^2 \frac{\pi}{\lambda} (z - z_0) \quad , \quad (3.3.6b)$$

respectively.

Since we are working with a potential flowfield, we are ultimately solving Laplace's equation, for which both the real and imaginary parts of each of the above complex potentials are solutions. In this case, the superposition principle is valid and the complex potential of the whole flowfield will be composed of contributions of the infinite rows of dipoles and vortices as well as their images in each of the hollow vortices.

As in the case of the simple point vortex system, the resulting equations are nonlinear. In order to keep the analysis within bounds, we are forced to consider only the leading contribution of the hollow vortices to the flowfield. To evaluate the order of magnitude of the contribution of the image system, we invoke Milne and Thomson's Circle Theorem [17] and look at the image system of a dipole and a vortex in

the presence of a cylinder. In the two simple cases of a cylinder located at the origin and a dipole or a vortex located at z_0 , we find that the complex velocities can be expressed as

$$\left. \frac{dW}{dz} \right|_d = \frac{-D}{(z - z_0)^2} + \frac{D}{z^2} \left(\frac{a}{z_0} \right)^2 \left[1 + \frac{2a^2}{z_0^2 z} + \dots \right], \quad (3.3.7a)$$

and

$$\left. \frac{dW}{dz} \right|_v = \frac{i\Gamma}{(z - z_0)} - \frac{i\Gamma a^2}{z_0^2 z^2} \left[1 + \frac{a^2}{z_0^2 z} + \dots \right], \quad (3.3.7b)$$

respectively.

Since the dipole strengths (D) are of order a^2 , we conclude that to this order of approximation the image system due to the dipoles can be neglected while that of the vortices must be considered. Also, to this order of magnitude, we note that to take into account the contribution of the vortex image system is the same as to consider a dipole at the origin with a strength given by $i\Gamma a^2/\bar{z}_0$.

Since the flow under consideration satisfies the premises of the Circle Theorem, the complex potential of the image system of a plane row of vortices in a cylinder located at z_0 is given by

$$W_{v_k}(z) = i\Gamma \frac{\pi a^2}{\lambda^2} F_k(\bar{z}_0) \cot \frac{\pi}{\lambda} (z - z_0) \quad (3.3.8)$$

where the function $F_k(\bar{z}_0)$ depends on the position of all the other vortices and the index k denotes the row to which these vortices belong. It can be shown that [14],

$$F_k(\bar{z}_0) = \int_{-\infty}^{\infty} \frac{1}{\frac{\bar{z}_k - \bar{z}_0}{\lambda} + n} = \pi \cot \frac{\pi}{\lambda} (\bar{z}_k - \bar{z}_0). \quad (3.3.9)$$

With the above in mind, we recognize four major contributions to the flowfield complex potential:

- The complex potential of the infinite row of vortices.
- The complex potential of the image system of the vortices in each of the hollow vortices.
- The complex potential of the infinite row of dipoles.
- The complex potential of the flowfield due to the motion of the hollow vortices.

The last contribution is equivalent to the action in each of the hollow vortices of another dipole the strength of which depends on the velocity and the diameter of the hollow vortex and is given by

$$D = Ua^2, \quad (3.3.10)$$

where U is a complex number representing the velocity of the hollow vortex.

In the realm of potential flows, the complex potential of the whole flow field becomes

$$W(z) = \sum_{n=1}^N \{ i\Gamma \log \left[\sin \frac{\pi}{\lambda} (z - z_n) \right] + G_n \frac{\pi a^2}{\lambda} \cot \frac{\pi}{\lambda} (z - z_n) \} \quad (3.3.11)$$

where,

$$G_n = L_n + U_n - i \frac{\Gamma \pi}{\lambda} \sum_{\substack{k=1 \\ k \neq n}}^N \cot \frac{\pi}{\lambda} (\bar{z}_n - \bar{z}_k) \quad (3.3.12)$$

The flow velocity at the center of each of the vortices can be found to be

$$\begin{aligned} \frac{\partial W}{\partial z} \Big|_m &= \sum_{\substack{n=1 \\ n \neq m}}^N \left[i \frac{\pi \Gamma}{\lambda} \cot \frac{\pi}{\lambda} (z_m - z_n) - G_n \left(\frac{\pi a}{\lambda} \right)^2 \csc^2 \frac{\pi}{\lambda} (z_m - z_n) \right] \\ &\quad - \frac{G_m}{3} \left(\frac{\pi a}{\lambda} \right)^2 \quad m = 1, \dots, N, \end{aligned} \quad (3.3.13)$$

where the last term represents the velocity field created at the m^{th} hollow vortex by the dipoles in its own row.

In order to satisfy the zero normal velocity boundary condition at the surface of each of the hollow vortices, we must require that

$$\frac{\partial W}{\partial z} \Big|_m - L_m = 0 \quad m = 1, \dots, N. \quad (3.3.14)$$

This expression represents a linear system of N equations and N unknowns, which enables the computation, at each time step, of the dipole strengths of the system of hollow vortices. For a better understanding vide Figure 3.1 where the various quantities involved in the computation of the dipole strengths are shown schematically. To a first order of magnitude, the above equation reduces to

$$L_m = \frac{i \Gamma \pi}{\lambda} \sum_{\substack{n=1 \\ n \neq m}}^N \cot \frac{\pi}{\lambda} (z_m - z_n) \quad m = 1, \dots, N. \quad (3.3.15)$$

Thus, to a first order of magnitude, the dipole strengths are determined by the vortex flowfield. This is to be expected since in a two-dimensional flowfield the vortex velocity field vanishes as $1/z$ while the dipole velocity field vanishes as $1/z^2$.

The rate of change of the dipole strengths is given by

$$\frac{dL_m}{dt} = - \frac{i\Gamma\pi^2}{\lambda^2} \sum_{\substack{n=1 \\ n \neq m}}^N (U_m - U_n) \csc^2 \frac{\pi}{\lambda} (z_m - z_n) , \quad (3.3.16)$$

where again $m = 1, \dots, N$.

3.3 The Dynamics of the System

In order to track the motion of the hollow vortices, we look at their equations of motion. In complex variables, this corresponds to the application of Blasius Theorem [16]. It can be easily shown that, if one neglects the rotation of the boundary, the generalized form of Blasius Theorem reduces to

$$\begin{aligned} X - iY|_m = & -i\rho_\ell \int_{C_m} \frac{\partial \bar{W}}{\partial t} d\bar{z} + \frac{1}{2} i\rho_\ell \int_{C_m} \left(\frac{\partial W}{\partial z} \right)^2 dz \\ & + i\rho_\ell \bar{U}_m \int_{C_m} \frac{\partial W}{\partial z} dz + \rho_\ell A \frac{d\bar{U}_m}{dt} \quad m = 1, \dots, N , \quad (3.3.17) \end{aligned}$$

where the left hand side is the inertia term in appropriate complex notation and the right hand side arises from the integration of Euler's equations around a closed contour enclosing the body's cross section. In Eq. (3.3.17) C_m represents the contour of the cross section of the m^{th} hollow vortex. As is shown in Appendix B, each of the five terms of the above equation is found to give

$$-i\rho_\ell \int_{C_m} \frac{\partial \bar{W}}{\partial t} d\bar{z} = -2\pi\rho_\ell a^2 \frac{d\bar{G}_m}{dt} , \quad (3.3.18a)$$

$$\begin{aligned} \frac{i}{2} \rho_\ell \int_{C_m} \left(\frac{\partial W}{\partial z} \right)^2 dz = & - 2\pi i \rho_\ell \Gamma \left(\frac{\pi a}{\lambda} \right)^2 \sum_{\substack{n=1 \\ n \neq m}}^N (G_m - G_n) \csc^2 \frac{\pi}{\lambda} (z_m - z_n) \\ & + 2\pi \rho_\ell \Gamma^2 \frac{\pi}{\lambda} \sum_{\substack{n=1 \\ n \neq m}}^N \cot \frac{\pi}{\lambda} (z_m - z_n) , \end{aligned} \quad (3.3.18b)$$

$$i \rho_\ell \bar{U}_m \int_{C_m} \frac{\partial W}{\partial z} dz = - 2\pi i \rho_\ell \Gamma \bar{U}_m , \quad (3.3.18c)$$

$$\rho_\ell A \frac{d\bar{U}_m}{dt} = \pi \rho_\ell a^2 \frac{d\bar{U}_m}{dt} , \quad (3.3.18d)$$

$$X - iY|_m = \pi \rho_g a^2 \frac{d\bar{U}_m}{dt} , \quad (3.3.18e)$$

where $m = 1, \dots, N$.

Equations (3.3.18a) and (3.3.18d) account for the unsteadiness of the flow and are thus equivalent to the added or virtual mass term. Equation (3.3.18b) gives both the first and second order steady state flow contributions. In Eq. (3.3.18c), we recognize Kutta-Joukowski's Theorem [15].

In the limit of vanishing core radius, we find

$$\bar{U}_m = - i \Gamma \frac{\pi}{\lambda} \sum_{\substack{n=1 \\ n \neq m}}^N \cot \frac{\pi}{\lambda} (z_m - z_n) \quad m = 1, \dots, N , \quad (3.3.19)$$

which are exactly the equations of motion of the point vortices in a sheet as given by Sir Horace Lamb [13].

In dimensionless variables, the equations of motion reduce to a system of first order ordinary differential equations of the form

$$\begin{aligned} \alpha^2 \frac{d\bar{U}_m}{dt} &= S_m(\underline{U}, \underline{Z}) \\ \frac{d\bar{Z}_m}{dt} &= \bar{U}_m \end{aligned} \quad m = 1, \dots, N, \quad (3.3.20)$$

where \underline{U} and \underline{Z} represent the velocity and position arrays of the system of hollow vortices. In arriving at the system of Eqs. (3.3.20), we used the fact that $\rho_g/\rho_l \ll 1$. After some algebra, the source term S_m is found to be given by

$$\begin{aligned} S_m(\underline{U}, \underline{Z}) &= -\alpha^2 \frac{2\pi}{N} \{i + 2\text{Im}\} \left[\sum_{\substack{n=1 \\ n \neq m}}^N (U_m - U_n) \csc^2 \pi(z_m - z_n) \right] \\ &\quad - \frac{2\pi}{N} i \left[\bar{U}_m + \frac{i}{N} \sum_{\substack{n=1 \\ n \neq m}}^N \cot \pi(z_m - z_n) \right] \\ &\quad + \frac{4\pi i}{N^2} \alpha^2 \sum_{n=1}^N \{\text{Im}\} [P_m(\underline{Z})] \csc^2 \pi(z_m - z_n) \end{aligned}$$

$$m = 1, \dots, N. \quad (3.3.21)$$

where

$$P_m(\underline{Z}) = \sum_{\substack{j=1 \\ j \neq m}}^N \cot \pi(z_m - z_j) - \sum_{\substack{i=1 \\ i \neq n}}^N \cot \pi(z_n - z_i).$$

So, from Eq. (3.3.21), we recognize that in the system (3.3.20) there is actually imbedded the zeroth order problem that represents the motion of the point vortices.

In order to solve the system (3.3.20), given the initial position of the hollow vortices the zeroth order problem, represented by Eq. (3.3.19), determines the initial velocity of the hollow vortices. With the initial vectors \underline{U} and \underline{Z} , the corrections to the velocities of the system of vortices are computed from

$$\frac{d\bar{U}_m}{dt} = H_m(\underline{U}, \underline{Z}) \quad m = 1, \dots, N, \quad (3.3.22)$$

where

$$H_m(\underline{U}, \underline{Z}) = -\frac{2\pi}{N} (i + 2\text{Im}) \left[\sum_{\substack{n=1 \\ n \neq m}}^N (U_m - U_n) \csc^2 \pi(z_m - z_n) \right] \\ + \frac{4\pi i}{N^2} \sum_{\substack{n=1 \\ n \neq m}}^N \{\text{Im}\} [P_m(\underline{z})] \csc^2 \pi(z_m - z_n) \quad m = 1, \dots, N. \quad (3.3.23)$$

Integrating the second equation of the system (3.3.20) and using as the source term the result obtained from (3.3.22) one obtains the corrections for the the positions of system of hollow vortices. Thus, the new position for the hollow vortex sheet is described by

$$z_m = z_{om} + \alpha^2 z_{cm} \quad m = 1, \dots, N, \quad (3.3.24)$$

where z_{cm} is obtained as described above and z_{om} is the result of the integration of (3.3.19) and illustrated for one case in Figure 3.2.

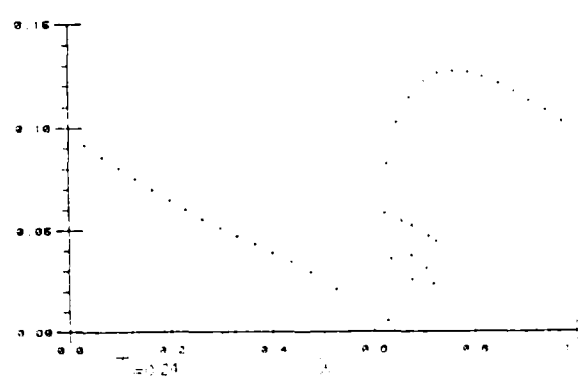
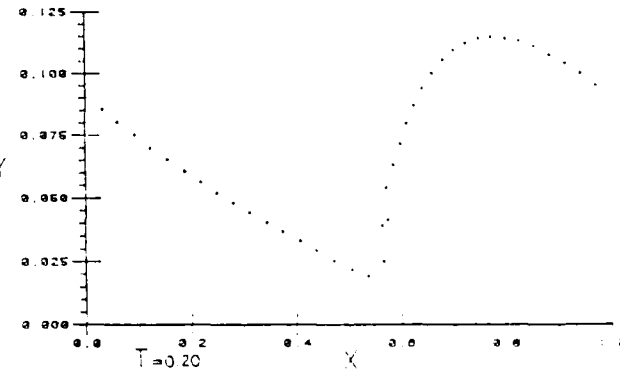
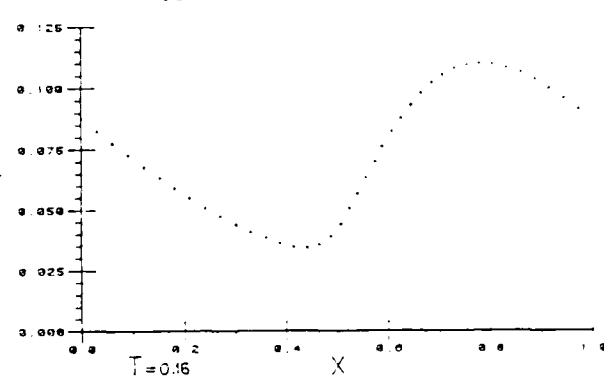
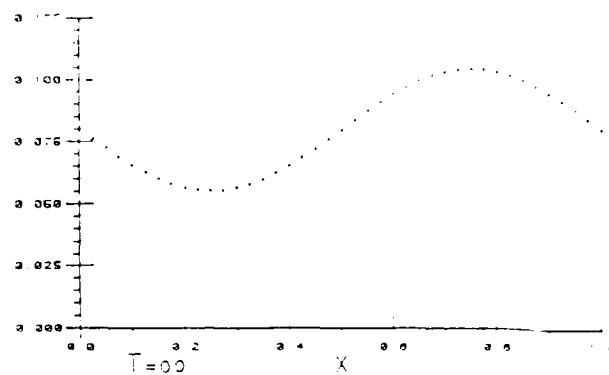
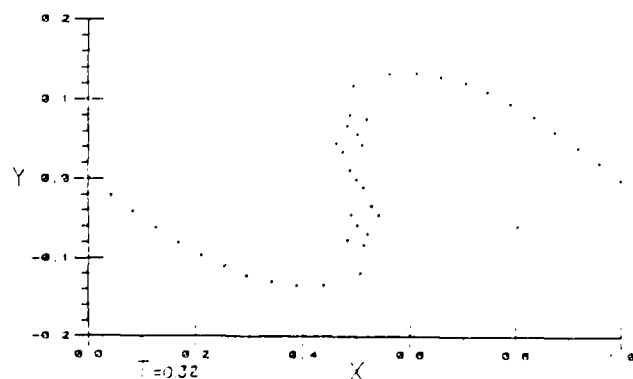
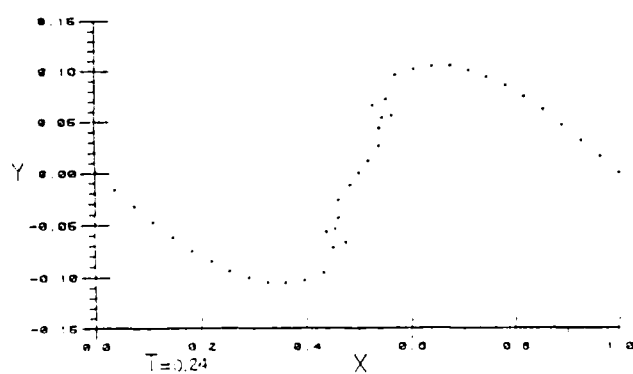
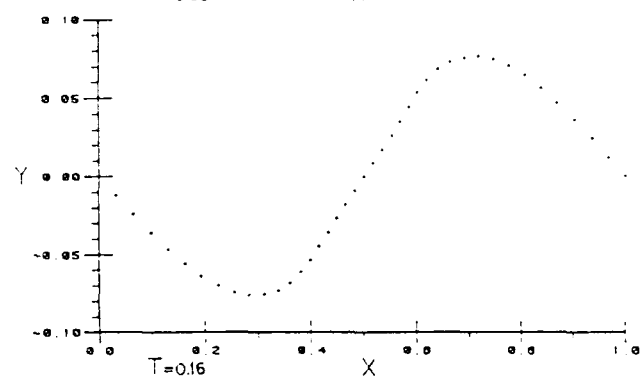
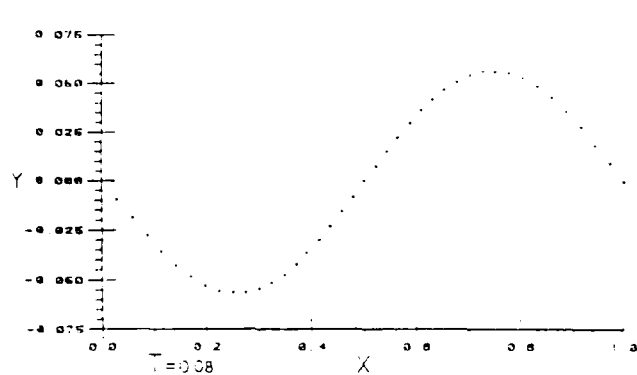


Figure 3.2. Evolution of a Simple Point Vortex Sheet starting with a Sinusoidal Deformation of Amplitude $\beta = 0.05$.

Figure 3.3. Evolution of a Simple Point Vortex Sheet in the Presence of a Sail, starting with a Sinusoidal Deformation of Amplitude $\beta = 0.025$ and $\kappa = 0.08$.

A fourth order Runge-Kutta solver was used to perform the computations described above. A flow chart as well as the code are included in Appendix C. Supporting our previous findings, comparison of Figures 3.2, 3.4 and 3.5 suggests that the consideration of the velocity field due to the dipoles is a destabilizing factor. The results indicate also that the larger the cylinder radius, the shorter the roll up time. In the two cases presented, the cylinder diameters make up 25% and 46% of the wavelength.

3.4 The Image System

Since the small disturbance analysis carried out in Chapter II suggests that the presence of the wall is the stabilizing factor of the hollow vortex sheet, we introduce an image system as illustrated in Figure 2.2.

With the complex potentials of a dipole and a vortex, located at z_0 , given by Eqs. (3.3.2), it is clear that the corresponding complex potential of the image system in a horizontal plane is given by

$$W_{d_i}(z) = \bar{D}/(z - \bar{z}_0) \quad , \quad (3.4.1a)$$

and

$$W_{v_i}(z) = -i\Gamma \log(z - \bar{z}_0) \quad , \quad (3.4.1b)$$

respectively. The bars, of course, mean the complex conjugate of the quantity.

With an analysis similar to that of the previous sections, one concludes that the complex potential of the hollow vortex sheet with the corresponding image system is given by

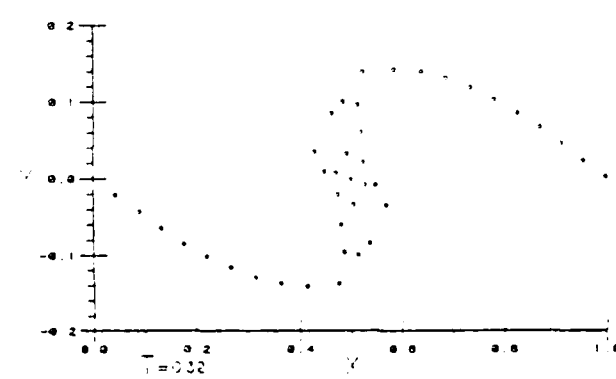
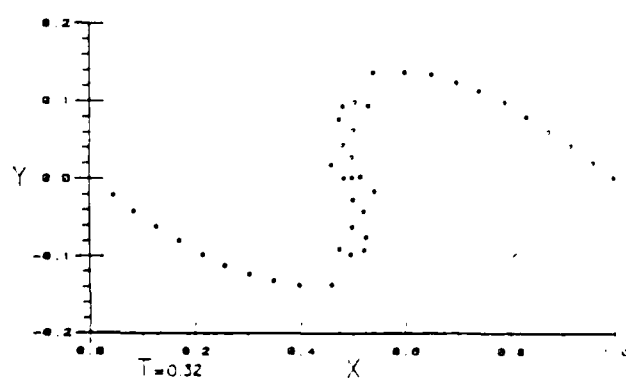
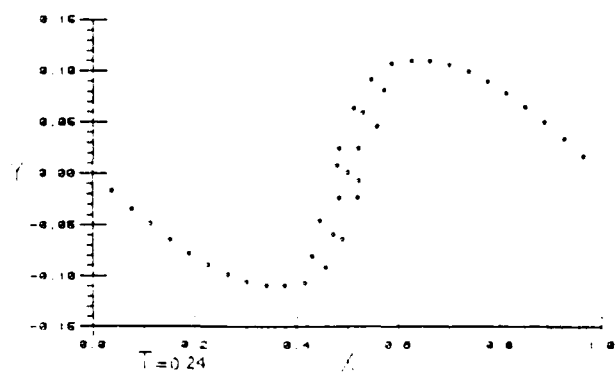
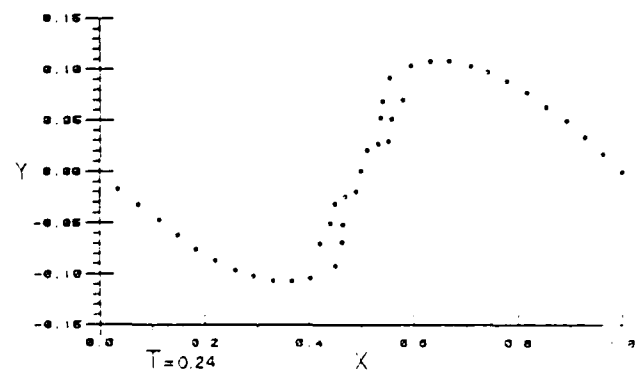
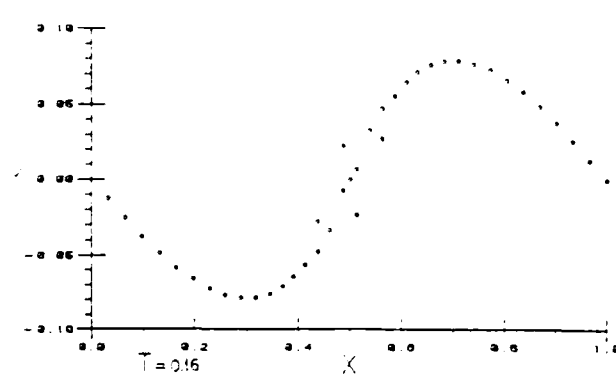
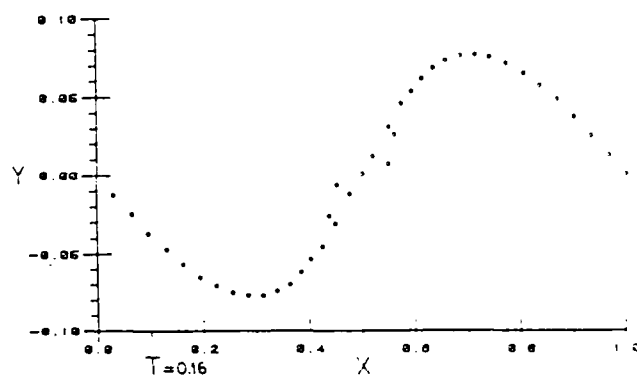
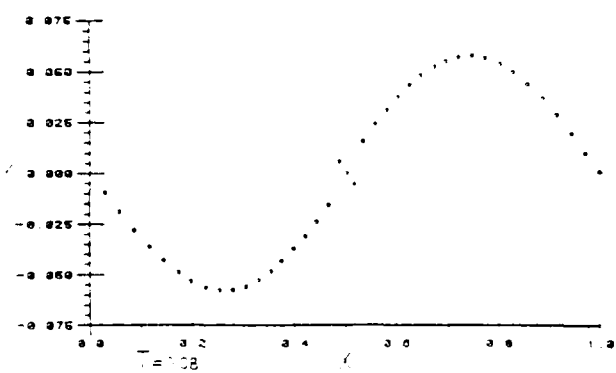
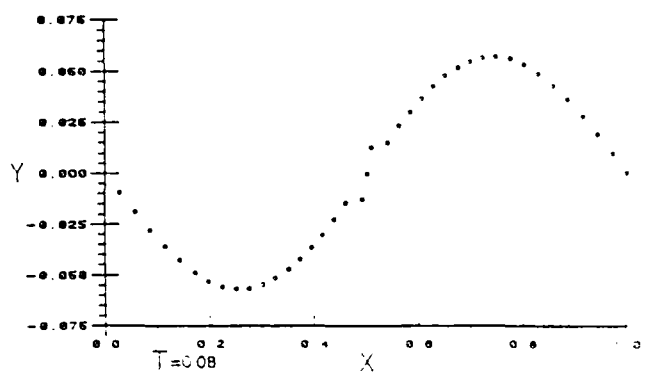


Figure 3.4. Evolution of a Simple Hollow Vortex Sheet starting with a Sinusoidal Deformation of Amplitude $B = 0.05$ and $\alpha = 0.01$.

Figure 3.5. Evolution of a Simple Hollow Vortex Sheet starting with a Sinusoidal Deformation of Amplitude $B = 0.05$ and $\alpha = 0.018$.

$$\begin{aligned}
W(z) = & \sum_{n=1}^N \{i\Gamma \log[\sin \frac{\pi}{\lambda} (z - z_n)] - i\Gamma \log[\sin \frac{\pi}{\lambda} (z - \bar{z}_n)] \\
& + G'_n \frac{\pi a^2}{\lambda} \cot \frac{\pi}{\lambda} (z - z_n) + \bar{G}'_n \frac{\pi a^2}{\lambda} \cot \frac{\pi}{\lambda} (z - \bar{z}_n)\} \quad (3.4.2)
\end{aligned}$$

where

$$\begin{aligned}
G'_n = & L'_n + U_n - i \frac{\Gamma\pi}{\lambda} \sum_{\substack{k=1 \\ k \neq n}}^N \cot \frac{\pi}{\lambda} (\bar{z}_n - \bar{z}_k) \\
& + i \frac{\Gamma\pi}{\lambda} \sum_{k=1}^N \cot \frac{\pi}{\lambda} (\bar{z}_n - z_k) \quad . \quad (3.4.3)
\end{aligned}$$

In the last expression, the last term stems from the image in each of the vortices of the wall image system.

Enforcing the zero normal velocity boundary condition at the surface of each of the hollow vortices, as expressed by Eq. (3.3.14), we find that for the symmetric hollow vortex sheet, to the first order magnitude, we have

$$\begin{aligned}
L'_m = & i \frac{\Gamma\pi}{\lambda} \left[\sum_{\substack{n=1 \\ n \neq m}}^N \cot \frac{\pi}{\lambda} (z_m - z_n) - \sum_{n=1}^N \cot \frac{\pi}{\lambda} (z_m - \bar{z}_n) \right] \\
m = & 1, \dots, N \quad . \quad (3.4.4)
\end{aligned}$$

With an argument identical to that of the last section, the motion of the hollow vortices in the presence of the wall is still governed by Eq. (3.3.17). Upon integration with the complex

potential as defined by Eq. (3.4.2), we conclude that only the term corresponding to Eq. (3.3.18b) is modified in the equations of motion, i.e.,

$$\begin{aligned}
 \frac{1}{2} i \rho_{\ell} \int_{C_m} \left(\frac{\partial W}{\partial z} \right)^2 dz &= 2 \pi \rho_{\ell} \Gamma^2 \frac{\pi}{\lambda} \left\{ \sum_{\substack{n=1 \\ n \neq m}}^N \cot \frac{\pi}{\lambda} (z_m - z_n) \right. \\
 &\quad - \sum_{n=1}^N \cot \frac{\pi}{\lambda} (z_m - \bar{z}_n) \left. \right\} + 2 \pi i \rho_{\ell} \Gamma \left(\frac{\pi a}{\lambda} \right)^2 \left\{ \sum_{n=1}^N (G'_m + \bar{G}'_n) \csc^2 \frac{\pi}{\lambda} (z_m - \bar{z}_n) \right. \\
 &\quad - \sum_{\substack{n=1 \\ n \neq m}}^N (G'_m - G'_n) \csc^2 \frac{\pi}{\lambda} (z_m - z_n) \left. \right\} \quad m = 1, \dots, N \quad (3.4.5)
 \end{aligned}$$

The other two integrals are not affected because the new functional terms added to the complex potential are always analytic inside the contour of integration and consequently vanish. While in the case of the hollow vortex sheet in an infinite expanse of fluid, the velocity scale is the farstream induced velocity (\bar{U}), in this case it is the rigid body velocity of the hollow vortex sheet (\bar{V}). Thus, the solution of the problem with the image system is still obtained through the system (3.3.20), where now the source term is given by

$$\begin{aligned}
S_m(\underline{U}, \underline{Z}) = & -2\pi\omega \left\{ -2 \sum_{\substack{n=1 \\ n \neq m}}^N \{ \text{Im} \} [(U_m - \bar{U}_n) \csc^2 \pi (z_m - \bar{z}_n)] \right. \\
& + \sum_{n=1}^N (U_m - U_n) \csc^2 \pi (z_m - z_n) \} \\
& + 2\pi i \omega \left\{ \sum_{n=1}^N (U_m + \bar{U}_n) \csc^2 \pi (z_m - \bar{z}_n) \right. \\
& - \sum_{\substack{n=1 \\ n \neq m}}^N (U_m - U_n) \csc^2 \pi (z_m - z_n) \} \\
& - 4\pi i \omega^2 \left\{ \sum_{n=1}^N \{ \text{Im} \} [P_m^*(\underline{Z}) + P_n^*(\underline{Z})] \csc^2 \pi (z_m - \bar{z}_n) \right. \\
& - \sum_{\substack{n=1 \\ n \neq m}}^N \{ \text{Im} \} [P_m^*(\underline{Z}) - P_n^*(\underline{Z})] \csc^2 \pi (z_m - z_n) \} \quad , \quad (3.4.6)
\end{aligned}$$

where

$$P_m^*(\underline{Z}) = \sum_{\substack{k=1 \\ k \neq m}}^N \cot \pi (z_m - z_k) - \sum_{k=1}^N \cot \pi (z_m - \bar{z}_k) \quad ,$$

and $m = 1, \dots, N$. In the above equation, $\omega = \pi\Gamma/\lambda\bar{V}$.

The zeroth order of magnitude problem is, of course, dictated by the complex potential of the symmetric arrangement of vortices. This complex potential falls out of Eq. (3.4.2) in the limit of vanishing hollow vortex radius. The corresponding complex velocity field is given by

$$\bar{U}_m = -i\omega \left\{ \sum_{\substack{n=1 \\ n \neq m}}^N \cot \pi(z_m - z_n) - \sum_{n=1}^N \cot \pi(z_m - \bar{z}_n) \right\}$$

$$m = 1, \dots, N, \quad (3.4.7)$$

where the indices refer to the vortices in the upper row.

The integration procedure for this problem is entirely identical to that described in the previous section. For computational convenience, but certainly to the detriment of the CPU time required, we used in both instances complex notation in the course of the computations.

The stability range of the symmetric hollow vortex sheet found in the last chapter imposes restrictions that cannot be satisfied if the physical dimensions of the cylinders are taken into account. In order to satisfy these impositions, we have to consider a very large number of vortices, which renders the computations impractical. According to Figure 2.3 a stable vortex hollow vortex sheet can be found farther away from the wall if the hollow vortex circulation is small enough. Once more the computations are impractical because the hollow cores only introduce a second order correction to the point vortex motion. As a consequence, we were unable to corroborate numerically the results found in Section 2.3.

The small size of the bubbles in the boundary layer suggests that they are endowed with a very small rotation. From the previous analysis the small circulation along with the presence of the wall are the key reasons for the apparent stability of the bubbles in the shear flow. Other contributing factors, which this analysis completely disregards, are the effect of viscosity which may be stabilizing and the presence of other bubble layers.

For illustration purposes, the evolution of a point vortex sheet in the presence of a wall is given in Figure 3.3. The pattern, clearly unstable, in support of von Kármán's conclusion [13], and is suggestive of the mechanism of drag reduction which we discuss in the next chapter.

CHAPTER IV

THE DRAG REDUCTION

4.1 Introduction

As mentioned in Chapter I, the promise of substantial skin friction reduction through boundary layer microbubble injection excited the interest of many engineers. The obvious potential applications of this concept of drag reduction led some of these researchers to attempt to model the boundary layer flow with microbubbles [18]. It should be noted that these attempts were of a probing nature. The aforementioned researchers claim to have only assessed the percentage of the drag reduction that can be attributed to a mean flow density and viscosity variation.

In the following, a more comprehensive attempt is presented. Like previous works, the direction adopted has shortcomings which are imposed by the extreme complexity of the flow with its poorly understood structure. Even though the modeling concept is basically the same, we think that if a phenomenological approach is to be adopted, then it should be built upon the rough model introduced in the following sections.

Some of the major difficulties that have to be dealt with in this problem in order to design a reliable code are:

- the fact that we have two phase flow,
- the large range of variation of the void fraction of the second phase in the flow,
- the interaction between the second phase in the flow and the turbulence structure of the carrier phase,

- the momentum transfer structure between the second phase and the mean flow in cross stream.

The solution of the above problems represents a major mathematical, numerical modeling and experimental effort. Part of this drive, mostly on the experimental side, has been underway at The Pennsylvania State University for sometime [6-8].

4.2 The Constitutive Relation

M. Ishii, in a most interesting monograph [19], discusses from first principles turbulent two phase flows and the mathematical tools within reach to describe them. From the complexity of the equations obtained, it is obvious, at least for the near future, that any hope of modeling these flows lies in the possibility of representing them as some kind of continuum single phase flow.

This being the only path open, it assumes the knowledge of the physical characteristics of the "fluid". This means that an experimental effort must be undertaken in order to study and establish a functional relationship between the viscosity of the "fluid" and the void fraction over large ranges. In other words, one must first find the appropriate constitutive relations for the "fluid".

To the author's knowledge, N. K Madavan, et al. [18] in their numerical study addressed this problem by representing the viscosity of the "fluid" by Einstein's relation [20,21], i.e.

$$\mu = \mu_l (1 + 2.5X) \quad , \quad (4.2.1)$$

as well as Sibree's viscosity model in order to provide an upper bound to the effects of density and viscosity variation. The validity of Eq. (4.2.1), which is obtained from theoretical hydrodynamic arguments, is restricted to small values of the void fraction, X . Even in this range, nevertheless, the experimental work of S. Hinata, et al. [22] suggests that Eq. (4.2.1) is not a good description of the functional dependence of the viscosity on the void fraction. The American researchers did not seem to be aware of this work by their Japanese colleagues. Indeed Figure 4.1 shows that Einstein's model is itself an upper bound for the viscosity when considered as a function of the void fraction. For this reason and the fact that in [4] the void fraction profiles are prescribed arbitrarily, the author thinks that the conclusions in [4] should be considered at most qualitatively.

Without delving into the merits of the experimental procedure used by S. Hinata, et al., we note two important facts:

The equation proposed by them as a constitutive relation dependent on the void fraction, i.e.,

$$\mu_{sp} = X(0.45 + 1.3X)Ta^{-1/6} \quad , \quad (4.2.2)$$

where $Ta = \mu_d(du/dy)/\sigma$, is based on void fractions that range up to 0.25. Even though based on this limited range of void fractions, there is reason to believe that Eq. (4.2.2) is valid in our flow. Our argument is connected to the coalescence and deformability of the bubbles. According to [18] this can be correlated to the non-dimensional number Ta with the conclusion that if $Ta > 0.15$,

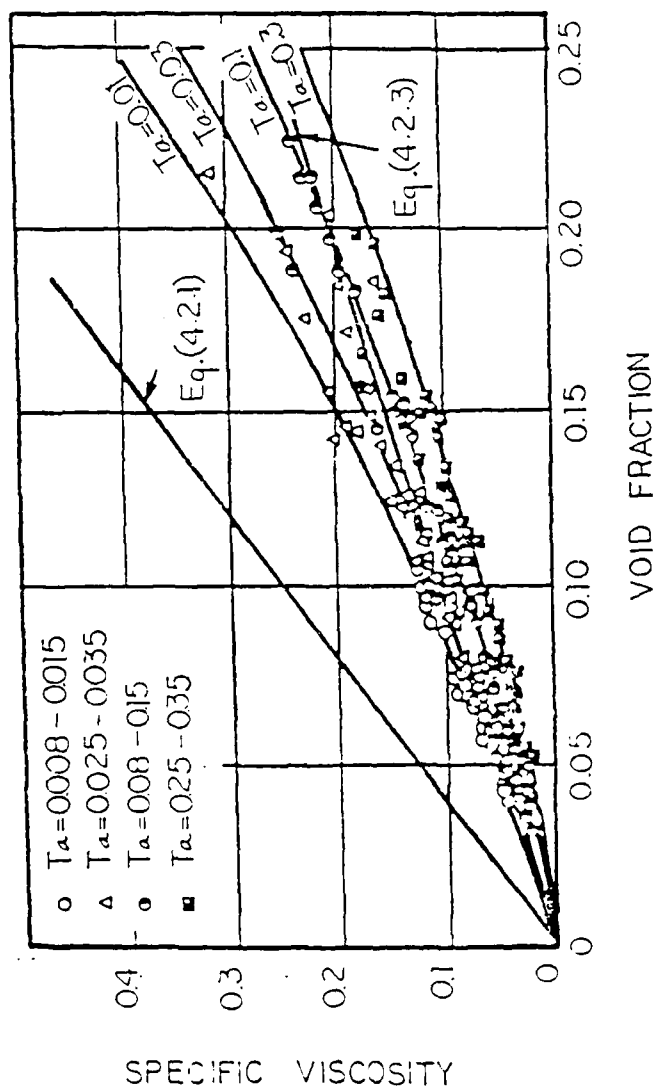


Figure 4.1. Relationship between the Specific Viscosity and the Void Fraction.

coalescence and deformability are prevalent, Eq. (4.2.2) is not valid. For a typical bubble in the present flow [8], we find that the parameter Ta is of order 10^{-2} . Some of their experimental findings, as well as the empirical relation (4.2.2), are reproduced in Figure 4.1.

At lower void fractions, the empirical relation (4.2.2) compares very favorably with Taylor's expression [23], see Figure 4.1,

$$\mu = 2.5X \left(\frac{\mu_g + \frac{2}{5} \mu_l}{\mu_g + \mu_l} \right) . \quad (4.2.3)$$

Consequently, Eq. (4.2.2) is used in our computations, even though we have no knowledge of how good it is at the higher void fractions of 0.8 reported by the Soviet researchers [2].

4.3 The Mechanisms of the Drag Reduction

Even though the mechanisms of the microbubble drag reduction are still unclear, we present here a chain of ideas that seems to be physically consistent in light of the experimental data available. The ideas presented will be used in Section 4.5 to modify the formulation of the Van Driest wall function.

M. K. Madavan, et al [18] uses, in his numerical studies, as the main mechanism to achieve the skin friction reduction, a modified Van Driest equation for the mixing length. The physical motivation of his expression, however, is obscure and in fact it does not capture one of the main characteristics of the drag

reduction by microbubble injection, i.e., the fact that it is a localized streamwise phenomenon. This is a consequence of the fact that the void fraction is arbitrarily prescribed in [4] and not computed.

The stability results of the past chapters suggest and the experimental results give credence to the idea that the drag reduction is a result of the dynamic interaction of the microbubbles with the macroscale turbulence structure of the boundary layer.

Since, downstream from the place of injection, the skin friction eventually recovers to its undisturbed value, it is obvious that the mere presence of the bubbles in the boundary layer is not responsible for the drag reduction. In fact, the streamwise distance over which the drag reduction is observed is rather limited [8]. Furthermore, the fact that the skin friction reduction depends on the volumetric flow rate of the gas being injected supports the last paragraph in two ways.

It was observed that [6,8]:

- The skin friction reduction is very small for small volumetric flow rates of the gas being injected.
- The skin friction reduction is partially lost if the volumetric flow rate of the gas being injected is increased beyond a specific quantity that depends on the free stream Reynolds number. In other words, for a given free stream Reynolds number, there is an optimum injection volume flow rate for maximum skin friction reduction.

These two facts, seemingly unrelated, have a common connection. In the first case, the lower bubble inertia, the larger diameter determines that the bubbles are forced to interchange momentum with the smaller turbulence eddies closer to the wall. This, allied to the fact that in this flow regime a fewer number of bubbles is injected, determines that only a small percentage of the turbulence energy of the mean flow is used to deflect the bubbles and eventually convect them. On the other hand, the higher buoyancy of the bubbles tends to reduce the time in which they interact with the boundary layer. The last remark is supported in a larger context by N. K. Madavan's experiments [8] in which two gravitational orientations of the boundary layer were studied. It was observed that when the buoyancy field acts against the escape of the bubbles from the boundary layer the bubbles become more effective in reducing the skin friction, vide Figures 1.5 and 1.6.

The above ideas explain why an increase in the injection flow rate will, in general, lead to a further decrease in the skin friction. The higher inertia of the bubbles allows them to reach larger eddies farther out in the boundary layer, while their smaller diameter and larger number makes them more effective vehicles of momentum transfer.

The fact that for a given injection flow rate lower skin friction reductions are observed for higher free stream velocities, vide Figure 1.1, can also be explained by the above reasoning. At higher free stream velocities, the bubbles are swept away sooner by the mean flow forcing the momentum interchanges with the mean flow to occur through smaller eddies closer to the plate. One

should keep in mind that the above reasoning assumes a zero pressure gradient. Obviously the presence of a pressure gradient affects the dynamic behavior of the bubbles in the boundary layer. Consequently, the skin friction reduction has different characteristics from the flat plate case.

The second experimental fact mentioned above, however, seems to contradict the preceeding exposition. The answer to the apparent contradiction lies in the structure of the turbulent boundary layer [24]. The turbulent energy is supplied to the boundary layer from the free stream through large scale structures, which through vortex stretching convey the turbulent energy to the inner regions of the boundary layer.

With this rough picture in mind, we conclude that for a given free stream flow regime the maximum skin friction reduction is obtained for the injection volumetric flow rate for which the bubbles have enough inertia to reach and interact with the larger scale structures. In this way the bubbles provide a breakdown of the chain of turbulent energy transmission to the inner region of the turbulent boundary layer. The fact that the skin friction starts increasing after the injection flow rate has surpassed its optimum value is clear because in these circumstances an increasing number of bubbles has sufficient energy to bypass the large scale structures without interchanging momentum with the turbulent structure of the boundary layer. Finally, the localized nature of the phenomenon is also explained by the fact that once bubbles

are brought to the same velocity as the mean flow, they possess no more energy to interchange with the flow and thus lose their ability to affect the flow's turbulent structure.

From this picture one perceives four main contributors to the drag reduction in a boundary layer with microbubbles:

- A decrease of the mean density of the "fluid",
- An increase of the mean viscosity of the "fluid",
- The interchange of linear and angular momentum between the bubbles and the turbulence structure of the mean flow, and
- The added mass, or fluid entrainment, of the bubbles when they are injected.

At the stage of current research on this problem, it is difficult to identify the main contributors, however, the previous reasoning suggests that the last two physical phenomena are probably the most important.

4.4 The System of Equations

The equations to be integrated for laminar flow are, of course, the steady-state compressible Navier-Stokes equations [25], along with a transport equation for the second phase,

$$\nabla \cdot (\rho \vec{V}) = 0, \quad (4.4.1a)$$

$$\rho [\vec{V} \cdot \nabla \vec{V}] = \rho \vec{B} - \nabla p - \mu \nabla x (\nabla x \vec{V}) - \nabla \mu x (\nabla x \vec{V}), \quad (4.4.1b)$$

$$\vec{V} \cdot \nabla X = 0, \quad (4.4.1c)$$

as well as their turbulent counterparts.

In the system above, μ is the viscosity of the mixture which is related to Eq. (4.2.2) by

$$\mu = \mu_l (1 + \mu_{sp}) \quad (4.4.2)$$

The transport equation (4.4.1c) stems from the assumption that the bubbles are convected by the main flow. Even though this is not true at the locus of injection, we expect this equation to capture some of the kinematics associated with the fact that the bubbles at injection possess some velocity of their own. Besides this, the adoption of Eq. (4.4.1c) introduces in the system the ability to compute the void fraction profile, as opposed to its a priori specification as is done in [18]. Equation (4.4.1c) can be understood as a remanent from the consideration of a full two phase flow system. Clearly the local density in the system (4.4.1) is given by

$$\rho = \rho_l (1 - X) + \rho_g X \quad (4.4.3)$$

For a two-dimensional flow, the system (4.4.1) reduces to

$$\frac{\partial u}{\partial x} + \frac{\partial v}{\partial y} = 0 \quad , \quad (4.4.4a)$$

$$u \frac{\partial X}{\partial x} + v \frac{\partial X}{\partial y} = 0 \quad , \quad (4.4.4b)$$

$$\rho \left[u \frac{\partial u}{\partial x} + v \frac{\partial u}{\partial y} \right] = B_x - \frac{\partial p}{\partial x} + \mu \nabla^2 u + \frac{\partial \mu}{\partial y} \left(\frac{\partial u}{\partial y} - \frac{\partial v}{\partial x} \right) \quad , \quad (4.4.4c)$$

$$\rho \left[u \frac{\partial v}{\partial x} + v \frac{\partial v}{\partial y} \right] = B_y - \frac{\partial p}{\partial y} + \mu \nabla^2 v - \frac{\partial \mu}{\partial x} \left(\frac{\partial u}{\partial y} - \frac{\partial v}{\partial x} \right) \quad , \quad (4.4.4d)$$

where to obtain Eq. (4.4.4a), we used Eq. (4.4.4b) and Eq. (4.4.3).

Since we know very little about the momentum interchanges between the bubbles and the carrier phase, we will discard the body force field terms. In this continuum approach, however, we still can take into account the buoyancy force field of the bubbles. Neglecting the other dynamic interactions may not be a very good approximation since the experimental results summarized in Chapter I showed the biggest skin friction reduction close to the region where the bubbles are injected, a fact that may be associated with momentum interchanges between the bubbles and the mean flow. Dynamic interactions between the bubbles, which are probably important in this region due to the high packing and velocity difference between the two phases, had also to be disregarded.

By virtue of the fact that

$$\rho_g / \rho_l \ll 1, \quad (4.4.5)$$

the system (4.4.3) can be further reduced to

$$\frac{\partial u}{\partial x} + \frac{\partial v}{\partial y} = 0, \quad (4.4.6a)$$

$$u \frac{\partial X}{\partial x} + v \frac{\partial X}{\partial y} = 0, \quad (4.4.6b)$$

$$(1 - X) \left[u \frac{\partial u}{\partial x} + v \frac{\partial u}{\partial y} \right] = - \frac{1}{\rho_l} \frac{\partial p}{\partial x} + \frac{u}{\rho_l} \nabla^2 u + \frac{1}{\rho_l} \frac{\partial u}{\partial y} \left(\frac{\partial u}{\partial y} - \frac{\partial v}{\partial x} \right), \quad (4.4.6c)$$

$$(1 - X) \left[u \frac{\partial v}{\partial x} + v \frac{\partial v}{\partial y} \right] = \frac{B_v}{\rho_l} - \frac{1}{\rho_l} \frac{\partial p}{\partial y} + \frac{v}{\rho_l} \nabla^2 v - \frac{1}{\rho_l} \frac{\partial u}{\partial x} \left(\frac{\partial u}{\partial y} - \frac{\partial v}{\partial x} \right). \quad (4.4.6d)$$

For this problem, the laminar flow regime develops in the absence of bubbles and thus the system of equations (4.4.6) reduces to the ubiquitous laminar boundary layer equations. The Prandtl hypothesis holds and after appropriate nondimensionalization the equations read

$$\frac{\partial u'}{\partial x} + \frac{\partial v'}{\partial y} = 0, \quad (4.4.7a)$$

$$u' \frac{\partial u'}{\partial x} + v' \frac{\partial u'}{\partial y} = \frac{\partial^2 u'}{\partial y'^2}, \quad (4.4.7b)$$

where the streamwise pressure gradient has been omitted because we are studying the flow on a flat plate with zero pressure gradient. The primed variables, of course, correspond to the appropriately scaled boundary layer variables, defined by $y' = \sqrt{\text{Re}_L} y$; $v' = \sqrt{\text{Re}_L} v$, where the Reynolds number is based on the physical properties of the carrier fluid, i.e., $\text{Re}_L = \frac{\rho_\ell U_\infty L}{\mu_\ell}$ and L is some length scale.

4.5 The Turbulent Regime

As is the case in all boundary layer flow calculations, transition is a crucial step of the computations. Its prediction, when not known experimentally, is very difficult.

Transition depends mainly on the free stream turbulence and on the pressure gradient. Since we are doing computations on a flat plate flow, which is usually the first-case problem in fluid mechanics, the mechanisms and position of the onset of boundary

layer transition are fairly well understood [26]. Nevertheless, to compute transition itself is a completely different matter and one has to resort to empirical methods, even in the flat plate problem. In our calculations, we make use of Michel's method as reported by Cebeci, et al. [27]. Michel's transition curve can be expressed as a function of the leading edge Reynolds number as

$$Re_{tr} = 1.174[1 + (22,400/Re_x)]Re_x^{0.46}, \quad (4.5.1)$$

for $0.1 \times 10^6 < Re_x < 40 \times 10^6$ which is the usual transition Reynolds number range for a flat plate in normal conditions.

Having said this, we turn to the study of the system of flow equations of motion (4.4.6) for turbulent flow. We consider in this system the velocity and pressure fields to consist of a mean with a superposed disturbance, i.e.,

$$\begin{aligned} u &= U + \tilde{u}, \\ v &= V + \tilde{v}, \\ p &= P + \tilde{p}. \end{aligned} \quad (4.5.2)$$

Upon substitution on the system (4.4.6) and after the usual averaging and subtraction of the equations satisfied by the disturbances, we find the appropriate Reynolds equations to be given by

$$\frac{\partial U}{\partial x} + \frac{\partial V}{\partial y} = 0, \quad (4.5.3a)$$

$$U \frac{\partial X}{\partial x} + V \frac{\partial X}{\partial y} = 0, \quad (4.5.3b)$$

$$\begin{aligned}
 (1 - X) \left[U \frac{\partial U}{\partial x} + V \frac{\partial U}{\partial y} \right] &= - \frac{1}{\rho_L} \frac{\partial P}{\partial x} + \frac{\mu}{\rho_L} \nabla^2 U + \frac{1}{\rho_L} \frac{\partial u}{\partial y} \left(\frac{\partial U}{\partial y} - \frac{\partial V}{\partial x} \right) \\
 &- (1 - X) \left[\frac{\partial}{\partial x} (\overline{u^2}) + \frac{\partial}{\partial y} (\overline{uv}) \right] , \quad (4.5.3c)
 \end{aligned}$$

$$\begin{aligned}
 (1 - X) \left[U \frac{\partial V}{\partial x} + V \frac{\partial V}{\partial y} \right] &= - \frac{1}{\rho_L} \frac{\partial P}{\partial y} + \frac{\mu}{\rho_L} \nabla^2 V - \frac{1}{\rho_L} \frac{\partial u}{\partial x} \left(\frac{\partial U}{\partial y} - \frac{\partial V}{\partial x} \right) \\
 &- (1 - X) \left[\frac{\partial}{\partial x} (\overline{uv}) + \frac{\partial}{\partial y} (\overline{v^2}) \right] . \quad (4.5.3d)
 \end{aligned}$$

The attentive reader will have noticed that in order to obtain the equations above, disturbances of the void fraction distribution were not considered. This avoids one of the major difficulties in this study, i.e., the simulation of the interaction of buoyancy with the turbulent shear stress.

If one now performs an order of magnitude analysis of the above equations for a thin shear layer, i.e., in the limit of high Reynolds number one finds that the y-momentum equation reduces to

$$\frac{1}{\rho_L} \frac{\partial P}{\partial y} = gX - (1 - X) \frac{\partial}{\partial y} (\overline{v^2}) , \quad (4.5.4)$$

since from Archimedes principle, $B_y = \rho_L gX$.

After integration and recognizing the vanishing boundary conditions of both the y-velocity fluctuation and the void fraction, we find

$$\frac{1}{\rho_l} [P_\infty - P] = (1 - X) \overline{\tilde{v}^2} - \int_y^\infty \overline{\tilde{v}^2} \frac{\partial X}{\partial y} dy + g \int_y^\infty X dy \quad (4.5.5)$$

If we differentiate this equation with respect to x and use the fluctuating counterpart of Eq. (4.5.3b), we find that

$$\begin{aligned} -\frac{1}{\rho_l} \frac{\partial P}{\partial x} &= (1 - X) \frac{\partial \overline{\tilde{v}^2}}{\partial x} - \overline{\tilde{v}^2} \frac{\partial X}{\partial x} + \frac{\partial}{\partial x} \int_y^\infty \overline{uv} \frac{\partial X}{\partial x} dy \\ &+ g \frac{\partial}{\partial x} \int_y^\infty X dy, \end{aligned} \quad (4.5.6)$$

since $P_\infty = \text{constant}$ for a flat plate.

It is important to note that the last term of the equation above captures, at least in part, the localized nature of the drag reduction. It is clear that the buoyancy force field will introduce a source term in the streamwise momentum equation. Furthermore, the importance of this source term is confined to the region of the flow where the bubbles are deflected by the freestream flow.

Substitution of (4.5.6) into (4.5.3c) eliminates the pressure term and gives for the x momentum equation,

$$\begin{aligned} (1 - X) \left[U \frac{\partial U}{\partial x} + v \frac{\partial U}{\partial y} \right] &= (1 - X) \frac{\partial}{\partial x} (\overline{\tilde{v}^2} - \overline{u^2}) - (1 - X) \frac{\partial}{\partial y} (\overline{uv}) \\ &- \overline{\tilde{v}^2} \frac{\partial X}{\partial x} + \frac{\partial}{\partial x} \int_y^\infty \overline{uv} \frac{\partial X}{\partial x} dy + \frac{\mu}{\rho_l} \nabla^2 U + \frac{1}{\rho_l} \frac{\partial \mu}{\partial y} \left(\frac{\partial U}{\partial y} - \frac{\partial V}{\partial x} \right) \\ &+ g \frac{\partial}{\partial x} \int_y^\infty X dy \quad (4.5.7) \end{aligned}$$

If we estimate the order of magnitude of the various terms in Eq. (4.5.7), we find that in the thin shear layer, high Reynolds number limit the x-momentum equation reduces to

$$(1 - X) \left[U \frac{\partial U}{\partial x} + v \frac{\partial U}{\partial y} \right] = - (1 - X) \frac{\partial}{\partial y} (\overline{uv}) + \frac{\mu}{\rho_\ell} \frac{\partial^2 U}{\partial y^2} + \frac{1}{\rho_\ell} \frac{\partial \mu}{\partial y} \frac{\partial U}{\partial y} + g \frac{\partial}{\partial x} \int_y^\infty X dy \quad (4.5.8)$$

In order to model the turbulent shear stress, we use the usual Boussinesq type approximation, i.e.,

$$(\overline{uv}) = - \epsilon \frac{\partial U}{\partial y} \quad , \quad (4.5.9)$$

where ϵ is the eddy viscosity.

In the inner region of the boundary layer, the eddy viscosity is modeled by Prandtl's mixing length hypothesis

$$\epsilon_i = \ell^2 \left| \frac{\partial U}{\partial y} \right| \quad , \quad (4.5.10)$$

where ℓ , Prandtl's mixing length, is computed from a modified Van Driest expression

$$\ell = k y^+ \{1 - e^{-y^+/A}\} \quad , \quad (4.5.11)$$

with von Kármán's constant $k = 0.41$.

In this expression, following Launder, et al. [28], we use

$$A = (\tau/\tau_w)^{3/2} / 26 (1 + 5.9 v_w^*) \quad , \quad (4.5.12)$$

an expression that has displayed a better behavior for flows with boundary layer injection. Through a convenient formulation of the function h we attempt to capture the local nature of the skin friction reduction.

As pointed out in Section 4.3, the phenomenon of microbubble boundary layer drag reduction can be consistently explained if one thinks of it in terms of momentum interchanges between the bubbles and the turbulent structure of the mean flow as well as bubble flow entrainment.

Under the limitations of the description of the flow adopted here, we are led to the conclusion that the mixing-length correction function h should depend on the streamwise gradient of $\partial v / \partial y$ as well as on some nondimensional parameter representative of the average bubble radius, such as T_a , i.e.,

$$h = \frac{1 + \mu_{sp}}{1 - X} g\left(\frac{\partial^2 v}{\partial x \partial y}, T_a\right) \quad (4.5.13)$$

where the dependency on the void fraction results from the non-dimensionalization of the eddy viscosity with the local properties of the "fluid".

The form of the functional dependence of h on the cross-stream velocity gradient, suggested above, is supported by the mathematical formulation of the buoyancy effects.

It is clear if the present direction is adopted then the form of h requires further intensive study, the first hurdle of which must be the acquisition of a more comprehensive set of experimental data on the properties of the mean flow at injection. For this reason, we are forced to disregard g , even though the previous reasoning suggests that g affords the most practical way of capturing the localized nature of the drag reduction.

In the outer or wake region of the boundary layer, the eddy viscosity model that we adopt is due to Clauser [29],

$$\varepsilon_0 = \alpha U_\infty \delta^* , \quad (4.5.14)$$

where $\alpha = 0.0168$ and δ^* is the boundary layer displacement thickness.

With expression (4.5.9) the momentum equation (4.5.8) becomes

$$\begin{aligned} (1 - X) \left[U \frac{\partial U}{\partial x} + v \frac{\partial U}{\partial y} \right] &= (1 - X) \frac{\partial}{\partial y} \left(\varepsilon \frac{\partial U}{\partial y} \right) + g \frac{\partial}{\partial x} \int_y^\infty X dy \\ &+ \frac{\mu_\ell}{\rho_\ell} \frac{\partial}{\partial y} \left[(1 + \mu_{sp}) \frac{\partial U}{\partial y} \right] , \end{aligned} \quad (4.5.15)$$

which along with Eq. (4.5.3a) and Eq. (4.5.3b) constitutes the system to be integrated.

The numerical scheme used to integrate the equations above is Keller's Box Method [27]. The transformation of the above equations by the Mangler-Levy-Lees equations is given in Appendix D. The boundary layer code based on the transformed equations is given in Appendix E.

4.6 The Boundary Conditions

We know from N. K. Madavan's experiments [8] that in the region of bubble injection the flow is completely turbulent. From the boundary layer measurements in the test section they estimate the position of a virtual flat plate leading edge that would have generated the boundary layer profile observed. It is based on the location of this virtual flat plate leading edge that we decide the location of bubble injection in the code.

Since we are simulating the bubbles by a variable density and viscosity "fluid", we must establish the boundary conditions not only for the velocity field but also for the void fraction. So, if $x > 0$ is the streamwise independent variable, we set

$$X(x,0) = CX_{[a,b]} \quad , \quad (4.6.1a)$$

where $[a,b]$ is the interval of injection. The estimation of the constant C is based on N. K. Madavan's experiments. The laminar regime boundary condition for the void fraction is given by

$$X(0,y) = 0 \quad , \quad (4.6.1b)$$

since the bubbles are injected in the turbulent flow regime.

The velocity field boundary conditions at the plate are determined by a statement of conservation of mass. At the impervious part of the wall we have

$$V_w = U_w = 0 \quad . \quad (4.6.2a)$$

In the interval of injection, we impose

$$U_w = 0 \quad , \quad (4.6.2b)$$

$$\rho_g Q_g = V_w (b - a) [\rho_\ell (1 - X) + \rho_g X] \quad ,$$

or

$$V_w = \frac{\rho_g Q_g}{\rho_\ell (b - a)(1 - X)} \quad , \quad (4.6.2c)$$

where Q_g is the volumetric flowrate of the gas being injected.

4.7 Results

In order to convince the reader that the code presented in Appendix E is reliable, we computed several characteristic parameters of the boundary layer in the absence of injection.

An inspection of Figures 4.2, 4.3, 4.4 and 4.5 shows that in the absence of injection the code generates results that are in agreement with widely known experimental data and empirical relationships for the flat plate boundary layer [26,30].

Despite this, the code is not in a stage where it can predict void fraction profiles with high wall resolution. For a 20 to 30 grid point boundary layer resolution, the code predicts void fraction profiles that have a maximum at $y/\delta = 0.1$. This fact is very encouraging since this is exactly the position on the buoyancy layer where experiments seem to suggest the highest bubble concentration.

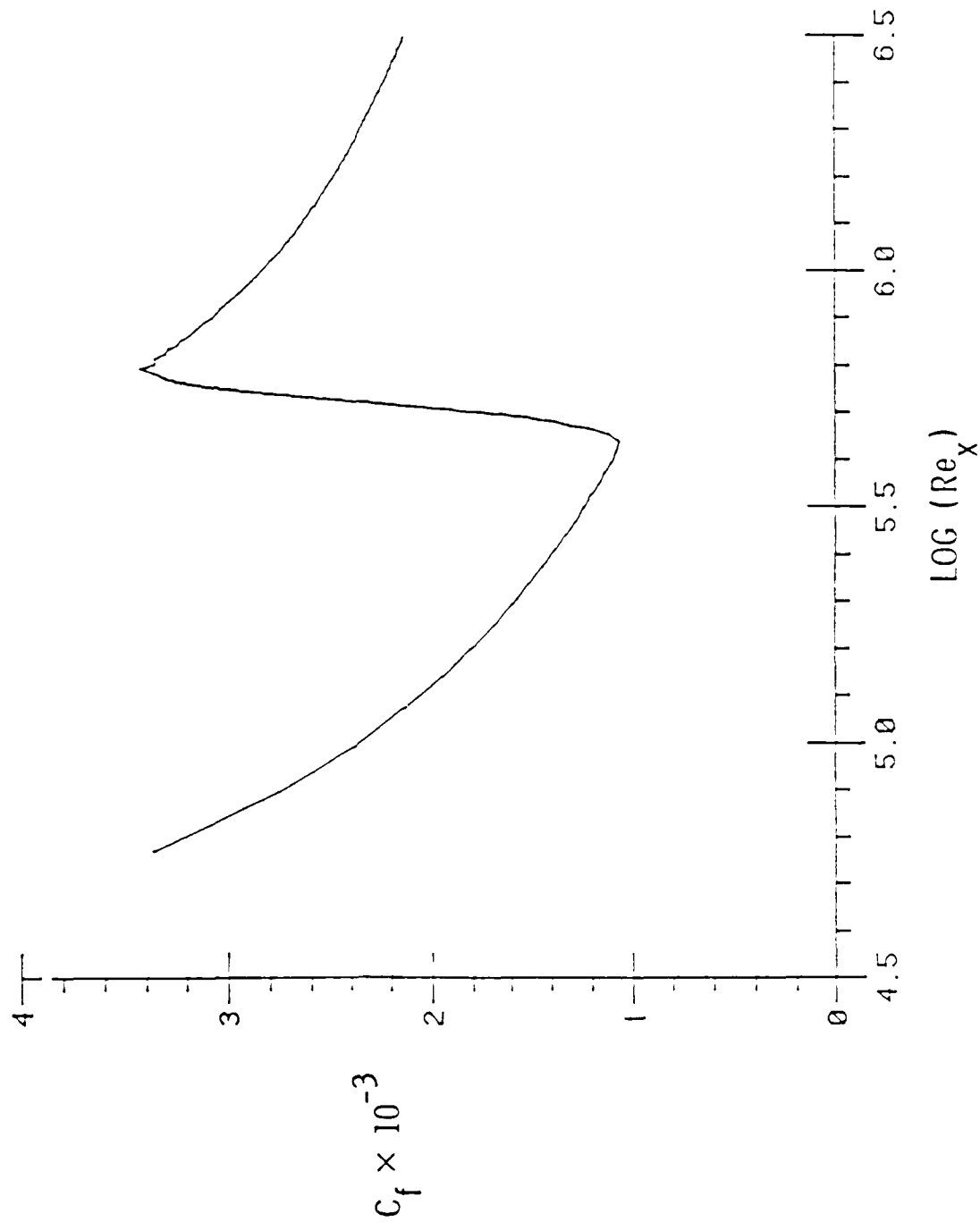


Figure 4.2. Variation of the Skin Friction with the Streamwise Reynolds Number in the Absence of Injection ($U_\infty = 4.2 \text{ m/s}$).

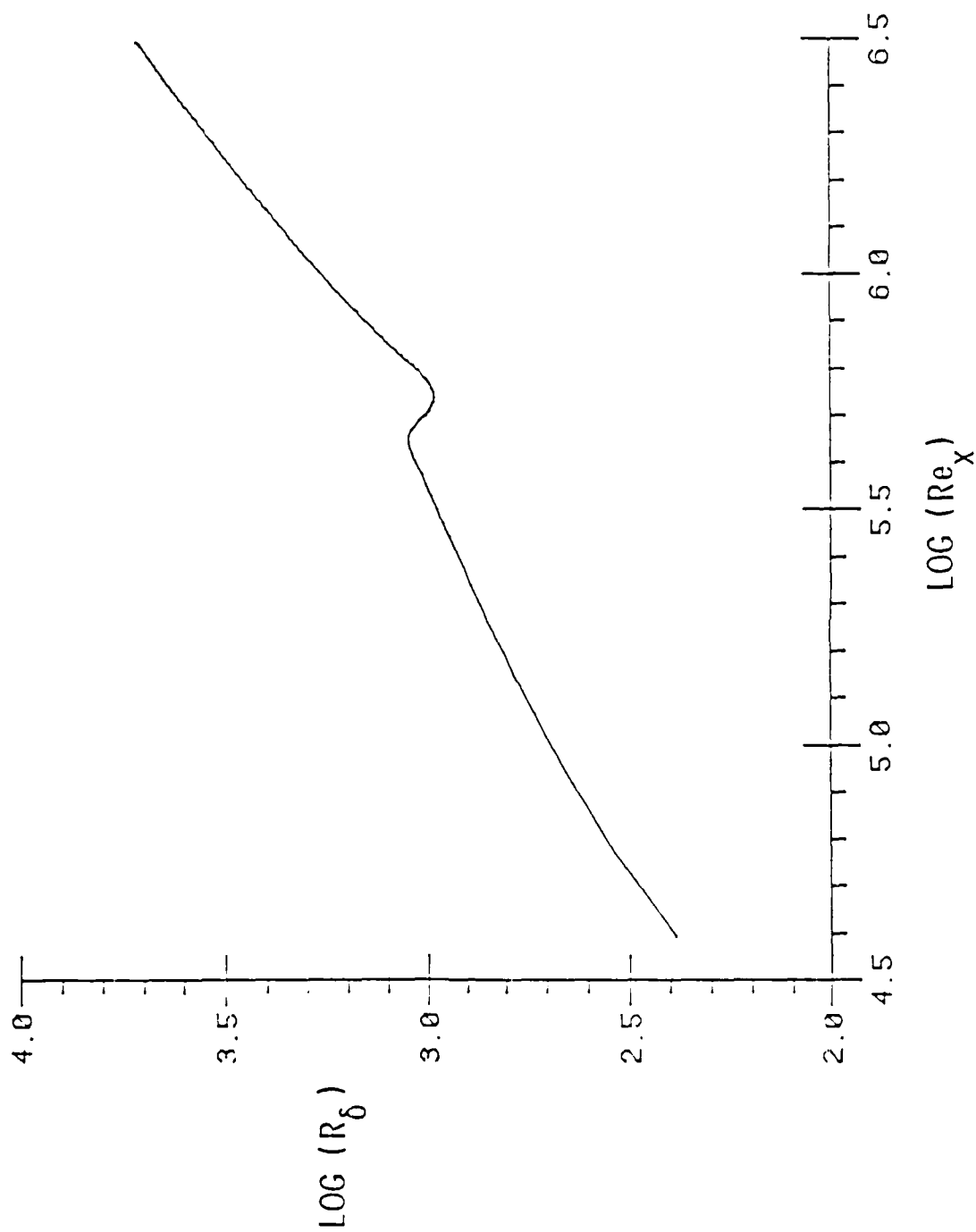


Figure 4.3. Variation of the Boundary Layer Displacement Thickness Reynolds Number with the Streamwise Reynolds Number in the Absence of Injection ($U_\infty = 4.2$ m/s).

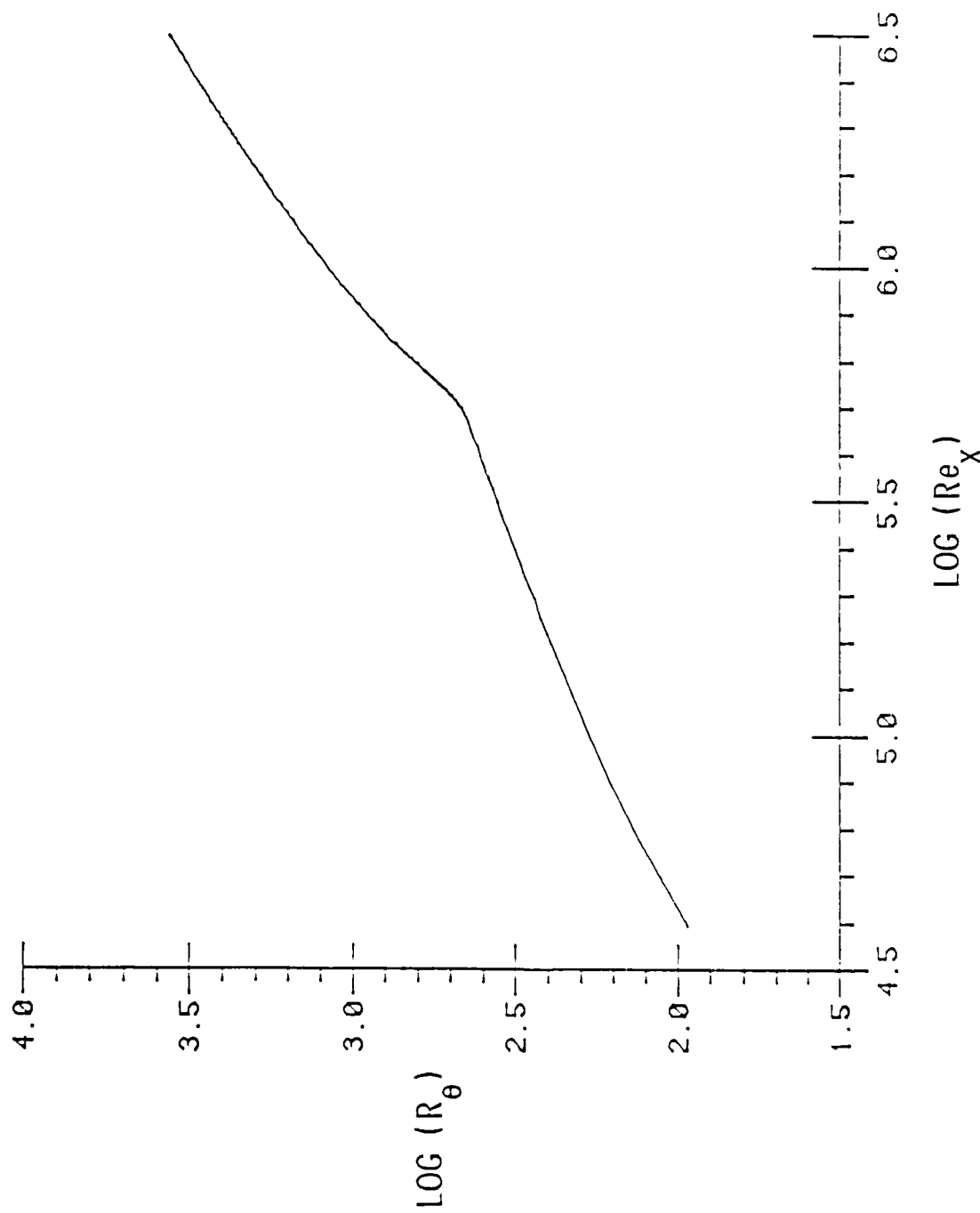


Figure 4.4. Variation of the Boundary Layer Momentum Thickness Reynolds Number with the Streamwise Reynolds Number in the Absence of Injection ($U_\infty = 4.2$ m/s).

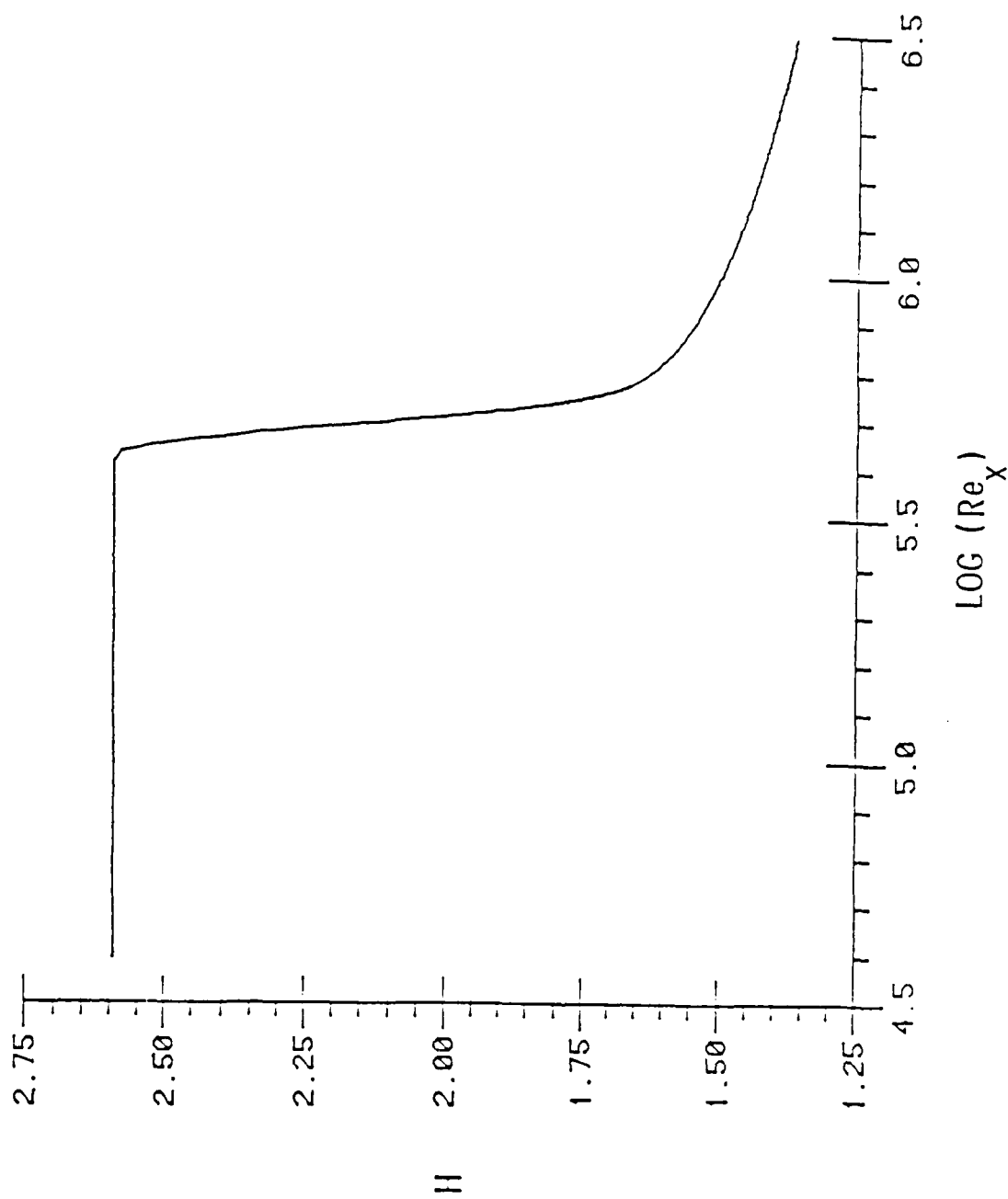


Figure 4.5. Variation of the Boundary Layer Shape Factor with the Streamwise Reynolds Number in the Absence of Injection ($U_{\infty} = 4.2$ m/s).

These results are however not satisfactory because of the lack of resolution of the wall gradients. The fact that the bubble injection occurs in the turbulent regime demands the resolution of the wall gradients. This can be done rather easily in the code since the positions of the first grid point and the boundary layer edge can be chosen freely, but judiciously.

With this resolution, the coupling of the momentum and transport equations becomes very delicate because of the high streamwise near wall void fraction gradients. Several unsuccessful attempts were made to correct this situation. A refinement of the streamwise grid at injection as well as a smoother injection void fraction profile were unable to correct the problem.

The resolution of the wall gradients is essential because the form of the transformed momentum equation suggests that the buoyancy effects are important only in the inner region of the boundary layer where the turbulent shear stresses are either negligible or of the same order of magnitude as the viscous stresses.

It was observed that for a rather modest wall void fraction, the code before the computations collapsed, predicts a skin friction reduction of the order of 60%. This fact is not only encouraging but also points to the possible solution of the problems that the model has presented.

From the beginning we assumed that the boundary layer hypotheses were valid throughout the boundary layer with micro-bubbles. The large streamwise velocity gradients at injection suggests that the boundary layer hypotheses are not valid close to the locus of injection.

These conclusions indicate that the order of magnitude analysis of the momentum equations should be reviewed.

The code as it is now should be able to handle the computations of the flowfield away from the locus of injection, however, a different version of the momentum equations, as indicated above, should be solved during injection.

This will certainly add to the complexity of the computations because the momentum equations at injection will probably not be parabolic anymore but elliptic.

CHAPTER V

DISCUSSION AND CONCLUSIONS

5.1 The Stability

As was discussed in Chapters II and III, the simple arrangement of hollow vortices is unconditionally unstable. It was shown, through an analysis similar to von Kármán's, that the instability is independent from either the size of the cylinders, as reflected by the dipole strength, or the circulation of the vortices.

The evolution of a point hollow vortex sheet was included for comparison purposes. Even though the time history that we obtained for this case is different from that presented by Chow [11], the onset of the rollup is found to have the same pattern. Indeed, from the evolution of the hollow vortex sheet, one concludes that the consideration of the dipole system is a destabilizing factor since the onset of the rollup comes earlier than for the corresponding point vortex sheet.

From the point of view of inviscid flows, the apparent stability of the hollow vortex sheet is associated with its proximity to the wall. Indeed, as is clear from Figure 2.3, the stability domain shrinks exponentially away from the wall and, as expected, the condition of unconditional instability is recovered several disturbance wavelengths away from the wall.

The results of the small disturbance analysis of the symmetric hollow vortex sheet presented in Chapter II could not be corroborated by the computation of its evolution because the CPU time required renders the attempt impractical.

For the sake of completeness, the evolution of a sinusoidal wave of point vortices in the presence of a wall was also computed. Supporting von Kármán's work, the arrangement is always unstable. Indeed, the pattern of evolution, vide Figure 3.3, is suggestive of the large scale turbulence structures that develop in a turbulent boundary layer after the breakdown of the Tollmien-Schlichting waves.

It's conceivable, and our analysis does not address the issue, that viscous effects also play a role on the stability of the bubbles, which we simulated by cylinders due to the two-dimensional nature of the boundary layer. A deeper study of this aspect of the the problem is necessary.

Attempts to correlate, in a very simple minded way [31], the circulation of the hollow vortices to a velocity gradient representative of their position on the boundary layer lead to meaningless conclusions. However, the fact that the bubbles are conveyed by the mean flow, even though not all at the same speed, renders the analytic treatment of the problem of shear flow through an array of spheres conceivable.

The problem of low Reynolds number flow through periodic arrays of spheres and cylinders in several packing configurations, has been studied by other authors. H. Hasimoto [32] studied the problem of flow past special cases of cubic lattices. More recently [33,34], his work has been expanded, in an equally elegant way, to encompass a wider range of void fractions. The latter authors derive an asymptotic solution for the high void fraction flow regime. They provide the connection between their

solution and Hasimoto's, for the intermediate void fractions, through the numerical integration of the resulting equations using spectral methods.

The extension of this analysis to our problem must resolve the difficulty introduced by the motion of the spheres convected by the shear flow, i.e., the unsteadiness. The unsteadiness translates itself into a time dependency of the solution domain. This is where the mathematical difficulties arise.

5.2 Drag Reduction

If not from the title of this dissertation certainly from Chapter IV, the reader must have realized the monumental task that it will be to describe this flow even from an engineering point of view.

Ahead we try to point out further some more of the difficulties and suggest, in broad lines, some research that can lead to a better understanding of the problem.

The fact that the bubbles are very small is very suggestive of a phenomenological approach to this problem. On the other hand, the high packing of the bubbles may support arguments in the opposite direction. Whichever direction one chooses, the challenge is enormous.

If one decides to formulate appropriate constitutive relations for a bubbly flow [22], then the present experimental techniques must be improved to allow the measurement of mean flow properties in regions of high void fraction. To the author's knowledge, very

little effort has been conducted in this direction, at least in connection with this problem. Nevertheless, exciting progress seems to have been achieved recently by R. van der Welle [35]. He reports the development of ingenious measurement techniques for bubbly flows with high void fraction that can conceivably be extended to the study of the present flow.

It is important to notice that any such constitutive relation will be dependent not only on local properties of the fluid but also on local properties of the flow [36,37,38]. The latter effect is dictated by the dynamic interaction between the bubbles and the carrier flow.

Another very important aspect of an experimental investigation must be the study of the interaction of the turbulent structure and the carrier flow with the dynamics of bubbles. This complex phenomenon seems to be very important at least in the region of injection of the bubbles. Indeed, the Soviet researchers [2,4] postulate that this is the most important mechanism of the drag reduction. If this is indeed the whole picture, it is not clear. The idea is supported however, by the fact that the drag reduction persists only for a few boundary layer thicknesses downstream from the place of injection. The way in which this may be happening was presented in Section 4.3.

One is faced with a major computational and modeling effort, specially in providing appropriate closure models for the resulting turbulent flow equations. Attention must be dedicated not only to the modeling of the buoyancy effects [19,39] but also to the shear stresses themselves. It is not clear, for example, that the

normal stresses in the streamwise and cross-stream directions are of the same order of magnitude as is usually assumed, and is experimentally confirmed in the flat plate turbulent boundary layer. Another aspect is that, since buoyancy and the void fraction play such an important role on this flow, it is probably more appropriate in the averaging of the Reynolds number to use a mass weighed ensemble average [39].

Also, a mixing length approach in the modeling of the shear stresses may prove inadequate. The empirical relations used in this approach depend on particular characteristics of the boundary layer which have not yet been confirmed true for the boundary layer with microbubbles. This suggests interesting experimental research that could make use of the techniques mentioned in [35]. The strong interaction of the bubbles with the turbulence structure may preclude any such approach and force the use of second order closure models [39]. It is not clear, for example, that the intermittency characteristics exhibited by boundary layers with and without bubbles is the same. Indeed, the reasoning presented before on the mechanisms of the drag reduction suggests that this is not the case. If experiments ever substantiate this, then an appropriate formulation for the eddy viscosity in the outer region of the boundary layer is necessary.

Either in the approach adopted here or in a complete two phase flow description, the researcher must be concerned about the appropriate formulation of the boundary conditions. The carrier flow boundary conditions are straightforward, however,

it is clear that the wall boundary condition for the void fraction is itself a function of the injection flow rate. Consequently, even though the approach adopted here is physically meaningful, it is rather restricted and must be improved. Once again, measurement techniques must be perfected in order to allow near wall void fraction measurements and determine its correlation with the injection flowrate.

For the sake of completeness and adding to the complexities already mentioned, the author must point out that recent results from ongoing research in this problem [40] suggests that the bubbles are bigger than originally thought and the coalescence is a fact specially downstream from injection.

It is clear from what we presented as well as past work [2-8] that, at least in the near future, the main effort towards understanding this problem must be carried out experimentally. At the current research stage there are too many gaps in relevant experimental data. A more complete knowledge of these is needed if the researcher is to approach the modeling of this flow with a reasonable degree of confidence.

BIBLIOGRAPHY

1. M. E. McCormick and R. Battacharyya, "Drag Reduction of a Submersible Hull by Electrolysis," Naval Engineers Journal 85:11-16 (1973).
2. G. S. Migirenko and A. R. Evseev, "Turbulent Boundary Layer with Gas Saturation," Problems in Thermophysics and Physical Hydrodynamics (in Russian) (Novosibirsk, Nauka, 1974).
3. Y. N. Dubnishchev, A. R. Evseev, V. S. Sobolev and E. N. Utkin, "Study of Gas Saturated Turbulent Streams using a Laser Doppler Velocity Meter," J. Appl. Mech. Tech. Phys. 16(1):114 (1975). Translated from Zhur. Prikl. Mekh. Tekh. Fiz. 1:147 (1975).
4. V. G. Bogdevich and A. R. Evseev, "Effect of Gas Saturation on Wall Turbulence," Investigations of Boundary Layer Control (in Russian), edited by S. S. Katateladze and G. S. Migirenko (Thermophysics Institute Publishing House), p. 49 (1976).
5. V. G. Bogdevich and A. G. Malyaga, "The Distribution of the Skin Friction in a Turbulent Boundary Layer in Water beyond the Location of Gas Injection," Investigations of Boundary Layer Control (in Russian), edited by S. S. Katateladze and G. S. Migirenko (Thermophysics Institute Publishing House), p. 62 (1976).

BIBLIOGRAPHY [continuation]

6. N. K. Madavan, S. Deutsch and C. L. Merkle, "Measurements of Local Skin Friction in a Microbubble Modified Turbulent Boundary Layer," J. Fluid Mech. 156:237-256 (1985).
7. N. K. Madavan, S. Deutsch and C. L. Merkle, "The Effects of Porous Materials on Microbubble Skin Friction Reduction," AIAA Paper 84-0345 (1984).
8. N. K. Madavan, S. Deutsch and C. L. Merkle, "Reduction of Turbulent Skin Friction by Microbubbles," Physics of Fluids 27(2):356 (February 1984).
9. E. Silberman, Proceedings of the Fifth Midwestern Conference on Mechanics, The University of Michigan, Ann Arbor, MI, p. 263 (1957).
10. R. F. Hama and E. R. Burke, "On the Rolling Up of a Vortex Sheet," I. M. of The Institute for Fluid Dynamics and Applied Mathematics, The University of Maryland.
11. C. Y. Chow, An Introduction to Computation Fluid Mechanics, John Wiley & Sons, New York, pp. 322-329 (1979).
12. L. Rosenhead, "The Formation of Vortices from a Surface Discontinuity," Proceedings of the Royal Society, Series A, Vol. 132, pp. 170-192 (1931).
13. Sir H. Lamb, Hydrodynamics, Sixth Edition, Chapter VII, Dover Publishers (1932).

BIBLIOGRAPHY [continuation]

14. Albert D. Wheelon, "A Short Table of Summable Series,"
Douglas Aircraft Company, SM-14642 (1953).
15. G. R. Baker, "Studies in Vortex Motion," Ph.D. Thesis,
The California Institute of Technology, Pasadena, CA
(1977).
16. K. Karamcheti, Principles of Ideal Fluid Aerodynamics,
pp. 239 and 253, Krieger Publishing Co. (1980).
17. Milne and L. M. Thomson, Theoretical Hydrodynamics,
Macmillan Company, New York, 2nd Edition (1957).
18. N. K. Madavan, S. Deutsch and C. L. Merkle, "Numerical
Investigations into the Mechanisms of Microbubble Drag
Reduction," Proceedings of the 1984 Symposium on Laminar
Turbulent Boundary Layers, ASME Fluids Engineering
Conference, New Orleans, LA (1984).
19. M. Ishii, Thermo Fluid Dynamic Theory of Two Phase Flow,
Eyrolles, Paris, France (1975).
20. A. Einstein, "Eine Neue Bestimmung der Moleculdimensionen"
(in German), Annaln der Physik 19:298 (1906).
21. J. Happel and H. Brenner, Low Reynolds Number Hydrodynamics,
Nijhoff Publishers, The Netherlands (1983).
22. S. Hinata and M. Okhi, "The Relationship between the
Apparent Viscosity and the Void Fraction in Two-Phase
Flow," Bull. of JSME 14(75) (1971).

AD-A191 975

STABILITY AND DRAG REDUCTION IN A BOUNDARY LAYER WITH
MICROBUBBLES(U) PENNSYLVANIA STATE UNIV UNIVERSITY PARK
APPLIED RESEARCH LAB J M NEVES FEB 88

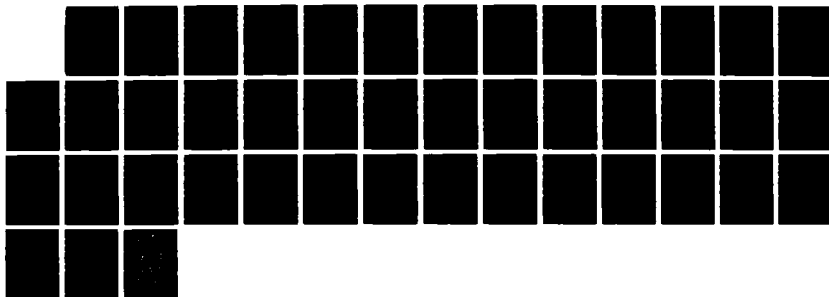
2/2

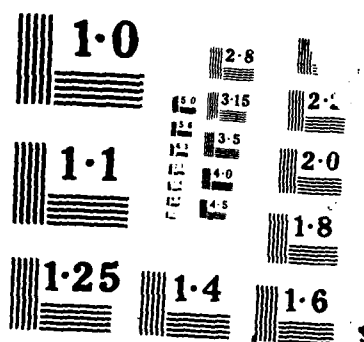
UNCLASSIFIED

ARL/PSU-TR-88-001 N00024-85-C-6041

F/G 20/4

NL





BIBLIOGRAPHY [continuation]

23. G. I. Taylor, "The Formation of Emulations in Refinable Fields of Flow," Proceedings of the Royal Society, Series A, Vol. 146, p. 501 (1934).
24. H. Tennekes and J. L. Lumley, A First Course in Turbulence, MIT Press (1983).
25. H. W. Liepman and A. Roshko, Elements of Gasdynamics, John Wiley & Sons, New York (1957).
26. F. M. White, Viscous Flow, McGraw Hill Book Co., New York (1974).
27. T. Cebeci and A. M. O. Smith, Analysis of Turbulent Boundary Layers, Chapter 9, Academic Press (1974).
28. B. E. Launder and C. H. Priddin, "A Comparison of Some Proposals for the Mixing Length Near a Wall," International Journal of Heat Mass Transfer 16:700-702 (1973).
29. F. H. Clauser, "The Turbulent Boundary Layer," Vol. IV of Advances in Applied Mechanics, Academic Press, New York (1956).
30. H. Schlichting, Boundary Layer Theory, McGraw-Hill Book Company (1979).
31. F. P. Bretherton, "Slow Viscous Motion around a Cylinder in Simple Shear," Journal of Fluid Mechanics 12:591 (1962).
32. H. Hasimoto, "On the Periodic Fundamental Solutions of the Stokes Equations and Their Application to Viscous Flow Past a Cubic Array of Spheres," Journal of Fluid Mechanics 5:317-328 (1959).

BIBLIOGRAPHY [continuation]

33. A. S. Sangani and A. Acrivos, "Slow Flow Past Periodic Arrays of Cylinders with Application to Heat Transfer," International Journal of Multiphase Flow 8(3):193-206 (1982).
34. A. S. Sangani and A. Acrivos, "Slow Flow Through a Periodic Array of Spheres," International Journal of Multiphase Flow 8(4):343-360 (1982).
35. R. Welle, "Void Fraction, Bubble Velocity and Bubble Size in Two-Phase Flow," International Journal of Multiphase Flow 11(3) (1985).
36. C. L. Merkle and S. Deutsch, "Drag Reduction by Microbubbles: Current Research Status," AIAA Shear Flow Conference, Boulder, CO (1985).
37. S. W. Beyerlin, K. R. Cossmann and H. J. Richter, "Prediction of Bubble Concentration Profiles in Vertical Turbulent Two-Phase Flow," International Journal of Multiphase Flow 11(5) (1985).
38. T. Nejat Vejiroglu and A. E. Bergles (eds), Multiphase Flow and Heat Transfer III, Elsevier Science Publishers, Amsterdam, The Netherlands (1983).
39. B. E. Launder, W. C. Reynolds, W. Rodi, J. Mathieu, and D. Jeandel, Turbulence Models and Their Applications, Vol. 2, Editions Eyrolles, Paris, France (1984).

BIBLIOGRAPHY [continuation]

40. Pal, S., W. Seelig, J. Cimbala, C. L. Merkle and S. Deutsch,
"Microbubble Drag Reduction," Proceedings of the 16th
Symposium on Naval Hydrodynamics, Berkeley, CA (July 1986).

APPENDIX A

THE FOURIER SERIES EXPANSIONS

In order to obtain expressions (2.3.8), several Fourier series expansions were obtained:

$$\cosh k\theta = \frac{1}{\pi k} \sinh k\pi + \sum_{n=1}^{\infty} \frac{2k/\pi}{n^2 + k^2} \sinh k\pi \cos n\pi \cos n\theta, \quad (\text{A.1})$$

$$\begin{aligned} \theta \sinh k(\pi - \theta) = & -\frac{1}{k} + \frac{1}{\pi k^2} \sinh k\pi + \sum_{n=1}^{\infty} \frac{2(k^2 - n^2)}{\pi(n^2 + k^2)^2} \sinh k\pi \cos n\theta \\ & - \sum_{n=1}^{\infty} \frac{2k \cos n\pi}{n^2 + k^2} \cos n\theta, \end{aligned} \quad (\text{A.2})$$

$$\begin{aligned} \theta \cosh k(\pi - \theta) = & - \sum_{n=1}^{\infty} \frac{2n}{\pi(n^2 + k^2)} \cos n\pi \sinh k\pi \sin n\theta \\ & + \sum_{n=1}^{\infty} \frac{4kn}{\pi(n^2 + k^2)^2} \sinh k\pi \sin n\theta, \end{aligned} \quad (\text{A.3})$$

$$\sinh k\theta = - \sum_{n=1}^{\infty} \frac{2n \cos n\pi}{\pi(n^2 + k^2)} \sinh k\pi \sin n\theta, \quad (\text{A.4})$$

$$\begin{aligned} \theta^2 \sinh k(\pi - \theta) = & \sum_{n=1}^{\infty} \frac{4n(3k^2 - n^2)}{\pi(n^2 + k^2)^3} \sinh k\pi \sin n\theta \\ & - \sum_{n=1}^{\infty} \frac{8kn}{(n^2 + k^2)^2} \cos n\pi \sin n\theta, \end{aligned} \quad (\text{A.5})$$

$$\begin{aligned} \theta \cosh k\theta = & - \sum_{n=1}^{\infty} \frac{2n}{n^2 + k^2} \cos n\pi \cosh k\pi \sin n\theta \\ & + \sum_{n=1}^{\infty} \frac{4nk}{\pi(n^2 + k^2)^2} \sinh k\pi \sin n\theta \quad , \quad (A.6) \end{aligned}$$

$$\begin{aligned} \theta^2 \cosh k(\pi - \theta) = & - \frac{2}{k^2} + \frac{2}{\pi k^3} \sinh k\pi + \sum_{n=1}^{\infty} \frac{4(n^2 - k^2)}{(n^2 + k^2)^2} \cos n\pi \cos n\theta \\ & + \sum_{n=1}^{\infty} \frac{4k(k^2 - 3n^2)}{\pi(n^2 + k^2)^3} \sinh k\pi \cos n\theta \quad , \quad (A.7) \end{aligned}$$

$$\begin{aligned} \theta \sinh k\theta = & \frac{1}{k} \cosh k\pi - \frac{1}{\pi k^2} \sinh k\pi + \sum_{n=1}^{\infty} \frac{2k \cos n\pi}{n^2 + k^2} \cosh k\pi \cos n\theta \\ & - \sum_{n=1}^{\infty} \frac{2(k^2 - n^2)}{\pi(k^2 + n^2)^2} \cos n\pi \sinh k\pi \cos n\theta \quad . \quad (A.8) \end{aligned}$$

A combination of expressions (A.1) with (A.2) and of (A.3) with (A.4) leads to Eq. (2.3.8d) and Eq. (2.3.8a), respectively. Equation (2.3.8d) is obtained from expressions (A.4), (A.5) and (A.6), while Eq. (2.3.8c) stems from (A.1), (A.7) and (A.8).

APPENDIX B

THE CONTOUR INTEGRALS

To integrate Eq. (3.3.17) we use Cauchy's Residue Theorem. In order to perform the integrations we need the following expressions

$$\frac{\partial W}{\partial z} = \sum_{n=1}^N \left\{ \frac{i\Gamma\pi}{\lambda} \cot \frac{\pi}{\lambda} (z - z_n) - G_n \left(\frac{\pi a}{\lambda} \right)^2 \csc^2 \frac{\pi}{\lambda} (z - z_n) \right\}, \quad (B.1)$$

$$\begin{aligned} \frac{\partial W}{\partial t} = & \sum_{n=1}^N \left\{ \frac{dG_n}{dt} \left(\frac{\pi a}{\lambda} \right)^2 \cot \frac{\pi}{\lambda} (z - z_n) \right. \\ & \left. - U_n \left[-G_n \left(\frac{\pi a}{\lambda} \right)^2 \csc^2 \frac{\pi}{\lambda} (z - z_n) + \frac{i\Gamma\pi}{\lambda} \cot \frac{\pi}{\lambda} (z - z_n) \right] \right\}. \end{aligned} \quad (B.2)$$

The integral $\int_{C_m} \frac{\partial W}{\partial z} dz$ leads to integrals of the type

$$\int_{C_m} \cot \frac{\pi}{\lambda} (z - z_n) dz = \begin{cases} 0 & \text{if } n \neq m \\ 2\lambda i & \text{if } n = m \end{cases}, \quad (B.3)$$

$$\int_{C_m} \csc^2 \frac{\pi}{\lambda} (z - z_n) dz = 0 \quad n = 1, \dots, N. \quad (B.4)$$

The integral $\int_{C_m} \left(\frac{\partial W}{\partial z} \right)^2 dz$ leads to integrals of the type

$$\begin{aligned} & \int_{C_m} \csc^2 \frac{\pi}{\lambda} (z - z_k) \cot \frac{\pi}{\lambda} (z - z_\ell) dz \\ & = \begin{cases} 0 & \text{if } k \neq m \text{ and } \ell \neq m \\ -2\lambda i \csc^2 \frac{\pi}{\lambda} (z_m - z_\ell) & \text{if } k = m \text{ and } \ell \neq m \\ 2\lambda i \csc^2 \frac{\pi}{\lambda} (z_m - z_k) & \text{if } k \neq m \text{ and } \ell = m \\ 0 & \text{if } k = \ell = m \end{cases}, \end{aligned} \quad (B.5)$$

$$\int_{C_m} \cot \frac{\pi}{\lambda} (z - z_k) \cot \frac{\pi}{\lambda} (z - z_l) dz$$

$$= \begin{cases} 0 & \text{if } k \neq m \text{ and } l \neq m \\ 2\lambda i \cot \frac{\pi}{\lambda} (z_m - z_k) & \text{if } k \neq m \text{ and } l = m \\ 2\lambda i \cot \frac{\pi}{\lambda} (z_m - z_l) & \text{if } k = m \text{ and } l \neq m \\ 0 & \text{if } k = l = m \end{cases} \quad (B.6)$$

The integral $\int_{C_m} \frac{\partial W}{\partial t} dz$ leads to integrals of the type (B.3) and (B.4). With these results and taking into consideration the appropriate coefficients, Eqs. (3.3.8) can be readily obtained.

For the image system, the expressions to integrate in Eq. (3.3.17) are

$$\frac{\partial W}{\partial z} = \sum_{n=1}^N \left\{ \frac{i\Gamma\pi}{\lambda} \cot \frac{\pi}{\lambda} (z - z_n) - \frac{i\Gamma\pi}{\lambda} \cot \frac{\pi}{\lambda} (z - \bar{z}_n) \right.$$

$$\left. - G_n \left(\frac{\pi a}{\lambda} \right)^2 \csc^2 \frac{\pi}{\lambda} (z - z_n) - \bar{G}_n \left(\frac{\pi a}{\lambda} \right)^2 \csc^2 \frac{\pi}{\lambda} (z - \bar{z}_n) \right\} \quad , \quad (B.7)$$

$$\frac{\partial W}{\partial t} = \sum_{n=1}^N \left\{ - \frac{dG_n}{dt} \left(\frac{\pi a}{\lambda} \right)^2 \csc^2 \frac{\pi}{\lambda} (z - z_n) \right.$$

$$\left. - \frac{d\bar{G}_n}{dt} \left(\frac{\pi a}{\lambda} \right)^2 \csc^2 \frac{\pi}{\lambda} (z - \bar{z}_n) - \frac{i\Gamma\pi}{\lambda} U_n \cot \frac{\pi}{\lambda} (z - z_n) \right.$$

$$\left. + \frac{i\Gamma\pi}{\lambda} \bar{U}_n \cot \frac{\pi}{\lambda} (z - \bar{z}_n) + U_n G_n \left(\frac{\pi a}{\lambda} \right)^2 \csc^2 \frac{\pi}{\lambda} (z - z_n) \right.$$

$$\left. + \bar{U}_n \bar{G}_n \left(\frac{\pi a}{\lambda} \right)^2 \csc^2 \frac{\pi}{\lambda} (z - \bar{z}_n) \right\} \quad . \quad (B.8)$$

From these expressions it is obvious that in Blasius equations only Eq. (3.3.18b) generates more terms.

With expression (B.7), Eq. (3.3.18b) produces, in addition to (B.5) and (B.6), integrals of the following type

$$\int_{C_m} \cot \frac{\pi}{\lambda} (z - \bar{z}_\ell) \cot \frac{\pi}{\lambda} (z - \bar{z}_j) dz = 0 \quad \text{for any } \ell \text{ or } j.$$

$$\begin{aligned} & \int_{C_m} \cot \frac{\pi}{\lambda} (z - z_\ell) \cot \frac{\pi}{\lambda} (z - \bar{z}_j) dz \\ &= \begin{cases} 0 & \text{if } \ell \neq m \text{ any } j \\ 2\lambda i \cot \frac{\pi}{\lambda} (z_m - \bar{z}_j) & \text{if } \ell = m \text{ any } j \end{cases}, \end{aligned} \quad (B.10)$$

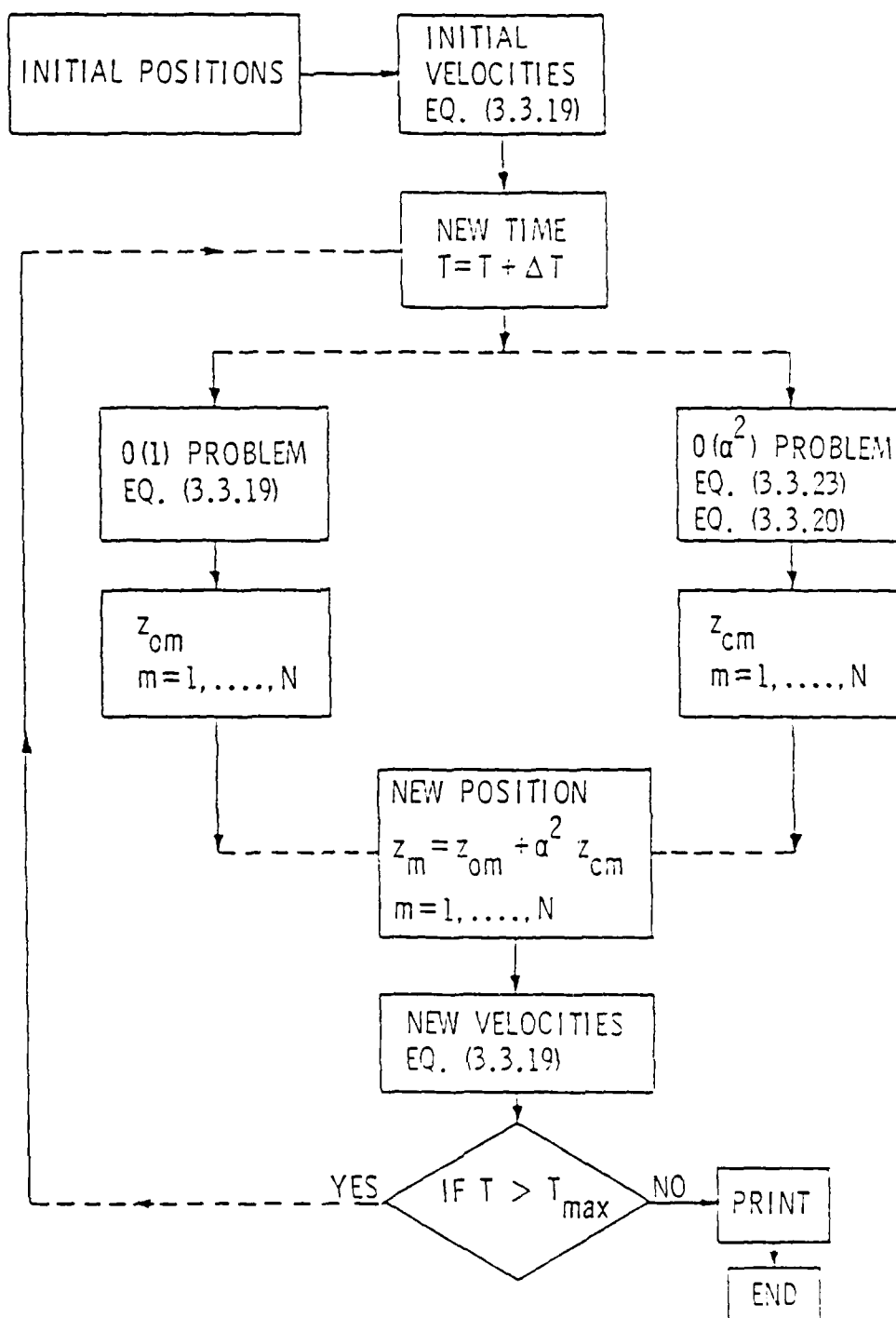
$$\begin{aligned} & \int_{C_m} \cot \frac{\pi}{\lambda} (z - z_\ell) \csc^2 \frac{\pi}{\lambda} (z - \bar{z}_j) dz \\ &= \begin{cases} 0 & \text{if } \ell \neq m \text{ any } j \\ 2\lambda i \csc^2 \frac{\pi}{\lambda} (z_m - \bar{z}_j) & \text{if } \ell = m \text{ any } j \end{cases}, \end{aligned} \quad (B.11)$$

$$\begin{aligned} & \int_{C_m} \cot \frac{\pi}{\lambda} (z - \bar{z}_j) \csc^2 \frac{\pi}{\lambda} (z - \bar{z}_\ell) dz \\ &= \begin{cases} 0 & \text{if } \ell \neq m \text{ any } j \\ -2\lambda i \csc^2 \frac{\pi}{\lambda} (z_m - \bar{z}_j) & \text{if } \ell = m \text{ any } j \end{cases}. \end{aligned} \quad (B.12)$$

With these results at hand, Eq. (3.4.5) follows easily.

APPENDIX C

THE HOLLOW VORTEX SHEET EVOLUTION CODE



```

      IMPLICIT REAL*8(A-H,O-Y)
      IMPLICIT COMPLEX*16(Z)
      COMMON/BLK1/J,N,PI
      COMMON/BLK2/ZPOS
      COMMON/BLK3/ZVEL
      COMMON/BLK4/DT
      COMMON/BLK5/ZPC
      DIMENSION ZPOS(100),ZPOS0(50),ZPOS1(50)
      DIMENSION ZVEL(100)
      PRINT*,'ENTER N,M'
      READ(5,*) N,M
      PRINT*,'ENTER AD,DEL'
      READ(5,*) AD,DEL
      N1=N+1
      N2=N/2
      N21=N2+1
      DT=1/DFLOAT(500)
      PI=DACOS(-1.D0)
      ZI=DCMPLX(0.D0,1.D0)
      DO 10 I=1,N
        X=(I-1)/DFLOAT(N)
        Y=-AD*DSIN(2*PI*(X))
        ZPOS(I)=DCMPLX(X,Y)
        WRITE(21,*) X,Y
10    CONTINUE
      ZVEL(1)=DCMPLX(0.0D0,0.0D0)
      ZVEL(N21)=DCMPLX(0.0D0,0.0D0)
      DO 20 J=2,N2
        ZPC=ZPOS(J)
        ZVEL(J)=ZI*(DCONJG(ZSCOT(J,ZPOS(J))))/N
        ZVEL(N+2-J)=-ZVEL(J)
20    CONTINUE
      DO 60 K=1,M
        T=T+DT
        CALL ORDER0(ZPOS0)
        CALL ORDER1(ZPOS1)
        DO 30 I=2,N2
          ZPOS(I)=ZPOS0(I)+(DEL**2)*ZPOS1(I)
          ZPOS(N+2-I)=1.D0-ZPOS(I)
30    CONTINUE
        DO 40 J=2,N2
          ZPC=ZPOS(J)
          ZVEL(J)=ZI*(DCONJG(ZSCOT(J,ZPOS(J))))/N
          ZVEL(N+2-J)=-ZVEL(J)
40    CONTINUE
        IF(MOD(DFLOAT(K),40.D0).EQ.0.D0) THEN
          L1=21+K/40
          DO 50 I=1,N1
            X=DREAL(ZPOS(I))
            Y=DIMAG(ZPOS(I))
            WRITE(L1,*) X,Y
50    CONTINUE
          WRITE(L1,*) T
          ENDIF
60    CONTINUE

```

```

ZD4=DT*ZRHS1(ZPC)
ZPOUT=ZPIN+DCONJG(ZD1+2*ZD2+2*ZD3+ZD4)/6.0D0
RETURN
END

```

```

SUBROUTINE RUNTA2(DT,ZPIN,ZVIN,ZPOUT)
IMPLICIT REAL*8(A-H,O-Y)
IMPLICIT COMPLEX*16(Z)
COMMON/BLK5/ZPC
ZDV1=DT*ZRHS2(ZPIN,ZVIN)
ZDP1=DT*ZRHS3(ZVIN)
ZPC=ZPIN+DCONJG(ZDP1)/2.0D0
ZVC=ZVIN+DCONJG(ZDV1)/2.0D0
ZDV2=DT*ZRHS2(ZPC,ZVC)
ZDP2=DT*ZRHS3(ZVC)
ZPC=ZPIN+DCONJG(ZDP2)/2.0D0
ZVC=ZVIN+DCONJG(ZDV2)/2.0D0
ZDV3=DT*ZRHS2(ZPC,ZVC)
ZDP3=DT*ZRHS3(ZVC)
ZPC=ZPIN+DCONJG(ZDP3)
ZVC=ZVIN+DCONJG(ZDV3)
ZDV4=DT*ZRHS2(ZPC,ZVC)
ZDP4=DT*ZRHS3(ZVC)
ZPOUT=ZPIN+DCONJG(ZDP1+2*ZDP2+2*ZDP3+ZDP4)/6.0D0
RETURN
END

```

```

FUNCTION ZRHS1(ZPC)
IMPLICIT REAL*8(A-H,O-Y)
IMPLICIT COMPLEX*16(Z)
COMMON/BLK1/J,N,PI
ZI=DCMPLX(0.0D0,1.0D0)
ZRHS1=-ZI*ZSCOT(J,ZPC)/N
RETURN
END

```

```

FUNCTION ZRHS2(ZPC,ZVC)
IMPLICIT REAL*8(A-H,O-Y)
IMPLICIT COMPLEX*16(Z)
COMMON/BLK1/J,N,PI
COMMON/BLK2/ZPOS
COMMON/BLK3/ZVEL
DIMENSION ZPOS(100),ZVEL(100)
ZI=DCMPLX(0.0D0,1.0D0)
ZS1=ZSCOT(J,ZPC)
ZS2=DCMPLX(0.0D0,0.0D0)

```

STOP
END

```
SUBROUTINE ORDER0(ZPOS0)
IMPLICIT REAL*8(A-H,O-Y)
IMPLICIT COMPLEX*16(Z)
COMMON/BLK1/J,N,PI
COMMON/BLK2/ZPOS
COMMON/BLK4/DT
COMMON/BLK5/ZPC
DIMENSION ZPOS0(50),ZPOS(100)
N2=N/2
DO 10 J=2,N2
    ZPC=ZPOS(J)
    CALL RUNTA1(DT,ZPOS(J),ZPOS0(J))
10 CONTINUE
RETURN
END
```

```
SUBROUTINE ORDER1(ZPOS1)
IMPLICIT REAL*8(A-H,O-Y)
IMPLICIT COMPLEX*16(Z)
COMMON/BLK1/J,N,PI
COMMON/BLK2/ZPOS
COMMON/BLK3/ZVEL
COMMON/BLK4/DT
COMMON/BLK5/ZPC
DIMENSION ZPOS(100),ZPOS1(50),ZVEL(100)
N2=N/2
DO 10 J=2,N2
    ZPC=ZPOS(J)
    CALL RUNTA2(DT,ZPOS(J),ZVEL(J),ZPOS1(J))
10 CONTINUE
RETURN
END
```

```
SUBROUTINE RUNTA1(DT,ZPIN,ZPOUT)
IMPLICIT REAL*8(A-H,O-Y)
IMPLICIT COMPLEX*16(Z)
COMMON/BLK5/ZPC
ZD1=DT*ZRHS1(ZPIN)
ZPC=ZPIN+DCONJG(ZD1)/2.0D0
ZD2=DT*ZRHS1(ZPC)
ZPC=ZPIN+DCONJG(ZD2)/2.0D0
ZD3=DT*ZRHS1(ZPC)
ZPC=ZPIN+DCONJG(ZD3)
```



```

      ZS3=DCMPLX(0.D0,0.D0)
      DO 10 I=1,N
        IF(I.EQ.J) GO TO 10
        Z=PI*(ZPC-ZPOS(I))
        ZS2=ZS2+(ZS1-ZSCOT(I,ZPOS(I)))/((ZDSIN(Z))**2)
        ZS3=ZS3+(ZVC-ZVEL(I)))/((ZDSIN(Z))**2)
10    CONTINUE
      ZS2=4*ZI*ZS2/(N**2)
      ZS3=-2*(ZI*ZS3+2*DIMAG(ZS3))/N
      ZRHS2=PI*(ZS2+ZS3)
      RETURN
      END

```

```

      FUNCTION ZRHS3(ZVC)
      IMPLICIT REAL*8(A-H,O-Y)
      IMPLICIT COMPLEX*16(Z)
      ZRHS3=DCONJG(ZVC)
      RETURN
      END

```

```

      FUNCTION ZSCOT(L,ZP)
      IMPLICIT REAL*8(A-H,O-Y)
      IMPLICIT COMPLEX*16(Z)
      COMMON/BLK1/J,N,PI
      COMMON/BLK2/ZPOS
      COMMON/BLK5/ZPC
      DIMENSION ZPOS(100)
      ZS=DCMPLX(0.D0,0.D0)
      DO 10 I=1,N
        IF(I.EQ.L) GO TO 10
        IF(I.EQ.J) THEN
          ZP1=ZPC
        ELSE
          ZP1=ZPOS(I)
        ENDIF
        Z=PI*(ZP-ZP1)
        ZS=ZS+ZDCOS(Z)/ZDSIN(Z)
10    CONTINUE
      ZSCOT=ZS
      RETURN
      END

```

```

      FUNCTION ZDSIN(Z)
      IMPLICIT REAL*8(A-H,O-Y)
      IMPLICIT COMPLEX*16(Z)
      ZI=DCMPLX(0.D0,1.D0)

```

```
XR=DREAL(Z)
XI=DIMAG(Z)
X=DSIN(XR)*DCOSH(XI)
Y=DCOS(XR)*DSINH(XI)
ZDSIN=X+ZI*Y
RETURN
END
```

```
FUNCTION ZDCOS(Z)
IMPLICIT REAL*8(A-H,O-Y)
IMPLICIT COMPLEX*16(Z)
ZI=DCMPLX(0.D0,1.D0)
XR=DREAL(Z)
XI=DIMAG(Z)
X=DCOS(XR)*DCOSH(XI)
Y=DSIN(XR)*DSINH(XI)
ZDCOS=X-ZI*Y
RETURN
END
```

APPENDIX D

THE MANGLER-LEVEL-LEES TRANSFORMATION

In Chapter IV, the system of equations to be integrated is

$$\frac{\partial u}{\partial x} + \frac{\partial v}{\partial y} = 0 \quad , \quad (D.1a)$$

$$\frac{\partial}{\partial x} (Xu) + \frac{\partial}{\partial y} (Xv) = 0 \quad , \quad (D.1b)$$

$$(1 - X) \left[u \frac{\partial u}{\partial x} + v \frac{\partial u}{\partial y} \right] = (1 - X) \frac{\partial}{\partial y} \left[v \epsilon^* \frac{\partial u}{\partial y} \right] \\ + g \frac{\partial}{\partial x} \int_y^\infty X dy + \frac{\mu_l}{\rho_l} \frac{\partial}{\partial y} \left[(1 + \mu_{sp}) \frac{\partial u}{\partial y} \right] \quad , \quad (D.1c)$$

where $\epsilon^* = \epsilon/v$.

If we define a stream function ψ according to

$$u = \frac{\partial \psi}{\partial y} \quad ; \quad v = - \frac{\partial \psi}{\partial x} \quad , \quad (D.2)$$

then the continuity equation is identically satisfied.

With a Mangler-Levy-Lees type of transformation, defined by

$$\xi(x) = \rho_l \mu_{t_{ref}} U_\infty x \quad , \quad (D.3a)$$

$$\eta(x, y) = \frac{\rho_l U_\infty y}{\sqrt{2\xi}} \quad , \quad (D.3b)$$

$$\psi(\xi, \eta) = \sqrt{2\xi} f(\xi, \eta) \quad , \quad (D.3c)$$

the two remaining equations become

$$2\xi f' \frac{\partial X}{\partial \xi} - (f + 2\xi f_\xi) \frac{\partial X}{\partial \eta} = 0, \quad (\text{D.4a})$$

$$\frac{\mu_l}{\mu_{t_{\text{ref}}}} \frac{\partial}{\partial \eta} [(1 + \mu_{\text{sp}}) f''] + (1 - X) \left\{ \frac{\mu_l(1 + \mu_{\text{sp}})}{\mu_{t_{\text{ref}}}} \frac{\partial}{\partial \eta} \left[\frac{\epsilon^* f''}{1 - X} \right] + f f'' \right\}$$

$$\frac{g}{\rho_l U_\infty^3} \sqrt{2\xi} \left[1 + 2\xi \frac{\partial}{\partial \xi} - \eta \frac{\partial}{\partial \eta} \right] \left\{ \int_n^\infty X d\zeta \right\} = (1 - X) 2\xi [f'_\xi f' - f f''_\xi]. \quad (\text{D.4b})$$

The corresponding boundary conditions at the wall become

$$f'(\xi, 0) = 0, \quad (\text{D.5a})$$

$$\sqrt{2\xi} f(\xi, 0) = - \frac{1}{\mu_{t_{\text{ref}}} U_\infty} \int_0^\xi v_w(\zeta) d\zeta, \quad (\text{D.5b})$$

while the farfield boundary condition is

$$f'(\xi, \eta) \rightarrow 1 \text{ as } \eta \rightarrow \infty. \quad (\text{D.5c})$$

The volume fraction boundary conditions remain as expressed in Eq. (4.6.1).

In order to apply Keller's Box Method, we rewrite the system of equations as

$$F = f', \quad (\text{D.6a})$$

$$G = F' = f'', \quad (\text{D.6b})$$

$$2\xi F X_\xi - (f + 2\xi f_\xi) Y = 0, \quad (\text{D.6c})$$

$$\begin{aligned}
& \frac{\mu_\ell}{\mu_{t_{ref}}} \left[(1 + \mu_{sp}) G \right]' + (1 - X) \left\{ \frac{\mu_\ell (1 + \mu_{sp})}{\mu_{t_{ref}}} \left[\frac{\varepsilon^* G}{1 - X} \right]' + f G \right\} \\
& \frac{g}{\rho_\ell U_\infty^3} \sqrt{2\xi} \left[1 + 2\xi \frac{\partial}{\partial \xi} - \eta \frac{\partial}{\partial \eta} \right] \left\{ \int_\eta^\infty X d\zeta \right\} \\
& = (1 - X) 2\xi [FF_\xi - f_\xi G] \quad , \quad (D.6d)
\end{aligned}$$

with the boundary conditions

$$\begin{aligned}
F &= 0 & \text{at } \eta &= 0 \quad , \\
F &\rightarrow 1 & \text{as } \eta &\rightarrow \infty \quad , \\
X &= CX_D & \text{at } \eta &= 0 \quad , \\
f &= -\frac{1}{\sqrt{2\xi}} \frac{\rho_g Q_g}{(1 - X)} \left(\frac{\xi - \xi_1}{\xi_2 - \xi_1} \right) & \text{at } \eta &= 0 \quad ,
\end{aligned} \quad (D.6e)$$

where D is the interval, in the transformed space (ξ, η) , corresponding to $[a, b]$.

For the sake of completeness we give now, in transformed variables, the expressions used for the eddy viscosity.

In the inner region we have

$$\varepsilon_i = \frac{K^2}{\mu_\ell} \sqrt{2\xi} f'' \eta^2 \left[1 - e^{\frac{y^+}{A^+} \left(\frac{\rho_w}{\rho} \frac{\tau_w}{\tau_w} \right)^{1/2}} \right]^2 \quad , \quad (D.7a)$$

where

$$y^+ = \eta \left[\frac{\mu_w}{2} \sqrt{2\xi} f''_{\eta=0} \frac{(1 - X)^2}{1 - X_w} \right]^{1/2} \quad , \quad (D.7b)$$

and

$$\frac{\rho_w}{\rho} \frac{\tau}{\tau_w} = \frac{1 - X_w}{1 - X} \frac{\mu}{\mu_w} \frac{f''}{f''_{\eta=1}} \quad (D.7c)$$

In the outer region we used

$$\epsilon_0 = \alpha \frac{\sqrt{2\xi}}{\mu_k} \int_0^{\infty} [1 - (1 - X)f'] d\eta \quad (D.7d)$$

Finite differencing the system (D.6) according to Keller's Method [27], leads to a block tridiagonal system, with 3×3 block matrices, for the parabolic momentum equation. The volume fraction equation, a hyperbolic equation, is integrated separately, in each cycle, by a different solver. The differencing scheme chosen for this equation is second order accurate.

Since the numerical methods are not the object of this dissertation, we decline from including the finite difference equations that lead to the code presented in Appendix E.

APPENDIX E

THE BOUNDARY LAYER CODE

The code presented in this appendix was designed for the flat plate boundary layer. It corresponds to the numerical integration of the system (D.6).

As it is, the code cannot be used for the computation of the flow around an axisymmetric body. However, the changes to be introduced are rather straightforward. In this case, the Reynolds equations expressed in body fitted coordinates should be transformed through the Stokes stream function and the axisymmetric Mangler-Levy-Lees transformation to obtain the self-starting system of equations [27]. The system obtained in the previous appendix must be the special case of zero pressure gradient. Some entries of the matrices of the block tridiagonal system will be different, however, the numerical solver is exactly the same and needs no modifications. It should be noted that the body shape will also affect both equations by the definition of the Stokes stream function and the Mangler-Levy-Lees transformation.

Even though confident about the code presented, the author wants to issue a word of caution. The ability of the code to resolve high void fraction gradients is limited.

The code uses second order differencing everywhere and is designed for a variable grid in either the streamwise or the cross-stream directions.

Because the void fraction transport equation introduces in the flow strong streamwise gradients, there exists the need of a grid generator in the streamwise direction. This addition can be appended to the code without any modifications.


```

*****
*
*      MAIN PROGRAM
*
*****

```

```

IMPLICIT REAL*8(A-H,O-Z)
DIMENSION A(3,3,101),B(3,3,101),C(3,3,101),R(3,101)
DIMENSION AL(3,3,101),BET(3,3,101),DETA(101),BUOY(101)
DIMENSION Y(3,101),Z(3,101),ITER(1000),ALFA(1000),V(3,1)
DIMENSION SFI(101),BFI(101),GI(101),ZI(1000),XI(101)
DIMENSION SFI1(101),BFI1(101),GI1(101),WKAREA(10)
DIMENSION AHAT(101),BHAT(101),CHAT(101),DHAT(1101)
DIMENSION P(101),Q(101),S(101),REX(1000),YDEL(101)
DIMENSION SFI2(101),BFI2(101),GI2(10-1),CF(1000),XI(101)
DIMENSION THMO(1000),XDEL(500),QBL(500),XI2(101),DU(3,3)
DIMENSION UPLUS(101),YPLUS(101),SUM(101),SUM1(101)
DIMENSION SUM2(101),BUOY1(51),SHAPE(1000),ETA(101)
DIMENSION PXL(101),PXL1(101),THBL(1000),SFI3(101)
COMMON/BLK1/DETA,CE,N
COMMON/BLK2/ALFA,IS
COMMON/BLK3/SFI,BFI,GI
COMMON/BLK4/SFI1,BFI1,GI1
COMMON/BLK5/PRTR,PRTR1,PRST,PRST1
COMMON/BLK6/XI,XI1
COMMON/BLK7/ZI,ETA
COMMON/BLK8/PXL,PXL1
COMMON/BLK9/ISINJI,EREF,VISCL,VISCT
COMMON/BLK10/GRAV,ROUL,UE
COMMON/BLK11/SUM,SUM1,SUM2
COMMON/BLK12/YPLUS,USTAR
COMMON/BLK13/SFI2,XI2
COMMON/BLK14/BUOY,BUOY1
STRFAC=DLOG(10.0D0)
EPS=1.0D-5
PI=DACOS(-1.0D0)
VISCL=1010D-6
VISC=17.9D-6
ROUL=997.3
ROUG=1.21
GRAV=9.81
PRINT*,'ENTER M'
READ(5,*) M

```

C
C
C

Specification of flow parameters.

```

PRINT*,'ENTER INITIAL POSITION'
READ(5,*) PIIC
PRINT*,'ENTER FINAL POSITION'
READ(5,*) PFIC
PRINT*,'ENTER VFI,QG'
READ(5,*) VFI,QG

```

```

PRINT*, 'ENTER UE'
READ(5,*) UE
ISINJI=0
ISINJF=0
POSEND=0.0D0
DZIC=1.0D0/DFLOAT(M)
DZI=DZIC
VISCT=VISCL
PRTR=0.0D0
PRST=1.0D0
POS=0.0D0
CE=1.05D0
IS=1
YDEL(1)=0.0D0
ALFA(1)=0.0D0

```

```

C
C      Establishment of the cross stream grid which obeys
C      a geometric progression law.
C

```

```

ETA(1)=0.0D0
DETA(1)=0.0D0
DETA(2)=0.005
ETA(2)=DETA(2)
K=2

```

```

C
C      Determination of the number of grid points across
C      the boundary layer.
C

```

```

1 DETA(K+1)=DETA(K)*CE
  ETA(K+1)=ETA(K)+DETA(K+1)
  ETAE=DETA(2)*(CE**(K-1)-1.0D0)/(CE-1.0D0)
  IF(ETAE.LE.8.0D0) THEN
    N=K
    K=K+1
    GO TO 1
  ENDIF
  NP1=N+1

```

```

C
C      Specification of the starting parabolic profile.
C

```

```

ZI(1)=0.0D0
SFI(1)=0.0D0
BFI(1)=0.0D0
XI(1)=0.0D0
XI1(1)=0.0D0
GI(1)=2.0D0/ETAE
YDEL(1)=0.0D0
BUOY(1)=0.0D0
BUOY1(1)=0.0D0
SUM(1)=0.0D0
SUM1(1)=0.0D0
SUM2(1)=0.0D0
PXL(1)=0.0D0
PXL1(1)=0.0D0
SFI3(1)=0.0D0

```

```

DO 5 K=2,NP1
  IF(ETA(K).LE.(5.0D0)) IDEL=K
  SFI(K)=(ETA(K)**2)*(1.0D0-ETA(K)/
>(3*ETAE))/ETAE
  BFI(K)=ETA(K)*(2.0D0-ETA(K)/ETAE)/ETAE
  GI(K)=2*(1.0D0-ETA(K)/ETAE)/ETAE
  XI(K)=0.0D0
  XI1(K)=0.0D0
  BUOY(K)=0.0D0
  BUOY1(K)=0.0D0
  SUM(K)=0.0D0
  SUM1(K)=0.0D0
  SUM2(K)=0.0D0
  PXL(K)=0.0D0
  PXL1(K)=0.0D0
  SFI3(K)=0.0D0
  YDEL(K)=BFI(K)
5 CONTINUE
10 IF(IS.EQ.ISINJI) THEN
  DO 15 K=1,NP1
    SFI2(K)=SFI3(K)
    SFI1(K)=SFI2(K)
    SFI(K)=SFI2(K)
    BFI1(K)=BFI2(K)
    BFI(K)=BFI2(K)
    GI1(K)=GI2(K)
    GI(K)=GI2(K)
15 CONTINUE
  ENDIF
C
C   Computation of the streamwise Reynolds number.
C
  POS1=POS
  POS=POS+DZI/VISCT
20 IF(IS.EQ.1) THEN
  REX(1)=0.0D0
  ELSE
  REX(IS)=POS/VISCL
  ENDIF
C
C   Computation of the transition parameter that switches
C   on the turbulence model.
C
  IF(REX(IS).LT.4.D5) THEN
    PRTR=0.0D0
C
C   Computation of the laminar boundary layer edge
C   parameters.
C
    PRCF=DSQRT(2.0D0)*GI(1)
    PRSFI=(SFI(IDEL+1)-SFI(IDEL))/DETA(IDEL)
    PRBFI=(BFI(IDEL+1)-BFI(IDEL))/DETA(IDEL)
    SFIID=SFI(IDEL)+PRSFI*(5.0D0-ETA(IDEL))
    BFIID=BFI(IDEL)+PRBFI*(5.0D0-ETA(IDEL))
    PREV--(SFIID-5.0D0*BFIID)/DSQRT(2.0D0)

```

```

ELSE
  IF( REX( IS ).LE.6.D5) THEN
    X=REX( IS )/1.D5
    PRTR1=PRTR
    X=(X-4.0D0)/2.0D0
    PRTR=(1.0D0+DSIN(PI*(X-0.5D0)))/2.0D0
    PRTR=PRTR**2
  ELSE
    PRTR1=PRTR
    PRTR=1.0D0
  ENDIF
ENDIF

C
C Computation of the boundary layer displacement thickness
C and of the boundary layer momentum thickness.
C

IF( IS.GT.2) THEN
  CALL BLPR( DELSTR, TETSTR )
  THBL( IS-1 )=DSQRT( 2*ZI( IS-1 ) ) * DELSTR / ( UE * ROUL )
  THMO( IS-1 )=DSQRT( 2*ZI( IS-1 ) ) * TETSTR / ( UE * ROUL )

C
C Computation of the boundary layer shape factor.
C

  SHAPE( IS-1 )=THBL( IS-1 ) / THMO( IS-1 )
ENDIF
PRST1=PRST
POSC1=POS1 / ( UE * ROUL )
POSC=POS / ( UE * ROUL )

C
C Determination of the final station of injection taking
C into account the influence of the void fraction.
C

IF( ( IS.GT.ISINJF ).AND.( ISINJF.NE.0 ) ) THEN
  IF( POSC.LE.PFIC ) THEN
    ISINJF=IS
    ETAREF=ETA( NP1 )
  ELSE

C
C Computation of the position downstream from injection
C in terms of the boundary layer thickness.
C

    XDEL( IS-1 )=POSEND / ( ETAREF * DSQRT( 2 * PFIM ) /
    > ( UE * ROUL ) )
    ENDIF
  ENDIF

C
C Determination of the initial station of injection.
C

IF( ( PIIC.GE.POSC1 ).AND.( PIIC.LE.POSC ) ) THEN
  IF( ISINJI.NE.0 ) GO TO 30
  ISINJI=IS
  PIIM=( ZI( IS ) + ZI( IS-1 ) ) / 2.0D0
  POSIN=POS1
  DZIIN=DZI
  VISCTI=VISCT

```

```
PRTRI=PRTR
PRSTI=PRSTI
NIN=N
```

```
C
C
C      Storage of the converged initial injection profile
C      to restart the computations once the final position
C      of injection is determined.
```

```
C
C      DO 25 K=1,NP1
C          SFI3(K)=SFI2(K)
C          SFI2(K)=SFI(K)
C          BFI2(K)=BFI(K)
C          GI2(K)=GI(K)
25  CONTINUE
30  ENDIF
```

```
C
C      Determination of the final station of injection.
```

```
C
C      IF((PFIC.GE.POSC1).AND.(PFIC.LE.POSC)) THEN
C          IF(ISINJF.NE.0) GO TO 35
C          ISINJF=IS
C          ETAREF=ETA(NP1)
C          PFIM=ZI(IS)+DZI/2.0D0
C          IS=ISINJI
C          POS=POSIN
C          DZIC=DZIIIN
C          VISCTF=VISCT
C          VISCT=VISCTI
C          PRTR=PRTRI
C          PRST=PRSTI
C          N=NIN
C          NP1=N+1
```

```
C
C      Restart of the computations from the initial position of
C      injection. With the final position of injection in the
C      transformed space determined, injection and the transport
C      equation for the void fraction will be turned on.
```

```
C
C      GO TO 10
35  ENDIF
```

```
C
C      These commands change the boundary conditions during
C      injection according to a statement of mass conservation.
```

```
C
C      IF((ZI(IS).GT.PIIM).AND.(ZI(IS).LT.PFIM)) THEN
C          PRPOS=(PFIM-PIIM)/10.0D0
C          PRINJ=ROUG*QG/((PFIM-PIIM)*DSQRT(2.0D0*ZI(IS)))
C          IF(ZI(IS).LE.(PIIM+PRPOS)) THEN
C              XI(1)=VFI*(ZI(IS)-PIIM)/PRPOS
C          ELSE
C              IF(ZI(IS).GE.(PFIM-PRPOS)) THEN
C                  XI(1)=VFI-VFI*(ZI(IS)-PFIM+PRPOS)/PRPOS
C              ELSE
C                  XI(1)=VFI
C              ENDIF
C          ENDIF
```



```

        DU(L,J)=AL(J,L,K-1)
55      CONTINUE
60      CONTINUE
        DO 65 J=1,3
            V(J,1)=B(I,J,K)
65      CONTINUE
        MS=1
        NS=3
        IA=3
        IDGT=0
C
C      IMSL matrix solver.
C
        CALL LEQT1F(DU,MS,NS,IA,V,IDGT,WKAREA,IER)
        DO 70 J=1,3
            BET(I,J,K)=V(J,1)
70      CONTINUE
75      CONTINUE
        DO 80 J=1,3
            BET(3,J,K)=0.0D0
80      CONTINUE
        DO 90 I=1,2
            DO 85 J=1,3
                AL(I,J,K)=A(I,J,K)-BET(I,3,K)*C(3,J,K-1)
85      CONTINUE
90      CONTINUE
        DO 95 J=1,3
            AL(3,J,K)=A(3,J,K)
95      CONTINUE
100     CONTINUE
C
C      The backward and forward substitutions of the Lower
C      Upper decomposition of the tridiagonal system.
C
        CALL FORW(N,BET,R,Y)
        CALL BACK(N,Y,C,AL,Z)
C
C      Update of the station computations.
C
        DO 110 K=1,NP1
            SFI(K)=SFI(K)+Z(1,K)
            BFI(K)=BFI(K)+Z(2,K)
            GI(K)=GI(K)+Z(3,K)
110     CONTINUE
C
C      Station convergence test for the momentum equation
C      based on both the wall velocity gradient correction
C      and the outer edge velocity gradient.
C
        IF(DABS(Z(3,1)).GT.EPS) THEN
            ITER(IS)=ITER(IS)+1
            GO TO 40
        ELSE
            IF(DABS(GI(NP1)).GT.EPS) THEN
C

```

```

C      Boundary layer extension based on the zero edge
C      velocity gradient condition.
C
C      CALL EXTEND(ETA)
C      NP1=N+1
C
C      Update of the normed cross stream coordinate.
C
C      DO 120 K=2,NP1
C          YDEL(K)=ETA(K)/ETA(NP1)
120    CONTINUE
C      ITER(IS)=ITER(IS)+1
C      GO TO 40
C    ENDIF
C
C      Computation of the void fraction.
C
C      IF((IS.GE.ISINJI).AND.(ISINJF.NE.0)) THEN
C          CALL VOLFRG(XI,XI1,ZI)
C
C      Computation of the buoyancy force field according
C      to Archimedes principle.
C
C          CALL ARCHIE(XI,BUOY)
C
C      Convergence of the iteration procedure of the whole
C      system based on the convergence of the wall velocity
C      gradient.
C
C          SYSCON=DABS(SYSCON-GI(1))
C          IF(SYSCON.GT.EPS) THEN
C              SYSCON=DABS(GI(1))
C              ITER(IS)=ITER(IS)+1
C              GO TO 40
C          ENDIF
C      ENDIF
C      SYSCON=0.0D0
C
C      Computation of the skin friction.
C
C      IF(IS.NE.1) THEN
C          CF(IS)=VISCL*GI(1)*DSQRT(2.0D0/ZI(IS))
C      ENDIF
C
C      Station advance and specification of the corresponding
C      starting solution.
C
C      IS=IS+1
C      ITER(IS)=1
C      DO 130 K=1,NP1
C          SFI2(K)=SFI1(K)
C          SFI1(K)=SFI(K)
C          BFI1(K)=BFI(K)
C          GI1(K)=GI(K)
C          XI2(K)=XI1(K)

```



```

      XI1(K)=XI(K)
      SUM2(K)=SUM1(K)
      SUM1(K)=SUM(K)
      BUOY1(K)=BUOY(K)
130  CONTINUE

```

Computation of the boundary layer mass flowrate.

```

      IF((IS.GT.ISINJI).AND.(ISINJF.NE.0)) THEN
        PRQBL=0.0D0
        DO 135 K=2,NP1
          CK=(1.0D0-XI(K))*BFI(K)
          CK1=(1.0D0-XI(K-1))*BFI(K-1)
          PRQBL=PRQBL+(CK+CK1)*DETA(K)
135  CONTINUE
        QBL(IS-1)=PRQBL*DSQRT(ZI(IS-1)/2.0D0)
      ENDIF

```

The end of the computations is commanded at 30 boundary layer thicknesses downstream from injection.

```

      IF(((IS-1).GT.ISINJF).AND.(ISINJF.NE.0)) THEN
        POSEND=POSEND+DZI/(UE*ROUL*VISCTF)
      ENDIF
      IF(XDEL(IS-2).GT.30.0D0) GO TO 150

```

Update of the streamwise stepsize during transition.

```

      IF((PRTR.GT.0.0D0).AND.(PRTR.LT.1.0D0)) THEN
        DZIT=DZIC*(1.0D0-0.5*EREF*PRST*PRTR)
      ELSE
        IF(PRTR.EQ.0.0D0) THEN
          DZI=DZIC
        ELSE
          DZI=DZIC*(1.0D0+0.8*EREF)
        ENDIF
      ENDIF

```

Update of the streamwise stepsize during injection.

```

      IF((ISINJI.NE.0).AND.(ISINJF.NE.0)) THEN
        DZI=DZI/4.0D0
      ENDIF
      IF(IS.GE.(ISINJF+20)) THEN
        DZI=4*DZI
      ENDIF
      ZI(IS)=ZI(IS-1)+DZI
      ALFA(IS)=(ZI(IS)+ZI(IS-1))/(ZI(IS)-ZI(IS-1))

```

Printing statements.

```

      IF(((IS-1).GE.ISINJF).AND.(ISINJF.NE.0)) THEN
        LP=IS-ISINJF-1
        IF(MOD(DFLOAT(LP),15.0D0).EQ.0.0D0) THEN
          L1=31+LP/15

```

```

L2=51+LP/15
L3=71+LP/15
L4=91+LP/15
WRITE(21,*) XDEL(IS-2)

```

C
C
C

Computation of the velocity profile in inner variables.

```

DO 140 K=2,NP1
  UPLUS(K)=BFI(K)/USTAR
  YTRANS=DLOG(YPLUS(K))/STRFAC
  WRITE(L4,*) YTRANS,UPLUS(K)
140 CONTINUE
DO 145 K=1,NP1
  VEL=UE*BFI(K)
  VELGRD=ROUL*(UE**2)*GI(K)/DSQRT(2*ZI(IS-1))
  WRITE(L1,*) VEL,YDEL(K)
  WRITE(L2,*) VELGRD,YDEL(K)
  WRITE(L3,*) XI(K),YDEL(K)
145 CONTINUE
ENDIF
ENDIF
GO TO 15
150 ISEND=IS-3
DO 155 K=2,ISEND
  REXLOG=DLOG(REX(K))/STRFAC

```

C
C
C
C

Computation of the boundary layer thickness and momentum thickness Reynolds numbers.

```

FRICK=1000*CF(K)
RBL=ROUL*UE*THBL(K)/VISCL
RMO=ROUL*UE*THMO(K)/VISCL
RBLLOG=DLOG(RBL)/STRFAC
RMOLOG=DLOG(RMO)/STRFAC
WRITE(120,*) REXLOG,FRICK
WRITE(121,*) REXLOG,RBLLOG
WRITE(122,*) REXLOG,RMOLOG
WRITE(123,*) REXLOG,SHAPE(K)
IF(K.GE.ISINJF) THEN
  QRATIO=ROUG*QG/QBL(K)
  WRITE(124,*) XDEL(K),QRATIO
ENDIF
155 CONTINUE
ENDIF
STOP
END

```

```

*****
*
*      SUBROUTINES
*
*****

```

C
C Subroutine FORW performs the forward substitution of
C the Lower-Upper decomposition of the block tridiagonal
C system.

```

SUBROUTINE FORW(N,BET,R,Y)
IMPLICIT REAL*8 (A-H,O-Z)
DIMENSION Y(3,101),R(3,101),BET(3,3,101)
NP1=N+1
DO 10 J=1,3
  Y(J,1)=R(J,1)
10 CONTINUE
DO 40 K=2,NP1
  DO 30 I=1,2
    B1=0.0D0
    DO 20 J=1,3
      B1=B1+BET(I,J,K)*Y(J,K-1)
20   CONTINUE
    Y(I,K)=R(I,K)-B1
30   CONTINUE
    Y(3,K)=R(3,K)
40 CONTINUE
RETURN
END

```

C
C Subroutine BACK performs the backward substitution of
C the Lower-Upper decomposition of the block tridiagonal
C system.

```

SUBROUTINE BACK(N,Y,C,AL,Z)

```

```

      IMPLICIT REAL*8 (A-H,O-Z)
      DIMENSION AL(3,3,101),C(3,3,101),Z(3,101),Y(3,101)
      DIMENSION WKAREA(10),V(3,1),DU(3,3)
      NP1=N+1
      DO 5 I=1,3
        V(I,1)=Y(I,NP1)
5     CONTINUE
      DO 15 I=1,3
        DO 10 J=1,3
          DU(I,J)=AL(I,J,NP1)
10    CONTINUE
15    CONTINUE
      MS=1
      NS=3
      IA=3
      IDGT=0

C
C     IMSL matrix solver.
C
      CALL LEQTLF(DU,MS,NS,IA,V,IDGT,WKAREA,IER)
      DO 20 I=1,3
        Z(I,NP1)=V(I,1)
20    CONTINUE
      DO 50 K=1,N
        B1=0.0D0
        DO 25 J=2,3
          B1=B1+C(3,J,NP1-K)*Z(J,NP1+1-K)
25    CONTINUE
        Y(3,NP1-K)=Y(3,NP1-K)-B1
        DO 30 I=1,3
          V(I,1)=Y(I,NP1-K)
30    CONTINUE
        DO 40 I=1,3
          DO 35 J=1,3
            DU(I,J)=AL(I,J,NP1-K)
35    CONTINUE
40    CONTINUE
        MS=1
        NS=3
        IA=3
        IDGT=0

C
C     IMSL matrix solver.
C
      CALL LEQTLF(DU,MS,NS,IA,V,IDGT,WKAREA,IER)
      DO 45 I=1,3
        Z(I,NP1-K)=V(I,1)
45    CONTINUE
50    CONTINUE
      RETURN
      END

```

```

C
C Subroutine COEFFS computes the entries of the matrices
C [A], [B], [C], and [W] of the block tridiagonal system.
C The system arises from the discretization of the
C parabolic momentum equation with Keller's box scheme.
C

```

```

SUBROUTINE COEFFS(AHAT,BHAT,CHAT,DHAT,S,P,Q)
IMPLICIT REAL*8 (A-H,O-Z)
DIMENSION AHAT(101),BHAT(101),DHAT(101),GI(101),BFI(101)
DIMENSION P(101),Q(101),T(101),S(101),CHAT(101)
DIMENSION SFI1(101),BFI1(101),GI1(101),SFI2(101)
DIMENSION XI(101),XI1(101),PXL(101),PXL1(101),BUOY(101)
DIMENSION SFI(101),BUOY1(101),DETA(101),ALFA(1000)
COMMON/BLK1/DETA,CE,N
COMMON/BLK2/ALFA,IS
COMMON/BLK3/SFI,BFI,GI
COMMON/BLK4/SFI1,BFI1,GI1
COMMON/BLK5/PRTR,PRTR1,PRST,PRST1
COMMON/BLK6/XI,XI1
COMMON/BLK8/PXL,PXL1
COMMON/BLK14/BUOY,BUOY1
NP1=N+1
AI=ALFA(IS)

```

```

C
C Computation of the mixing length based on the
C latest station update.
C

```

```

IF(PRTR.GT.0.0D0) THEN
  CALL MIXLEN(IREF,PRTR)
ENDIF
DO 10 K=2,NP1

```

```

C Influence coefficient of the inner eddy viscosity.
C

```

```

  IF(PRTR.GT.0.0D0) THEN
    IF((K-1).LE.IREF) THEN
      PINF1=2.0D0
    ELSE
      PINF1=1.0D0
    ENDIF
    IF(K.LE.IREF) THEN
      PINF=2.0D0
    ELSE
      PINF=1.0D0
    ENDIF
    ENDEF
    DE=DETA(K)
    ASF=(SFI(K)+SFI(K-1))/2.0D0
    ASF1=(SFI1(K)+SFI1(K-1))/2.0D0
    ABF=(BFI(K)+BFI(K-1))/2.0D0
    ABF1=(BFI1(K)+BFI1(K-1))/2.0D0

```

```

AG=(GI(K)+GI(K-1))/2.0D0
AG1=(GI1(K)+GI1(K-1))/2.0D0
AX=(XI(K)+XI(K-1))/2.0D0
AX1=(XI1(K)+XI1(K-1))/2.0D0
AXD=XI(K)-XI(K-1)
AX1D=XI1(K)-XI1(K-1)
PVF=1.0D0-(AX+AX1)/2.0D0
PVK=1.0D0+(0.9+2.6*XI(K))*XI(K)
PVK1=1.0D0+(0.9+2.6*XI(K-1))*XI(K-1)
PV1K=1.0D0+(0.9+2.6*XI1(K))*XI1(K)
PV1K1=1.0D0+(0.9+2.6*XI1(K-1))*XI1(K-1)
PLKG=1.0D0+(PINF/(1.0D0-XI(K)))*PXL(K)
PLKG1=1.0D0+(PINF1/(1.0D0-XI(K-1)))*PXL(K-1)
PLK=1.0D0+(1.0D0/(1.0D0-XI(K)))*PXL(K)
PLK1=1.0D0+(1.0D0/(1.0D0-XI(K-1)))*PXL(K-1)
PL1K=1.0D0+(1.0D0/(1.0D0-XI1(K)))*PXL1(K)
PL1K1=1.0D0+(1.0D0/(1.0D0-XI1(K-1)))*PXL1(K-1)
P(K)=-SFI(K)+DE*ABF+SFI(K-1)
Q(K)=-BFI(K)+DE*AG+BFI(K-1)
AHAT(K)=DE*PVF*AI*ABF
BHAT(K)=-DE*PVF*(AG+AI*(AG+AG1))/2.0D0
CHAT(K)=-PVF*DE*(ASF-AI*(ASF1-ASF))/2.0D0-PRST*
>(AX+(1.0D0-AX)*PLKG)*PVK
  DHAT(K)=-PVF*DE*(ASF-AI*(ASF1-ASF))/2.0D0+PRST1*
>(AX1+(1.0D0-AX1)*PLKG1)*PVK1
  S1=DE*(AI*(ABF**2-ABF1**2+AG*ASF1-ASF*AG1)-(1.0D0+AI))*
>ASF*AG-(1.0D0-AI)*AG1*ASF1)
  S2=AX*PRST*(PVK*GI(K)-PVK1*GI(K-1))+
>AX1*PRST1*(PV1K*GI1(K)-PV1K1*GI1(K-1))
  S3=(1.0D0-AX)*(PVK*PLK*GI(K)-PVK1*PLK1*GI(K-1))*
>PRST+(1.0D0-AX1)*(PV1K*PL1K*GI1(K)-PV1K1*PL1K1*GI1(K-1))
>*PRST1

```

C
C
C
C

Computation of the buoyancy generated source term
of the momentum equation.

```

      S4=DE*(BUOY(K)+BUOY(K-1)+BUCY1(K)+BUOY1(K-1))/2.0D0
      S(K)=-S1*PVF+S2+S3+S4
10 CONTINUE
RETURN
END

```

C
C
C
C

Subroutine MA computes the matrix [A] of the discretized
momentum equation.

```

SUBROUTINE MA(AHAT,BHAT,CHAT,A)
IMPLICIT REAL*8 (A-H,O-Z)
DIMENSION DETA(101),A(3,3,101)
DIMENSION AHAT(101),CHAT(101),BHAT(101)
COMMON/BLK1/DETA,CE,N
NP1=N+1
A(1,1,1)=1.0D0
A(2,2,1)=1.0D0
A(3,2,1)=-1.0D0
A(3,3,1)=-DETA(2)/2.0D0
A(1,2,1)=0.0D0
A(2,1,1)=0.0D0
A(2,3,1)=0.0D0
A(1,3,1)=0.0D0
A(3,1,1)=0.0D0
DO 10 K=2,N
  A(1,1,K)=1.0D0
  A(1,2,K)=-DETA(K)/2.0D0
  A(2,1,K)=BHAT(K)
  A(2,2,K)=AHAT(K)
  A(2,3,K)=CHAT(K)
  A(3,1,K)=0.0D0
  A(3,2,K)=-1.0D0
  A(3,3,K)=-DETA(K+1)/2.0D0
  A(1,3,K)=0.0D0
10 CONTINUE
A(1,1,NP1)=1.0D0
A(1,2,NP1)=-DETA(NP1)/2.0D0
A(1,3,NP1)=0.0D0
A(2,1,NP1)=BHAT(NP1)
A(2,2,NP1)=AHAT(NP1)
A(2,3,NP1)=CHAT(NP1)
A(3,1,NP1)=0.0D0
A(3,2,NP1)=1.0D0
A(3,3,NP1)=0.0D0
RETURN
END

```

C
C
C
C

Subroutine MB computes the matrix [B] of the discretized momentum equation.

```

SUBROUTINE MB(AHAT,BHAT,DHAT,B)
IMPLICIT REAL*8 (A-H,O-Z)
DIMENSION B(3,3,101),DETA(101)
DIMENSION AHAT(101),BHAT(101),DHAT(101)

```

```

COMMON/BLK1/DETA,CE,N
NP1=N+1
DO 10 K=2,NP1
  B(1,1,K)=-1.0D0
  B(1,2,K)=-DETA(K)/2.0D0
  B(1,3,K)=0.0D0
  B(2,1,K)=BHAT(K)
  B(2,2,K)=AHAT(K)
  B(2,3,K)=DHAT(K)
  B(3,1,K)=0.0D0
  B(3,2,K)=0.0D0
  B(3,3,K)=0.0D0
10 CONTINUE
RETURN
END

```

C
C
C
C

Subroutine MC computes the matrix [C] of the discretized momentum equation.

```

SUBROUTINE MC(C)
IMPLICIT REAL*8 (A-H,O-Z)
DIMENSION C(3,3,101),DETA(101)
COMMON/BLK1/DETA,CE,N
DO 10 K=1,N
  C(3,1,K)=0.0D0
  C(3,2,K)=1.0D0
  C(3,3,K)=-DETA(K+1)/2.0D0
  C(1,1,K)=0.0D0
  C(1,2,K)=0.0D0
  C(1,3,K)=0.0D0
  C(2,1,K)=0.0D0
  C(2,2,K)=0.0D0
  C(2,3,K)=0.0D0
10 CONTINUE
RETURN
END

```

C
C
C

Subroutine MR computes the vector [W], the source term of the discretized momentum equation.

C

```
SUBROUTINE MR(N,SFICOR,P,Q,S,R)
IMPLICIT REAL*8 (A-H,O-Z)
DIMENSION R(3,101),P(101),Q(101),S(101)
NP1=N+1
R(1,1)=SFICOR
R(2,1)=0.0D0
R(3,1)=Q(2)
DO 10 K=2,N
    R(1,K)=P(K)
    R(2,K)=S(K)
    R(3,K)=Q(K+1)
10 CONTINUE
R(1,NP1)=P(NP1)
R(2,NP1)=S(NP1)
R(3,NP1)=0.0D0
RETURN
END
```

C
C
C
C

Subroutine EXTEND performs the extension of the computational domain when necessary.

```
SUBROUTINE EXTEND(ETA)
IMPLICIT REAL*8(A-H,O-Z)
DIMENSION DETA(101),SFI(101),BFI(101),GI(101)
DIMENSION SFI1(101),BFI1(101),XI(101),XI1(101)
DIMENSION PXL(101),PXL1(101),ETA(101),SUM(101)
DIMENSION XI2(101),BUOY(101),BUOY1(101)
DIMENSION GI1(101),SUM2(101),SUM1(101)
COMMON/BLK1/DETA,CE,N
COMMON/BLK3/SFI,BFI,GI
COMMON/BLK4/SFI1,BFI1,GI1
COMMON/BLK6/XI,XI1
COMMON/BLK8/PXL,PXL1
COMMON/BLK11/SUM,SUM1,SUM2
COMMON/BLK13/SFI2,XI2
COMMON/BLK14/BUOY,BUOY1
NREF=N
N=N+2
NP1=N+1
NM1=N-1
```

```

DO 10 J=N,NP1
  DETA(J)=DETA(J-1)*CE
  ETA(J)=ETA(J-1)+DETA(J)
  PXL(J)=PXL(J-1)
  PXL1(J)=PXL1(J-1)
  XI(J)=XI(J-1)
  XI1(J)=XI1(J-1)
  XI2(J)=XI2(J-1)
  SUM(J)=0.0D0
  SUM1(J)=0.0D0
  SUM2(J)=0.0D0
  BUOY(J)=0.0D0
  BUOY1(J)=0.0D0
10 CONTINUE
DO 20 J=NM1,NP1
  SLOPE=(ETA(J)-ETA(NREF))/(ETA(NP1)-ETA(NREF))
  BFI1(J)=BFI1(NREF)+(1.0D0-BFI1(NREF))*SLOPE
  SFI1(J)=SFI1(J-1)+DETA(J)*(BFI1(J)+BFI1(J-1))/2.0D0
  BFI(J)=BFI(NREF)+(1.0D0-BFI(NREF))*SLOPE
  SFI(J)=SFI(J-1)+DETA(J)*(BFI(J)+BFI(J-1))/2.0D0
  SFI2(J)=SFI2(J-1)+DETA(J)*(BFI(J)+BFI(J-1))/2.0D0
  GI(J)=0.0D0
  GI1(J)=0.0D0
20 CONTINUE
RETURN
END

```

C
C Subroutine MIXLEN computes the wall function of
C the turbulence model through a modified Van Driest
C type expression.
C

```

SUBROUTINE MIXLEN(IREF,PRTR)
IMPLICIT REAL*8(A-H,O-Z)
DIMENSION PXL(101),PXL1(101),SFI(101),BFI(101)
DIMENSION GI(101),ETA(101),XI(101),XI1(101),ZI(1000)
DIMENSION SFI1(101),BFI1(101),GI1(101),ALFA(1000)
DIMENSION YPLUS(101),DETA(101)
COMMON/BLK1/DETA,CE,N
COMMON/BLK2/ALFA,IS
COMMON/BLK3/SFI,BFI,GI
COMMON/BLK4/SFI1,BFI1,GI1
COMMON/BLK6/XI,XI1
COMMON/BLK7/ZI,ETA
COMMON/BLK8/PXL,PXL1
COMMON/BLK9/ISINJI,EREF,VISCL,VISCT

```

```

COMMON/BLK12/YPLUS,USTAR
NP1=N+1
DZI=ZI(IS)-ZI(IS-1)
DO 5 K=2,NP1
    PXL1(K)=PXL(K)
5 CONTINUE
PRZI=DSQRT(2*ZI(IS))
USTAR=DSQRT(DABS(GI(1))*VISCL/PRZI)
VWALL=-VISCT*(SFI(1)+2*ZI(IS)*(SFI(1)-SFI1(1))/DZI)/PRZI

C
C Wall function injection modification.
C
IF(IS.LE.ISINJI) THEN
    ZETA=0.5D0
ELSE
    ZETA=1.5D0
ENDIF
APLUS=26.0D0/(1.0D0+5.9*VWALL/USTAR)
DO 20 K=2,NP1
    RA1=(1.0D0-XI(K))/(1.0D0-XI(1))
    RA2=(1.0D0+(0.9+2.6*XI(K))*XI(K))/
>(1.0D0+(0.9+2.6*XI(1))*XI(1))
    RA3=(1.0D0-XI(K))/(1.0D0+(0.9+2.6*XI(K))*XI(K))
    YPLUS(K)=ETA(K)*DSQRT(PRZI*RA1*RA3*DABS(GI(1))/
>(VISCL*RA2))
    POWER=-YPLUS(K)*(((RA2/RA1)*DABS(GI(K)/GI(1))))**
>ZETA)/APLUS
    EII=0.41*ETA(K)*(1.0D0-DEXP(POWER))
    PXL(K)=PRZI*DABS(GI(K))*(EII**2)/VISCL
20 CONTINUE
E0I=EREF
DO 25 K=2,NP1
    IF(PXL(K).LT.E0I) THEN
        IREF=K
    ELSE
        GO TO 30
    ENDIF
25 CONTINUE
30 IREFP1=IREF+1
DO 40 K=IREFP1,NP1
    PXL(K)=E0I
40 CONTINUE

C
C Modification of the mixing length during
C transition.
C
IF(PRTR.LT.1.0D0) THEN
    DO 50 K=2,NP1
        PXL(K)=PRTR*PXL(K)
50 CONTINUE
ENDIF
RETURN
END

```

C
C Subroutine BLPR computes boundary layer integral
C parameters, the boundary layer displacement
C thickness and the momentum thickness.
C

```
SUBROUTINE BLPR(DELSTR,TETSTR)
  IMPLICIT REAL*8(A-H,O-Z)
  DIMENSION ETA(101),DETA(101),ZI(1000),XI(101)
  DIMENSION SFI(101),BFI(101),GI(101),XI1(101)
  COMMON/BLK1/DETA,CE,N
  COMMON/BLK3/SFI,BFI,GI
  COMMON/BLK6/XI,XI1
  NP1=N+1
  DELSTR=0.0D0
  TETSTR=0.0D0
  DO 10 K=2,NP1
    AK1=(1.0D0-XI(K-1))*(1.0D0-BFI(K-1))
    AK=(1.0D0-XI(K))*(1.0D0-BFI(K))
    BK1=AK1*BFI(K-1)
    BK=AK*BFI(K)
    DELSTR=DELSTR+(AK1+AK)*DETA(K)
    TETSTR=TETSTR+(BK1+BK)*DETA(K)
10 CONTINUE
  DELSTR=DELSTR/2.0D0
  TETSTR=TETSTR/2.0D0
  RETURN
  END
```

C
C Subroutine VOLFRFC computes computes the volume fraction
C according to a hyperbolic transport equation.
C

```
SUBROUTINE VOLFRFC(XI,XI1,ZI)
  IMPLICIT REAL*8(A-H,O-Z)
  DIMENSION DETA(101),XI(101),XI1(101),ALFA(1000),GI1(101)
  DIMENSION SFI(101),BFI(101),GI(101),SFI1(101),BFI1(101)
  DIMENSION SFI2(101),XI2(101),ZI(1000)
  COMMON/BLK1/DETA,CE,N
  COMMON/BLK2/ALFA,IS
  COMMON/BLK3/SFI,BFI,GI
  COMMON/BLK4/SFI1,BFI1,GI1
  COMMON/BLK13/SFI2,XI2
```

```

EPS=1.0D-5
NP1=N+1
BI=ZI(IS)
DZI=ZI(IS)-ZI(IS-1)
DZI1=ZI(IS-1)-ZI(IS-2)
DE=DZI/DZI1

```

C
C
C
C

Computation of the first node of the void fraction profile after injection.

```

IF(IS.GT.ISINJF) THEN
  PRI=(2*DE+1.0D0)/(1.0D0+DE)
  PRI1=-(1.0D0+DE)
  PRI2=(DE**2)/(1.0D0+DE)
  DIR=2*BI*DETA(2)*BFI(2)*(PRI1*XI(2)+PRI2*XI2(2))
  COEF1=PRI*SFI(2)+PRI1*SFI1(2)+PRI2*SFI2(2)
  ESQ=2*BI*DETA(2)*BFI(2)*PRI-DZI*SFI(2)-2*BI*COEF1
  XI(2)=DIR/ESQ
ENDIF

```

C
C
C

Computation of the void fraction profile.

```

5 DO 10 K=3,NP1
  BIK=2*DETA(K)*BI*BFI(K)
  CIK=DZI*(1.0D0+DE)*SFI(K)+2*BI*(SFI2(K)*DE**2-
>SFI1(K)*(1.0D0+DE)**2+(2*DE+1.0D0)*SFI(K))
  COEF1=CIK/((1.0D0+2*DE)*BIK-CIK)
  COEF2=BIK/((1.0D0+2*DE)*BIK-CIK)
  XI(K)=-COEF1*XI(K-1)-COEF2*
>(XI2(K)*DE**2-XI1(K)*(1.0D0+DE)**2)
10 CONTINUE

```

C
C
C
C

Convergence procedure of the void fraction profile based on the zero wall void fraction gradient.

```

IF(IS.LE.ISINJF) THEN
  PRXI1=-(2.0D0+CE)/(DETA(2)*(CE+1.0D0))
  PRXI2=(1.0D0+CE)/DETA(3)
  PRXI3=-1.0D0/(DETA(3)*(1.0D0+CE))
  XIWGRD=XI(1)*PRXI1+XI(2)*PRXI2+XI(3)*PRXI3
  IF(DABS(XIWGRD).GT.EPS) THEN
    XI(2)=(XI(1)*CE*(2.0D0+CE)+XI(3))/((1.0D0+CE)**2)
    GO TO 5
  ENDIF
ENDIF
RETURN
END

```

C
C

Subroutine ARCHIE computes the source term of the

C momentum equation due to the buoyancy force field
C according to Archimedes principle.
C

```
SUBROUTINE ARCHIE(XI,BUOY)
IMPLICIT REAL*8(A-H,O-Z)
DIMENSION SUM(101),SUM1(101),DETA(101),ALFA(1000)
DIMENSION ZI(1000),ETA(101),XI(101),BUOY(101)
DIMENSION XI1(101),SUM2(101)
COMMON/BLK1/DETA,CE,N
COMMON/BLK2/ALFA,IS
COMMON/BLK7/ZI,ETA
COMMON/BLK10/GRAV,ROUL,UE
COMMON/BLK11/SUM,SUM1,SUM2
NP1=N+1
DZI=ZI(IS)-ZI(IS-1)
DZI1=ZI(IS-1)-ZI(IS-2)
DE=DZI/DZI1
RAX=2*ZI(IS)/DZI
FAC1=(2*DE+1.0D0)/(1.0D0+DE)
FAC2=-(1.0D0+DE)
FAC3=(DE**2)/(1.0D0+DE)
FAC4=(2*CE+1.0D0)/(1.0D0+CE)
FAC5=-(1.0D0+CE)
FAC6=(CE**2)/(1.0D0+CE)
DO 10 K=1,N
    SUM(N+1-K)=SUM(N+2-K)+DETA(N+2-K)*(XI(N+1-K)+
>XI(N+2-K))/2.0D0
10 CONTINUE
    DISTX=DSQRT(2*ZI(IS))
    FACTOR=DISTX*GRAV/(ROUL*(UE**3))
    BUOY(1)=FACTOR*(SUM(1)+RAX*(SUM(1)*FAC1+SUM1(1)*FAC2+
>SUM2(1)*FAC3))
    TERM1=SUM(2)-SUM(1)
    TERM2=SUM(2)*FAC1+SUM1(2)*FAC2+SUM2(2)*FAC3
    BUOY(2)=FACTOR*(SUM(2)+RAX*TERM2-TERM1)
    DO 20 K=3,NP1
        RAY=ETA(K)/DETA(K)
        TERM1=SUM(K)*FAC4+SUM(K-1)*FAC5+SUM(K-2)*FAC6
        TERM2=SUM(K)*FAC1+SUM1(K)*FAC2+SUM2(K)*FAC3
        BUOY(K)=SUM(K)+RAX*TERM2-RAY*TERM1
        BUOY(K)=BUOY(K)*FACTOR
20 CONTINUE
RETURN
END
```

END
DATE
FILMED

5-88
DTIC